10-26-2020

Surface-enhanced Raman Spectroscopy for Single Molecule Analysis and Biological Application

Jing Guo
Florida International University, jguo026@fiu.edu

FLORIDA INTERNATIONAL UNIVERSITY
Miami, Florida

SURFACE-ENHANCED RAMAN SPECTROSCOPY FOR SINGLE MOLECULE ANALYSIS AND BIOLOGICAL APPLICATION

A dissertation submitted in partial fulfillment of
the requirements for the degree of
DOCTOR OF PHILOSOPHY
in
PHYSICS
by
Jing Guo

2020

To: Dean Michael R. Heithaus
College of Arts, Sciences and Education

This dissertation, written by Jing Guo, and entitled Surface-Enhanced Raman Spectroscopy for Single Molecule Analysis and Biological Application, having been approved in respect to style and intellectual content, is referred to you for judgment.

We have read this dissertation and recommend that it be approved.

Xuewen Wang

Yuan Liu

Hebin Li

Jin He, Major Professor

Date of Defense: October 26, 2020

The dissertation of Jing Guo is approved.

Dean Michael R. Heithaus
College of Arts, Sciences and Education

Andrés G. Gil
Vice President for Research and Economic Development
and Dean of the University Graduate School

Florida International University, 2020

DEDICATION

I dedicate this dissertation to my parents, sister and husband. To me, you are the world.

ACKNOWLEDGMENT

I would like to express my sincere appreciation to my mentor, Professor Jin He. He is knowledgeable, affable, and has given me adroit guidance throughout my time here. Furthermore, his perseverance and positive attitude to scientific research benefit me greatly. It was my experience working in his lab for two years as a visiting student that led me to decide on FIU for my Ph.D. program. I am a slow learner and had little training in the sciences when I first joined his group, but he has been so patient with me. With his mentoring for six years, my skill in problem-solving, critical thinking, presenting, and paper writing grew and grew. Without his persistent help, the goal of my research would not have been realized. I feel really lucky to have him as my mentor.

I would like to extend my sincere gratitude to Professor Xuewen Wang, who wrote the recommendation letter that helped me enter the FIU Ph.D. program. He has always given excellent advice for my research from weekly group meetings and has taught me much about theoretical calculation. I appreciate my committee members, Professor Hebin Li, and Professor Yuan Liu, for taking time out of their busy days to help me with my Ph.D. program. I also wish to thank them for helping me attain the Dissertation Year Fellowship (DYF) award.

I would like to pay my special regards to electrical engineer Norman and mechanical engineer Zahid for their help with maintaining the instruments and their skill with building home-made devices. With their help, my research went on smoothly. I would also like to thank the whole physics department, along with all the professors and department staff, for their support. I would also like to thank the FIU AMERI staff for training me to use the Cleanroom and SEM facilities.

I would like to thank my colleagues: Puru, Numuna, Alberto, Dr. Chang, Popular, Govinda, Feng, Tao, and Qiushuang. They have always been there for me, understanding, and giving their support. Especially, I want to thank Puru and Numana for getting me familiar with our lab facilities at the beginning of my research. I also want to thank Alberto for teaching me the basics of biological bench work and providing me cell samples for my research. My sincere thank also goes to Dr. Chang, for teaching me Labview programming. It is a very useful skill for data analysis and instrument control. I would like to thank Benjamin Gross for proofreading and editing my dissertation.

I wish to acknowledge the Engineering Research Centers Program of the National Science Foundation, which under NSF Cooperative Agreement No. EEC-1647837 and NSF (CBET1454544) support me as a research assistant. I want to thank the Graduate School at Florida International University for providing me the DYF Award. Thanks to the DYF award, I can focus on dissertation writing and finish my research.

Last but not least, I would like to thank my parents and sister. With their support and serval hours of talk every Saturday, I feel not lonely even in a foreign country. The happiest moments are when we are talking and sharing our lives. I wish to thank my husband for his company. Every weekend, we will spend a whole day preparing food together. At that time, I am always so happy and calm, and know I can carry on.

ABSTRACT OF THE DISSERTATION

SURFACE-ENHANCED RAMAN SPECTROSCOPY FOR SINGLE MOLECULE ANALYSIS AND BIOLOGICAL APPLICATION

by

Jing Guo

Florida International University, 2020

Miami, Florida

Professor Jin He, Major Professor

Surface-enhanced Raman spectroscopy (SERS) is a surface analytical technique, which enhances the Raman signal based on the localized surface plasmon resonance (LSPR) phenomenon. It has been successfully used for single molecule (SM) detection and has extended SERS to numerous applications in biomolecular detection. However, SM detection by SERS is still challenging especially with traditional SERS substrates and detection methods. In addition, the fundamental understanding of the SERS enhancement mechanism is still elusive. Furthermore, the application of SERS in biological field is still in the early stage. To address these challenges, there are two main aspects of SERS studied in my dissertation: (a) fundamental aspects through systematic experimental studies combined with simulations, which focus on SM detection, Raman enhancement mechanisms, and (b) the development and optimization of the SERS-based nanoprobe for biomarkers detection from fluidic devices to a single cell.

In my dissertation, the following studies have been investigated. First, the sensitivity of a home-made SERS instrument was tested. SM detection was realized by utilizing a highly curved nanoelectrode (NE) to limit the number of attached nanoparticle (NP), which will allow us to have even a single NP on NE (NPoNE) junction in the SERS detection area.

The molecule number in a single NPoNE junction which contributes to SERS can be hundreds or even SM. In this first study, we also conducted a correlation study between electrochemical current and SERS to monitor the dynamic formation of the plasmonic junctions. Second, we investigate electromagnetic and chemical enhancement factor tuning by the electrode potential with the assistant of Au@Ag core-shell NPs. The electrode potential induced electromagnetic enhancement (EME) tuning in the Au@Ag NPoNE structure has been confirmed by 3D Finite-difference time-domain (FDTD) simulations. Last is the design of a SERS-based nanoprobe for biomarkers detection and the effort towards single cell analysis. Finally, several SERS-active substrates were examined for biomarkers (H^+, glucose, and H_2O_2) detection, including gold NPs (AuNPs) colloid and AuNPs decorated glass nanopipette.

In summary, my dissertation presents the fabrication and development of gold tip nanoelectrode for chemical detection, which can achieve SM sensitivity. SM SERS can be used to improve the fundamental understanding and provide more in-depth insight into mechanisms of SERS and the chemical behaviors of SM on surfaces and in plasmonic cavities. Second, the fabrication and optimization of SERS-active, flexible nanopipette for biological applications. The flexible nanopipette probe provides a platform for reliable detection and quantitative analysis of biomarkers at a single cell level, which is critical and vital for detecting diseases earlier and understanding the fundamental biological process better.

TABLE OF CONTENTS

LIST OF TABLES

TABLE PAGE

LIST OF FIGURES

FIGURE PAGE

CHAPTER 1 INTRODUCTION

1.1 The Motivation of Using SERS to Probe Molecule and Cell

Surface-enhanced Raman spectroscopy (SERS) is a surface analytical technique that enhances a Raman signal based on the localized surface plasmon resonance (LSPR) phenomenon. LSPR is defined as a coherent oscillation of electrons on the surface of metallic nanostructures when interaction with the electromagnetic wave of the incident light. The nanostructure which supports a LSPR response is also called a plasmonic nanostructure, which includes bulk solutions of nanoparticles, nanoparticle arrays, or single nanoparticles. There are the following advantages of SERS for chemical analysis: (i) Direct identification of chemical species since Raman spectra represent the vibrational fingerprints of molecules; (ii) Minimum sample preparation; (iii) Measurement in aqueous solution measurement is possible, owning to weak Raman signal of water; (iv) SERS allows multiplex capability, which means different analytes can be detected simultaneously. (v) On-site analysis is possible with a portable Raman instrument. Since the detection of single-molecule (SM) of resonant dyes by SERS in 1997[1, 2] and the development of plasmonic nanostructures in 2000 s[3], extensive attention was paid to SERS and the development of SMSERS and biological applications. SMSERS can be used to improve the fundamental understanding and provide deeper insight into mechanisms of SERS and the chemical behaviors of SM on surfaces and in plasmonic cavities. Besides SERS's utility in SM analysis, several analytical techniques were also developed for SM analysis, e.g., single-molecule fluorescence spectroscopies, scanning probe microscopies (SPM), and force spectroscopies. However, only SERS can provide the chemical information other

than molecular electronic states, conductance, and surface topography provided by other techniques.

Meanwhile, the excellent molecule specificity, high sensitivity, and weak water signal of SERS enable its biological application. The accurate and quantitative analysis of a set of disease-related biomarkers in the early stages of illness is highly significant to disease diagnosis, treatment, and management. Small molecules other than traditional protein biomarkers may provide valuable biological process information. For example, abnormalities in glucose utilization, metabolism, and oxidative stress have been found in patients suffering from the disease.[4-8] The elevation or reduction of the level of a given biomarker may indicate a specific disease state or correlate with the risk or progression of a disease.[9, 10] The early diagnosis of disease at the earliest possible stage is critical for the implementation of successful treatment. For example, Alzheimer's disease (AD) causes 5.1 million patients suffering in USA, but there is no definitive and accurate diagnosis method.[11] Previous review paper[5] discusses recent strategies and techniques employed for the discovery of biomarkers in AD, showing the importance of biomarkers to the knowledge and understanding of the disease. In addition to its potential for early disease diagnosis, monitoring of specific biomarkers can be used for drug development. Specifically, biomarkers tell us of metabolic changes over time after the addition of a drug to an organ, tissue, or cell. It would help researchers better understand the treatment response and disease progression.[12, 13] Moreover, in vivo biosensing also benefits patients with chronic disease. For example, minimally invasive and continuous glucose monitoring for diabetic patients can provide a complete picture of glucose fluctuation and help diabetic patients control their glucose levels better. However, traditional analytical techniques,

including separation methods, magnetic resonance spectroscopy, and immunoassays, almost always require sample preparation prior to analysis. Further compounding the inconvenience, sample preparation steps often need large volumes (>mL). Meanwhile, these methods lack the ability to provide real-time monitoring and single cell analysis.

1.2 Background of SERS

The Raman scattering effect was discovered by an Indian physicist Chandrashekhara Venkata (C.V.) Raman in 1928[14, 15]. For his discovery, Raman was awarded the Nobel Prize in physics in 1930. Since then, Raman spectroscopy has been used as a basic analytical tool by chemists. Raman spectroscopy is a technique for studying the inelastic scattering of light with matters. As most scattering photons after interacting with molecules experience Rayleigh scattering, only about 1 in 10^7 photons undergo Raman scattering[16]. In 1974, Fleischmann[17] found that Raman signal from pyridine was considerably enhanced when the analyte was adsorbed on a silver electrode. In 1977, Van Duyne group[18] and Albrecht[19] attributed the Raman signal enhancement to the electric field enhancement on the roughened metal surface, and named this physical phenomenon as SERS. Nie[1] and Kneipp[2] both claimed Single molecule (SM) detection of rhodamine 6G dye molecules by SERS analysis in 1997.

1.2.1 SERS Enhancement Mechanism

To achieve SM detection by Raman spectroscopy, a huge enhancement factor (EF) is needed to boost the SERS signal. EF is used to quantify the Raman signal enhancement due to the presence of SERS substrate. It is defined as the ratio of the normalized SERS signal to the normal Raman signal (RS) of the same molecule[20] (Figure 1-1), as follows

$$EF_{SERS} = \frac{I_{SERS}/N_{SERS}}{I_{RS}/N_{RS}}$$

Where I_{SERS} and I_{RS} are the intensities of the SERS and the normal Raman spectroscopy (NRS) signals, respectively. N_{SERS} and N_{RS} are the number of molecules contributing to the SERS and NRS signals, respectively.

The Raman spectroscopy community widely accepts that there are two Raman enhancement mechanisms to contribute to the total EF: electromagnetic enhancement (EME) and chemical enhancement (CE). The total EF = EF_{EME}*EF_{CM}.

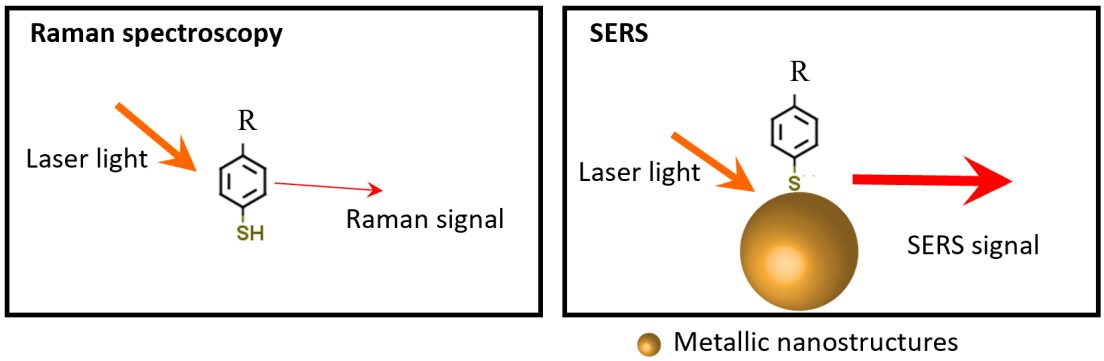

Figure 1-1 Schematic of the difference between the normal Raman signal and surface-enhanced Raman signal of the same one molecule on the SERS enhancement substrate, here use metallic nanostructures as the SERS substrate for example.

EME Mechanism

Electromagnetic enhancement of the Raman signal that result from a localized surface plasmon resonance (LSPR) generated on the surface of nanostructures by electromagnetic fields. Surface plasmons (SPs) are the collective oscillation of surface conduction electrons of the nanostructure of certain metals (such as Au, Ag, and Cu). Localized surface plasmon resonance happens when plasmonic nanoparticles are smaller in size than the wavelength of incoming light. Figure 1-2 shows the LSPR in a nanoparticle

induced by incident light. The LSPR creates regions of intense EME field on a nanostructure's surface, nanostructure gap, or sharp edge, known as hot spots. Enhancement factor of EME can be made to range from 10^5 to 10^8 by wisely choosing incident light frequency and plasmonic structure. In some cases, this EF of hot spots is high enough to be able to detect a single molecule of an analyte.

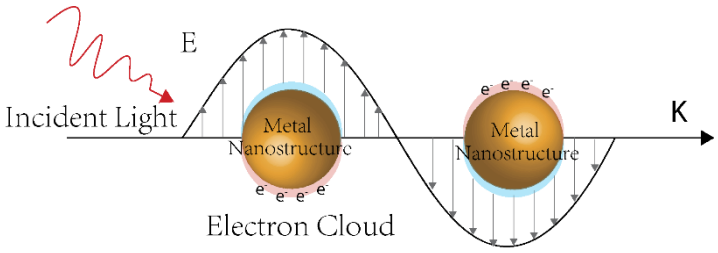

Figure 1-2 Schematic drawing (not to scale) of the LSPR phenomenon. When incident light interacts with plasmonic nanoparticles, the electric field component of light will induce the oscillation of electron cloud at the surface plasmonic nanoparticle with a specific frequency. The frequency will be affected by the shape, size of the nanoparticle, and its environment. Adapted from ref [20].

CE Mechanism

The chemical enhancement mechanism contributes to total EF on the order of 10 - 100. The CE mechanism of enhancement requires that the molecule of the analyte is chemically bonded to the metal nanostructure. This mechanism may explain the differences between EF values obtained theoretically and experimentally. There are two main processes for CE: (1) Resonant charge transfer between the Fermi level of the metal atom and an unfulfilled orbit of the analyte. (2) Nonresonant changes in the molecular polarizability upon surface binding. Table 1-1 summarized the comparison between EME and CE enhancement.

Table 1-1 The comparison between EME and CE enhancement.

EME	CE
EME originates from light and SERS substrate interaction.	The CE arises from a modification of the polarizability of a molecule.
Independent of the type of molecule.	Depends on the type of molecule.
Major enhancement contribution (EF_{EME}~10^8).	Minor contribution (EF_{CE}~10^2).
Long-range effect (<10 nm).	Short-range effect: requires contact or a very small separation (a few Å).

1.2.2 Plasmonic Structures and Hot Spot

Following the demonstrations of SMSERS, the correlation investigation between SERS and atomic force microscopy (AFM) shows that the SMSERS-active sites were aggregates of silver NPs (AgNPs).[1, 21] The nanocavities between aggregated NPs, also called hotspot, are important to achieve SMSERS. More accurate structure information of SMSERS-active sites can be provided by high-resolution transmission electron microscopy (TEM) than by AFM. Combining TEM with a theoretical approach and SERS techniques reveal that the single dye molecule (R6G) needs EF of 10^8 to achieve a detectable SERS signal. Please note a) the Raman cross-section of R6G is around $2.3*10^{-22}$ $cm^2*molecule^{-1}$, compared to non-resonant molecules (~10^{-28} – 10^{-30}), which need EF of 10^{14} to achieve SM detection. b) Hotspots are defined as EF>10^5, and hotspots can exist on the sharp edges of plasmonic NP, NP gaps, and crevices. To improve the systematic fundamental understanding of SERS mechanisms, a more rationally designed and reproducible SERS-active substrate is needed. Figure 1-3 shows the rationally designed SERS-active substrates: A) E-beam lithographically prepared nanoantennas;[22] B) triangular nanopyramids prepared by nanosphere lithography;[23] C) nanoparticle on mirror;[24] D) finishing-mode TERS. This is realized by combining SERS and scanning tuning microscopy (STM).[25]

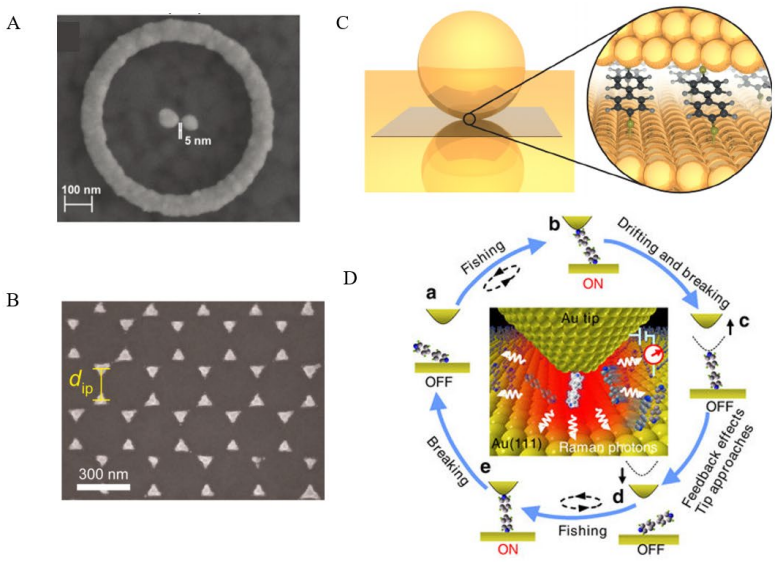

Figure 1-3 Rationally designed SERS-active substrate for single-molecule detection. (A) E-beam lithographically prepared nanoantennas, reprinted with permition from reference[22]. (B) triangular nanopyramids prepared by nanosphere lithography, reprinted with permition from reference[23]. (C) Nanoparticle on mirror, reproduced with permition from reference[24]. (D) finishing-mode TERS, reproduced with permition from reference[25].

1.2.3 SERS Substrate Material

The traditional SERS enhancement substrates are the materials that have the LSPR effect, for example, Au, Ag, Cu, and Al. Also, non-metallic materials and 2D materials are studied to enhance Raman signals. The comparison of those types of materials is summarized in table 1-2. In this dissertation, Au and Ag are materials used to amplify Raman signal, owing to they are easy to achieve high EF.

Table 1-2 Materials for SERS enhancement.

SERS enhancement material	**1. Metallic Materials (Au, Ag, Cu, Al)**	**2. Non-Metallic Materials (Doped ZnO, TiN, TiO_2)**	**3. 2D Materials (Graphene)**
Advantage	a) LSPR effect, high EF; b) Alloyed with transition metal with modified optical properties; Magnetic and catalytic functions can combine.	a) Non-absorbing materials: no overheating; laser power can be raised to increase Raman signal;	CT enhancement

		b) The band gap can be tuned to optimize the EF.	
Disadvantage	Plasmonic heating: damage the analyte	LSPR effect not easy to achieve in dielectrics/semiconductors, needs lots of free electrons in the conduction band.	

1.2.4 Principle of Raman Scattering

Since Raman scattering is the foundation of surface-enhanced Raman scattering, it is inevitable to introduce it first. When we consider the scattering of light after it interacts with a molecule or crystal, the majority of the photons are elastically scattered, and have the same frequency (wavelength) as the incident photons. The elastic scattering process is called Rayleigh scattering. However, a small portion of photons lose energy to the molecules that goes to promoting its vibrational mode from ground state to first excited state. This process is called Stokes Raman scattering. Conversely, when photons gain energy from molecules that go from the first excited state to the ground state, it is called anti-Stokes Raman scattering. The cross-section of Anti-Stokes (σ_k^{as}) is much smaller than that of Stokes (σ_k^{as}) of the k-th vibrational mode, so Stokes bands of Raman spectra are normally reported. The inelastic scattering process is named the Raman effect. Raman scattering can occur with a change in the vibrational, rotational, or electronic energy of a molecule.

Vibrational mode

Let us build a model about a diatomic molecule as an intruduction to the Raman effect. As shown in Figure 1-4A, two mass particles (m1, m2) represent the atoms, and the spring (spring constant, k) represents the bond between atoms. The displacement of two

particles is denoted x1 and x2, respectively. Under this assumption, the displacement can be expressed by Hooke's law:

$$k * (x1 + x2) = \frac{m1*m2}{(m1+m2)} \left(\frac{d^2x1}{d^2t} + \frac{d^2x2}{d^2t}\right) \text{ .....Eq.1}$$

By replacing the reduced mass $\frac{m1*m2}{(m1+m2)}$ with μ and the total displacement (x1+x2) with Q, the Eq. 1 can be simplified to,

$$k * x = \mu \left(\frac{d^2Q}{d^2t}\right) \text{ .....Eq. 2}$$

By solving Eq. 2 for x we get:

$$Q = Q_0 \cos(2\pi\nu_n t) \text{.....Eq. 3}$$

$$\text{Where } \nu_n = \frac{1}{2\pi}\sqrt{\frac{k}{\mu}} \text{.....Eq. 4}$$

$$E_n = \left(n + \frac{1}{2}\right) h\nu_n \text{.....Eq. 5}$$

To change the unit of ν from s^{-1} to be in cm^{-1}, c, the speed of light must be expressed in cm/s.

$$\nu_R = \frac{\nu_n}{c} = \frac{1}{2\pi C}\sqrt{\frac{k}{\mu}} \text{.....Eq. 6}$$

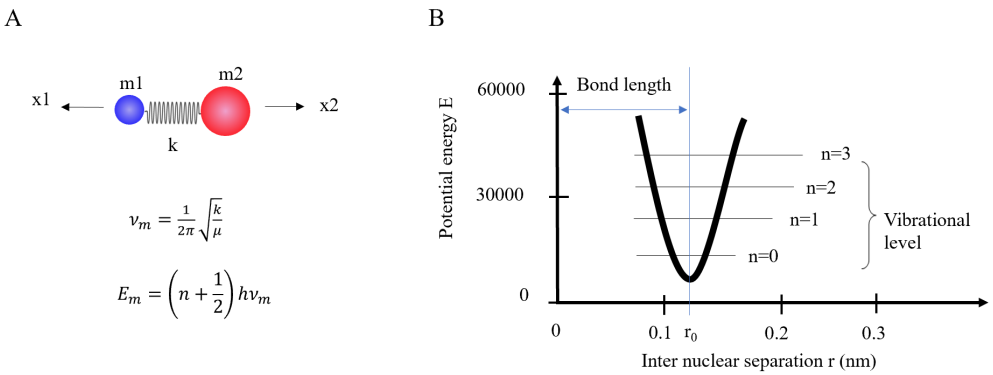

Figure 1-4 (A) Schematic spring model of a diatomic molecule as two mass balls connected by a spring. (B) Schematic representation of potential energy in the ground

electronics of the simplified model used for calculation (thick black line). Horizontal thin black lines are the vibrational energy levels of a molecule in a Jablonski diagram.

From equations Eq. 3 and Eq. 4, it shows that the molecule vibrates in a cosine pattern around its equilibrium position with a frequency proportional to the bond strength and inversely proportional to the reduced mass. The energy of the vibrational energy level can be simplified as Figure 1-4B. It tells us that each molecule will have its own unique vibrational frequency fingerprint, which is determined by its chemical structure (atoms and the individual bonds). The Raman effect allows us to measure these vibrational frequencies. It is because the polarizability of a molecule (α) is a function of displacement (x). When incident light interacts with a molecule, it induces an induced dipole moment (P). It is equal to the product of the polarizability of the molecule and the electric field of the incident light. The polarizability can be expressed as,

$$P = \alpha E_0 Cos(2\pi\nu_0 t) \text{.....Eq. 7}$$

Where E_0 and ν_0 are the intensity and frequency of the electric field of the incident light, respectively. When x is very small, we can express α as a function of x at x = 0 by the Taylor series,

$$\alpha = \alpha_0 + Q\left(\frac{\partial\alpha}{\partial Q}\right)|_{x=0} + \cdots\text{.....Eq. 8}$$

Here the higher orders of the expansion were ignored. By plugging Eq. 3 and Eq. 8 into Eq. 7 we have,

$$P = \alpha_0 E_0 Cos(2\pi\nu_0 t) + E_0 Q_0 Cos(2\pi\nu_m) Cos(2\pi\nu_0 t)\left(\frac{\partial\alpha}{\partial Q}\right)|_{x=0}\text{.....Eq. 9}$$

Rewriting the second term of Eq. 9 we have,

$$P = \alpha_0 E_0 Cos(2\pi\nu_0 t) + E_0 Q_0 \left(\frac{\partial\alpha}{\partial Q}\right)|_{x=0} (Cos(2\pi(\nu_0 - \nu_m)t +$$

$$Cos(2\pi(\nu_0+\nu_m)t)) \quad \ldots\text{Eq. 10}$$

In Eq. 10 we see that the induced dipole from the interaction of the molecule and the incident light consists of a Rayleigh dipole and a Raman dipole. The Rayleigh dipole radiation gives the Rayleigh scattering, which is the dominant effect and results in no change in the frequency of the incident light. The Raman dipole radiation is also called Raman scattering, which shifts the frequency of the incident light by plus or minus the frequency of the molecular vibration. The decrease in frequency is the Stokes shift, and the increase in frequency is the Anti-Stokes shift. By measuring the frequency difference between the incident light and Raman scattering light, we can directly access the vibrational frequency of a molecular bond.

In Figure 1-5A, the black thick line shows a more realistic model than the simplified spring model, and is more likely to be seen in empirical measurement. At room temperature, most molecules are still remain in their ground vibrational state (n=0), the spring model quite close to the Jablonski diagram. Now let us focus on the energy level in the Jablonski diagram, as shown in Figure 1-5B when the incident photon excites the molecule into a virtual energy state. There are three different potential outcomes. First, the molecule can relax back down to the ground state and emit a photon of equal energy to that of the incident photon; this is an elastic process and is again referred to as Rayleigh scattering. Second, the molecule can relax to a real phonon state and emit a photon with less energy than the incident photon, which is called Stokes shifted Raman scattering. The third potential outcome is that the molecule is already in an excited phonon state, is excited to a higher

virtual state, and then relaxes back down to the ground state emitting a photon with more energy than the incident photon, which is called Anti-Stokes Raman scattering. Since most molecules will be found in the ground state at room temperature, there is a much lower probability that a photon will be Anti-Stokes scattered. As a result, most Raman measurements are performed considering only the Stokes shifted light.

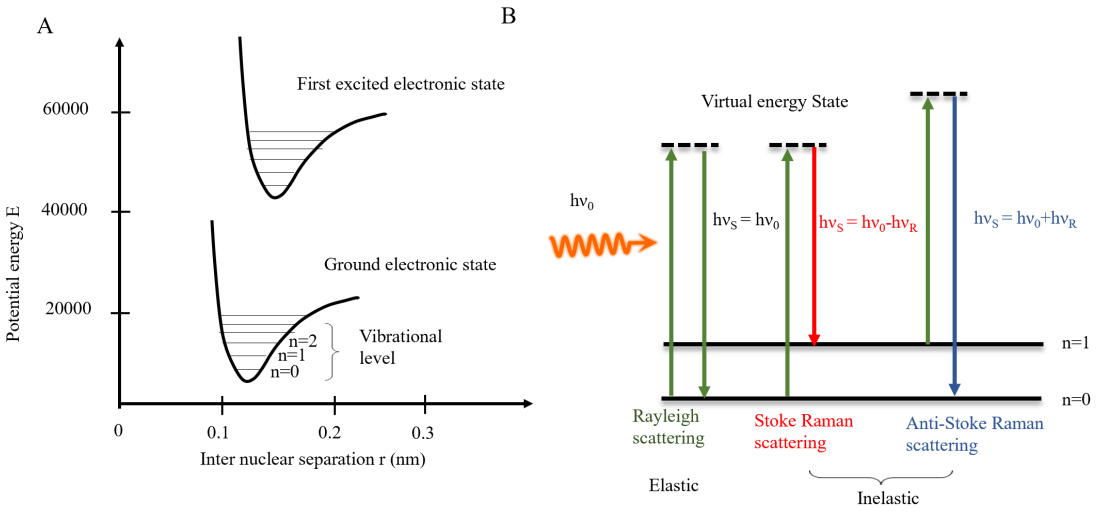

Figure 1-5 (A) Schematic representation of electronic (bold black lines) and vibrational (thin lines) energy levels of a molecule in a Jablonski diagram. (B) The vibrational energy levels in the Jablonski diagram. Possible radiative transitions between states are indicated by arrows.

Raman Selection Rules and Intensities

The selection rule for a Raman-active vibration mode is that there be a change in polarizability during the molecular vibration ($\frac{\partial \alpha}{\partial Q} \neq 0$), where Q is the normal coordinate of the molecule vibration. Scattering intensity is proportional to the square of the induced dipole moment, i.e., to the square of the polarizability derivative.

Example of a Raman Spectra

Different communities of scientists use different units for the photon energy and wavelength. Photon energy (E [J]) is proportional to angular frequency (w [rad/s]), frequency (ν [Hz] or [s^{-1}]), wave-number ($\bar{\upsilon}$ [m^{-1}]), and effective temperature (T [K]). Therefore, those parameters also can be viewed as a measure of energy. They are related by the following expressions:

$$E = h\upsilon = \hbar w = \frac{hc}{\lambda} = hc\bar{\upsilon} = k_B T$$

Where h is the Planck constant with the value of $6.626*10^{-34}$ J/S, C is the speed of light with the value of $3*10^8$ m/s. k_B is the Boltzmann constant with the value of $1.381*10^{-23}$ J/K.

As Raman spectroscopy is routinely used by chemists, the x-axis (photon transition energy) unit is wave-number ($\bar{\upsilon}$, [cm^{-1}]). The definition of vibrational mode (Raman shift) and its energy in the unit of eV is as follows:

$$\bar{v}[cm^{-1}] = \frac{10^7}{\lambda_o[nm]} - \frac{10^7}{\lambda_m[nm]}$$

$$E[eV] = \frac{1239.8}{\lambda_0[nm]} - \frac{1239.8}{\lambda_m[nm]} = 1.2398 * 10^{-4} * (\bar{v}[cm^{-1}])$$

The y-axis is the Raman scattering intensity, in arbitrary units. Figure 1-6 shows an example of the normal Raman spectrum of a chemical bulk. Bands located higher than incident light (632.8 nm) are from Stokes Raman scattering (cross-section, σ_k^s). Conversely, bands from the left side is Anti-Stokes Raman scattering (cross-section, σ_k^{as}). The k^{th} vibrational mode intensity ration between anti-Stoke and Stoke is related to the population ratio between the ground and first excited state: $\rho_k^{as/s} = \frac{\sigma_k^{as}}{\sigma_k^s} = (\frac{v_0 + v_k}{v_0 - v_k})^3 e^{-\frac{hcv_k}{K_B T}}$,

which is valid when a photon counter detector is used to detect the Raman signals. If energy-based detectors were used, the term needs to be changed to $(\frac{v_0+v_k}{v_0-v_k})^4$.

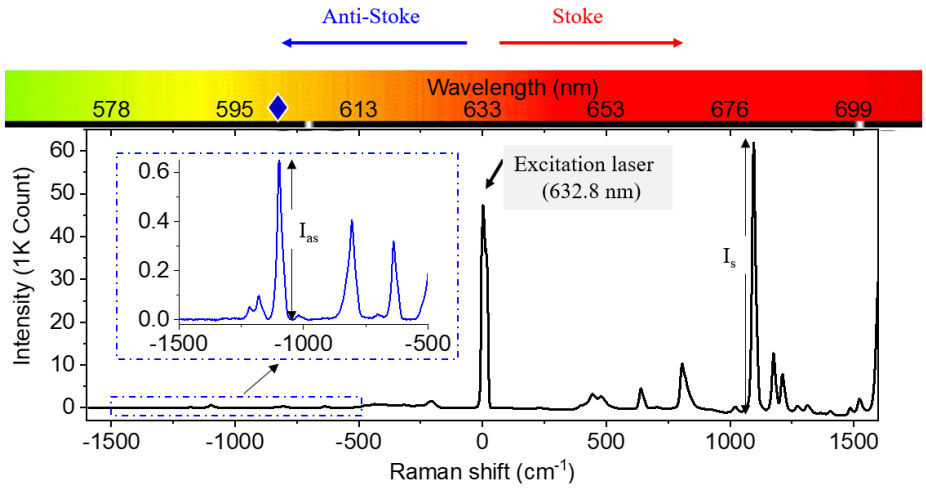

Figure 1-6 Raman spectra of 4-aminothiophenol powder. Here the laser source is a HeNe laser at 632.8 nm. Raman scattering with wavelengths higher than the incident laser, is called Stokes Raman scattering. On the other hand Raman scattering with wavelengths lower than the incident laser is called Anti-Stokes Raman scattering. The inset is the zoom-in of the dashed blue rectangle.

1.3 Overview of Emerged Techniques for Biological Application

Biomarkers analysis includes the extraction of meaningful data from monitoring intracellular, cell membrane-bound, and secreted circulating biomarkers. My dissertation aims to detect intracellular biomarkers as they are a building block of life. However, the concentration of biomarkers is low in the early stages of the disease. It's a challenge to reach such sensitivity. Moreover, the micron size and dynamic nature of live cells require that the probes for such analysis be sensitive in the nanoscale range and possess dynamic responsivity.[26, 27] The past several decades have seen several breakthroughs in analytical techniques to overcome these challenges, including fluorescence-based spectroscopy,[28]

dark-field scattering spectroscopy,[29] SERS,[30] and nanopore/nanoelectrode sensing.[31] Each sensing technique has the potential for single cell analysis and has its own unique advantages. Following is a brief overview of techniques other than SERS towards intracellular biomarkers sensing.

Fluorescence-based Spectroscopy/Microscopy

Fluorescence-based spectroscopy has been routinely performed for single-cell analysis. Especially, the fluorescence-based techniques like STORM[32] (stochastic optical reconstruction microscopy), PALM[33] (photo-activated localization microscopy) and FRET[34] (fluorescence resonance energy transfer) have been used in live cell studies and are capable of tracking individual molecules with high spatial and temporal resolution.[28, 35-37] To increase the specificity of fluorescence-based spectroscopy, one way is to monitor the dye molecules that can covalently and site-specifically bonded to biomolecules. The other way is to use green fluorescent protein (GFP) by fusion, which can measure Ca^{2+} changes[38] and local pH[39, 40]. However, there is a limited number of cell-permeant fluorophores[41] or construction techniques[39] that are required to allow intracellular sensing of live cells. Also, fluorophores have an intrinsic stability problem associated with photobleaching and blinking over long timescales. [42-44] Thus, there is a high demand for biological applications that could extend and complement the capabilities of the prevailing fluorescence microscopy by using novel methods and technologies.

Dark-field Scattering Spectroscopy

Plasmonic nanoparticles (NPs), e.g., gold NPs (AuNPs) and silver NPs (AgNPs), exhibit unique optical properties because of the phenomenon called localized surface plasmon resonance (LSPR)[45]. Thus, plasmonic NPs have been widely applied in

biological imaging and sensing. The scattering spectra of single plasmonic NPs can be monitored by dark-field scattering spectroscopy, which has been intensively used for plasmonic NP-based nanosensors.[46] The most promising advantage of dark-field scattering spectroscopy over fluorescence microscopy is its ability to sense cellular processes over long periods of time without phototoxicity.[29] Meanwhile, because of the scattering of plasmonic NPs being highly dependent on their sizes and shapes, the uniformity and stability of NPs in biospecimens are crucial for reliably sensing. Unfortunately, accurate morphology control at a large scale is not that easy. Additionally, plasmonic NPs (high-index material) will easily cause mechanical and photothermal damage due to light illumination to biological specimens[47] and uncontrollable aggregation in cells.

Nanopore/Nanoelectrode

Nanopore/nanoelectrode probes are utilize ionic or electrochemical current to measure intracellular biomolecules. The nanopipette is intensively used in the construction of various nanopore/nanoelectrode nanosensors. The nanoscale pore located at the sharp tip and carbon/gold deposited on internal or external surfaces of a nanopipette can be used as the nanopore/nanoelectrode platform for single cell sensing. For example, consider nanopipette-based nanopores for pH sensing at the single-cell level[48] and wireless nanopore electrodes for NADH analysis, which were pioneered by Professor Yitao Long's group. [31, 49, 50] Moreover, the glucosidase activity of isolated single lysosomes from a living cell was also tested by the electrochemical signal.[51] Different from light-based sensing methods, electric signals may have introduced more noise, and processing their

data is difficult. Another disadvantage of nanopore/nanoelectrode is that they are highly geometry and size dependent, which is hard to control at the nanometer dimension.

1.4 Overview of Research Projects and Results

The ultimate goal of my dissertation is to understand the fundamental aspects of SERS enhancement and develop a SERS-based nanoprobe for single-cell studies. To achieve these goals, in the beginning, the sensitivity of a home-made SERS instrument was tested. The first project (P1) is single-molecule detection by utilizing Au nanoparticles (NPs) on a curved electrode surface configuration to limit the NP numbers in the laser spot. Meanwhile, a correlation study was conducted between electrochemical current and SERS to monitor the dynamic formation of the plasmonic junctions. The second project (P2) investigates electromagnetic and chemical enhancement factor tuning by the electrode potential with the assistant of Ag. The last project (P3) is the design of a SERS-based nanoprobe for biomarkers detection and the effort towards single-cell analysis. The timeline of those projects is shown in table 1-3.

Table 1-3 The timeline of projects studied in this dissertation.

Projects		**2016 - 2017**	**2017-2018**	**2018 - 2019**	**2019-2020**	**2020.09**
P1. Single-molecule detection by SERS			Finished			
P2. Electrochemical-SERS	Electrochemical active/inactive molecule				Submitted	
P3. Biomarker detection by SERS	pH (H^+) sensor				Finished	
	H_2O_2 sensor				Ongoing	

	Glucose sensor				Ongoing	
Ph.D. Dissertation defense						

1.5 Reference

1. Nie, S. and S.R. Emory, Probing Single Molecules and Single Nanoparticles by Surface-Enhanced Raman Scattering. Science, 1997. **275**(5303): p. 1102-1106.

2. Kneipp, K., et al., Single Molecule Detection Using Surface-Enhanced Raman Scattering (SERS). Physical Review Letters, 1997. **78**(9): p. 1667-1670.

3. Park, J.-E., J. Kim, and J.-M. Nam, Emerging plasmonic nanostructures for controlling and enhancing photoluminescence. Chemical Science, 2017. **8**(7): p. 4696-4704.

4. Voge, N.V., et al., Metabolomics-Based Discovery of Small Molecule Biomarkers in Serum Associated with Dengue Virus Infections and Disease Outcomes. PLoS neglected tropical diseases, 2016. **10**(2): p. e0004449-e0004449.

5. Whiley, L. and C. Legido-Quigley, Current strategies in the discovery of small-molecule biomarkers for Alzheimer's disease. Bioanalysis, 2011. **3**(10): p. 1121-1142.

6. Liu, H.-W., et al., Recent progresses in small-molecule enzymatic fluorescent probes for cancer imaging. Chemical Society Reviews, 2018. **47**(18): p. 7140-7180.

7. Lee, Y.A., et al., Identification of Tumor Initiating Cells with a Small-Molecule Fluorescent Probe by Using Vimentin as a Biomarker. Angew Chem Int Ed Engl, 2018. **57**(11): p. 2851-2854.

8. Jun, Y.W., et al., Frontiers in Probing Alzheimer's Disease Biomarkers with Fluorescent Small Molecules. ACS Central Science, 2019. **5**(2): p. 209-217.

9. Goodacre, R., et al., Metabolomics by numbers: acquiring and understanding global metabolite data. Trends in Biotechnology, 2004. **22**(5): p. 245-252.

10. Urbanczyk-Wochniak, E., et al., Parallel analysis of transcript and metabolic profiles: a new approach in systems biology. EMBO reports, 2003. **4**(10): p. 989-993.

11. Holmes, C. and S. Lovestone, Long-term cognitive and functional decline in late onset Alzheimer's disease: therapeutic implications. Age and Ageing, 2003. **32**(2): p. 200-204.

12. Modrego, P.J., et al., Changes in Metabolite Ratios after Treatment with Rivastigmine in Alzheimer's Disease. CNS Drugs, 2006. **20**(10): p. 867-877.

13. Penner, J., et al., Increased glutamate in the hippocampus after galantamine treatment for Alzheimer disease. Progress in Neuro-Psychopharmacology and Biological Psychiatry, 2010. **34**(1): p. 104-110.

14. Raman, C.V. and K.S. Krishnan, A New Type of Secondary Radiation. Nature, 1928. **121**(3048): p. 501-502.

15. Raman, C.V. and K.S. Krishnan, A new class of spectra due to secondary radiation Part I Indian Journal of Physics, 1928(2): p. 399-419.

16. Atkins, P., J.D. Paula, and R. Friedman, Physical Chemistry: Quanta, Matter, and Change. 2013: Oxford Univ. Press.

17. Fleischmann, M., P.J. Hendra, and A.J. McQuillan, Raman spectra of pyridine adsorbed at a silver electrode. Chemical Physics Letters, 1974. **26**(2): p. 163-166.

18. Jeanmaire, D.L. and R.P. Van Duyne, Surface raman spectroelectrochemistry: Part I. Heterocyclic, aromatic, and aliphatic amines adsorbed on the anodized silver electrode. Journal of Electroanalytical Chemistry and Interfacial Electrochemistry, 1977. **84**(1): p. 1-20.

19. Albrecht, M.G. and J.A. Creighton, Anomalously intense Raman spectra of pyridine at a silver electrode. Journal of the American Chemical Society, 1977. **99**(15): p. 5215-5217.

20. Zrimsek, A.B., et al., Single-Molecule Chemistry with Surface- and Tip-Enhanced Raman Spectroscopy. Chemical Reviews, 2017. **117**(11): p. 7583-7613.

21. Michaels, A.M., Jiang, and L. Brus, Ag Nanocrystal Junctions as the Site for Surface-Enhanced Raman Scattering of Single Rhodamine 6G Molecules. The Journal of Physical Chemistry B, 2000. **104**(50): p. 11965-11971.

22. Wang, D., et al., Directional Raman Scattering from Single Molecules in the Feed Gaps of Optical Antennas. Nano Letters, 2013. **13**(5): p. 2194-2198.

23. Zrimsek, A.B., A.-I. Henry, and R.P. Van Duyne, Single Molecule Surface-Enhanced Raman Spectroscopy without Nanogaps. The Journal of Physical Chemistry Letters, 2013. **4**(19): p. 3206-3210.

24. Benz, F., et al., Nanooptics of Molecular-Shunted Plasmonic Nanojunctions. Nano Letters, 2015. **15**(1): p. 669-674.

25. Liu, Z., et al., Revealing the molecular structure of single-molecule junctions in different conductance states by fishing-mode tip-enhanced Raman spectroscopy. Nature Communications, 2011. **2**(1): p. 305.

26. Dittrich, P. and N. Jakubowski, Current trends in single cell analysis. Analytical and Bioanalytical Chemistry, 2014. **406**(27): p. 6957-6961.

27. Yuan, G.-C., et al., Challenges and emerging directions in single-cell analysis. Genome Biology, 2017. **18**(1): p. 84.

28. Weiss, S., Fluorescence Spectroscopy of Single Biomolecules. Science, 1999. **283**(5408): p. 1676-1683.

29. Qian, W., et al., Dark-field light scattering imaging of living cancer cell component from birth through division using bioconjugated gold nanoprobes. Journal of Biomedical Optics, 2010. **15**(4): p. 046025.

30. Willets, K.A., Surface-enhanced Raman scattering (SERS) for probing internal cellular structure and dynamics. Analytical and Bioanalytical Chemistry, 2009. **394**(1): p. 85-94.

31. Ying, Y.-L., et al., Asymmetric Nanopore Electrode-Based Amplification for Electron Transfer Imaging in Live Cells. Journal of the American Chemical Society, 2018. **140**(16): p. 5385-5392.

32. Rust, M.J., M. Bates, and X. Zhuang, Sub-diffraction-limit imaging by stochastic optical reconstruction microscopy (STORM). Nature Methods, 2006. **3**(10): p. 793-796.

33. Hess, S.T., T.P.K. Girirajan, and M.D. Mason, Ultra-High Resolution Imaging by Fluorescence Photoactivation Localization Microscopy. Biophysical Journal, 2006. **91**(11): p. 4258-4272.

34. Sekar , R.B. and A. Periasamy Fluorescence resonance energy transfer (FRET) microscopy imaging of live cell protein localizations. Journal of Cell Biology, 2003. **160**(5): p. 629-633.

35. Eigen, M. and R. Rigler, Sorting single molecules: application to diagnostics and evolutionary biotechnology. Proceedings of the National Academy of Sciences of the United States of America, 1994. **91**(13): p. 5740-5747.

36. Xie, X.S. and J.K. Trautman, OPTICAL STUDIES OF SINGLE MOLECULES AT ROOM TEMPERATURE. Annual Review of Physical Chemistry, 1998. **49**(1): p. 441-480.

37. Hess, S.T., et al., Dynamic clustered distribution of hemagglutinin resolved at 40 nm in living cell membranes discriminates between raft theories. Proceedings of the National Academy of Sciences, 2007. **104**(44): p. 17370-17375.

38. Miyawaki, A., et al., Fluorescent indicators for Ca2+based on green fluorescent proteins and calmodulin. Nature, 1997. **388**(6645): p. 882-887.

39. Llopis, J., et al., Measurement of cytosolic, mitochondrial, and Golgi pH in single living cells with green fluorescent proteins. Proceedings of the National Academy of Sciences, 1998. **95**(12): p. 6803-6808.

40. Han, J. and K. Burgess, Fluorescent Indicators for Intracellular pH. Chemical Reviews, 2010. **110**(5): p. 2709-2728.

41. Teng, K.W., et al., Labeling proteins inside living cells using external fluorophores for microscopy. eLife, 2016. **5**: p. e20378.

42. BERNAS, T., et al., Minimizing photobleaching during confocal microscopy of fluorescent probes bound to chromatin: role of anoxia and photon flux. Journal of Microscopy, 2004. **215**(3): p. 281-296.

43. Wright, A., et al., Singlet Oxygen–mediated Protein Oxidation: Evidence for the Formation of Reactive Side Chain Peroxides on Tyrosine Residues¶. Photochemistry and Photobiology, 2002. **76**(1): p. 35-46.

44. Song, L., et al., Influence of fluorochrome labeling density on the photobleaching kinetics of fluorescein in microscopy. Cytometry, 1997. **27**(3): p. 213-223.

45. Willets, K.A. and R.P.V. Duyne, Localized Surface Plasmon Resonance Spectroscopy and Sensing. Annual Review of Physical Chemistry, 2007. **58**(1): p. 267-297.

46. Xie, T., C. Jing, and Y.-T. Long, Single plasmonic nanoparticles as ultrasensitive sensors. Analyst, 2017. **142**(3): p. 409-420.

47. Li, Y., X. Liu, and B. Li, Single-cell biomagnifier for optical nanoscopes and nanotweezers. Light: Science & Applications, 2019. **8**(1): p. 61.

48. Özel, R.E., et al., Single-cell intracellular nano-pH probes. RSC Advances, 2015. **5**(65): p. 52436-52443.

49. Yu, R.-J., et al., Confined Nanopipette Sensing: From Single Molecules, Single Nanoparticles, to Single Cells. Angewandte Chemie International Edition, 2019. **58**(12): p. 3706-3714.

50. Gao, R., et al., Wireless nanopore electrodes for analysis of single entities. Nature Protocols, 2019. **14**(7): p. 2015-2035.

51. Pan, R., et al., Direct electrochemical observation of glucosidase activity in isolated single lysosomes from a living cell. Proceedings of the National Academy of Sciences, 2018. **115**(16): p. 4087-4092.

CHAPTER 2 METHODS AND MATERIALS

2.1 Chemicals

2.1.1 Solvent

Absolute ethanol (200 proof), Reagent alcohol (histology grade), and Acetone (99.9%) were purchased from Fisher scientific. All the aqueous solutions were prepared using deionized (DI) water (~18 M ohm, Ultra Purelab system, ELGA/Siemens).

2.1.2 Molecules for Surface Functionalization

Self-Assembled Monolayer Molecules on Gold Surface

8-amino-1-octanthiol (AOT) was purchased from Dojindo Molecular Technologies (Kumamoto, Japan). 6-Mercaptohexanoic acid (6-MHA), 6-Mercapto-1-hexanol (6-MCH, 97%), 16-Mercaptohexadecanoic acid (16-MHA, 90%), 4-Mercaptobenzoic acid (4-MBA, 99%), 4-Nitrothiophenol (4-NTP, 80%), Biphenyl-4,4'-dithiol (BPDT, 95%), and Biphenyl-4-thiol (BPT, 97%) were purchased from Sigma-Aldrich. 4,4'-Bipyridine (BYD, 98%), Thiophenol (TP, 99%), 4-Aminothiophenol (4-ATP, 97%), and silver nitrate (99.9%) were purchased from Alfa Aesar. 3-Hydroxybenzenethiol (3-HTP, 98%), 3-Mercaptophenylboronic acid (3-MPBA), and 4-Mercaptophenylboronic acid (4-MPBA) were purchased from Tokyo Chemical Industry Co., LTD. Thiolated poly (ethylene glycol) (HS-PEG, 5 kDa) was purchased from Nanocs, Inc.. Group 1 to 3 in Figure 2-1 is used for gold surface modification.

Silane molecules

(3-Aminopropyl) triethoxysilane (APTES, 99%) and (3-Mercaptopropyl) trimethoxysilane (MPTMS, 95%) were purchased from Sigma-Aldrich. Group 4 in Figure 2.3 shows the structure of the molecules.

2.1.3 Nanoparticles Colloid

Citrate protected 40, 60, 80 nm AuNPs and 20 nm silver nanoparticles (AgNPs) colloid were purchased from Ted Pella, Inc..

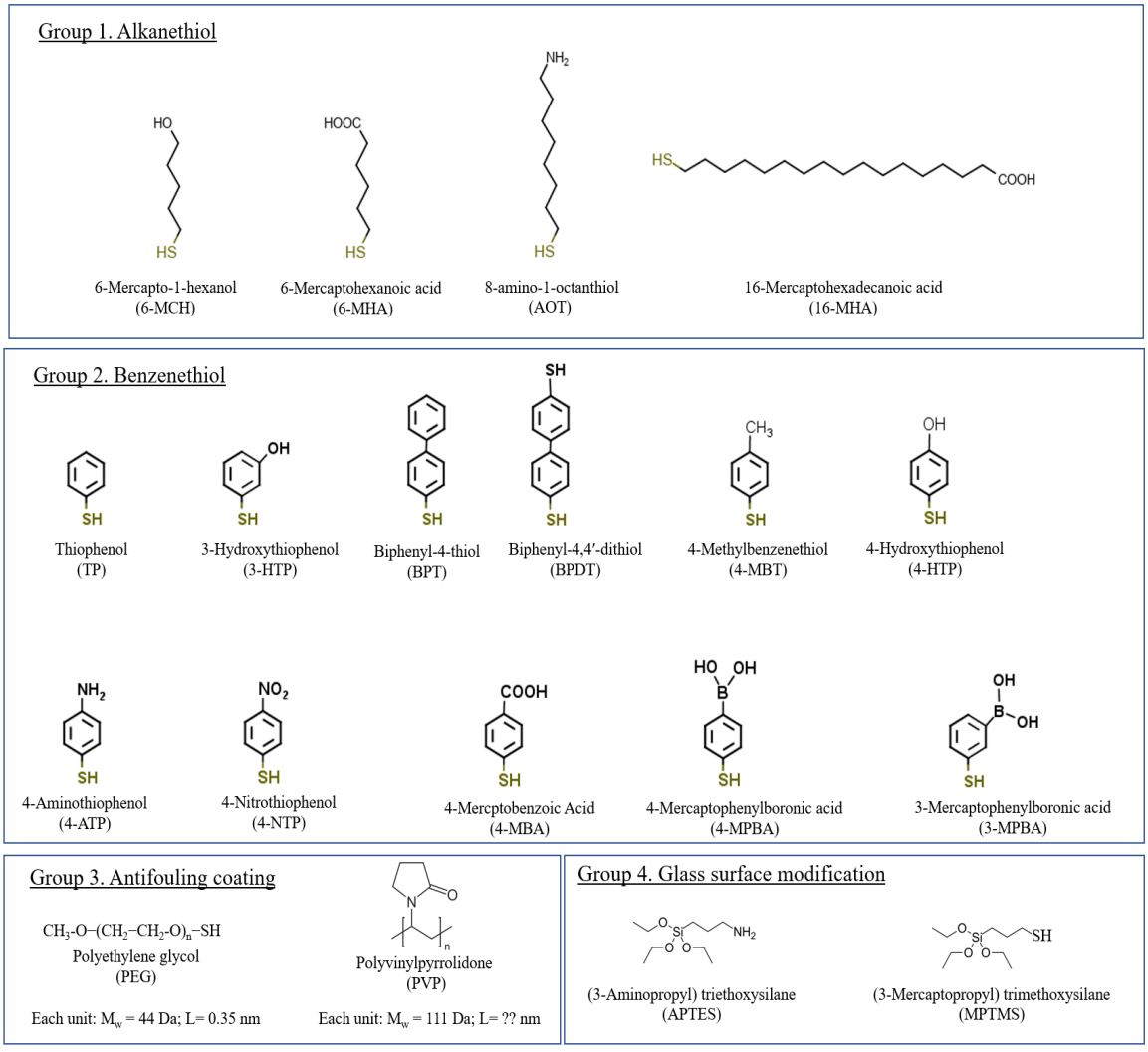

Figure 2-1 Molecules used in this dissertation and classified by their structure and applications.

2.1.4 Other Chemicals

Sodium chloride (NaCl, >99 %), potassium phosphate dibasic (K_2HPO_4), and potassium phosphate monobasic (KH_2PO_4) were purchased from Sigma-Aldrich. Phosphate buffered saline (PBS) powder (for pH 7.3−7.5), potassium chloride, reagent alcohol (histology grade), hydrochloric acid (HCl, ~37 %), and Sodium hydroxide (NaOH) were purchased from Fisher Scientific. Silver nitrate ($AgNO_3$, 99.9%) was purchased from Alfa Aesar. Potassium ferrocyanide (98.5% purity, $K_4[Fe(CN)_6]\cdot 3H_2O$) was purchased from Acros Organics (New Jersey, U.S.A.).

2.2 Instrumentation and Experimental Setup

2.2.1 Electrochemical Workstation

Instrument and Techniques

Model 760D Electrochemical Workstation from CH Instruments, Inc., USA. Techniques: Cyclic Voltammetry (CV)

The CV measurement setup was placed in a Faraday cage to reduce electrical noise. The main purpose of the electrochemical workstation in this dissertation was used to characterize the electrode/pore size and clean the gold electrode. These CV measurements were performed with three electrodes, the working electrode, the reference electrode, and the counter electrode. Here the fabricated Au electrode is used as the working electrode, an Ag/AgCl wire is the reference electrode and the Pt wire is the counter electrode.

2.2.2 Patch-clamp Amplifiers for Electrochemical Current Acquisition

Instrument and Mode

Axopatch_200B patch-clamp amplifier and Digidata 1440A were from Axon CNS Molecular devices Inc., CA. Function generator is the Model DS340 from Stanford research systems. The mostly used modes are V-Clamp and Cyclic voltammetry.

Electrochemical Current Measurement

The *I–t* measurement setup was placed in a suspended Faraday cage (Figure 2-2) on an optical table to reduce electrical noise and mechanical vibrations. An Axon 200B patch-clamp amplifier (Figure 2-3) in voltage-clamp mode was used to supply the bias and amplify the current. A 10 kHz Bessel low-pass filter was typically used for current measurements. An Axon Digidata 1440A (Figure 2-3) was used to record data at 50 kHz. The setup had the sensitivity to detect a current change of less than 1 pA with a temporal resolution better than 1 ms. The Au electrode was used as the working electrode. The Ag/AgCl electrode was grounded and used as the quasi-reference electrode.

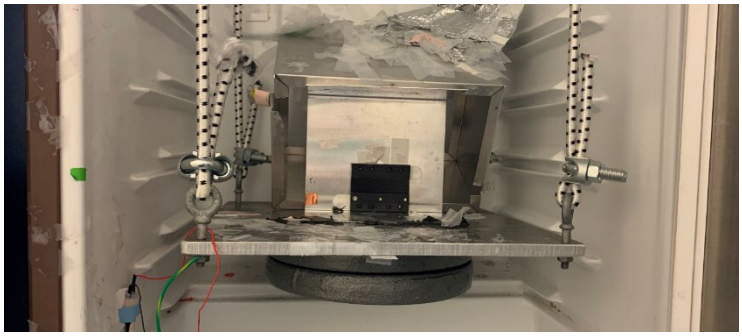

Figure 2-2 Suspended Faraday cage. Two electrodes electrochemical systems.

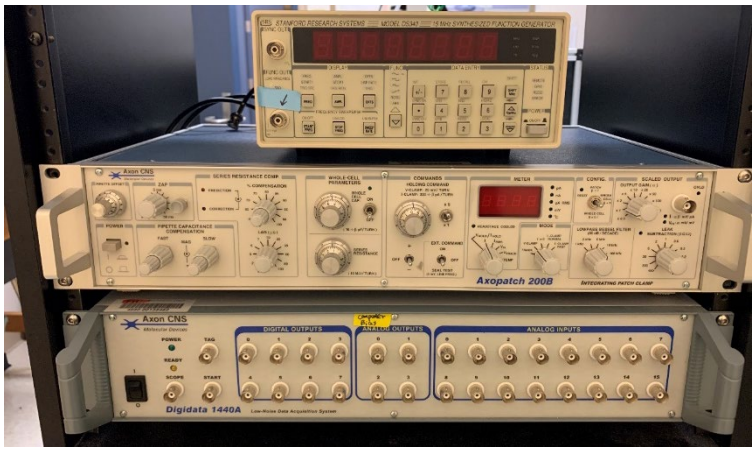

Figure 2-3 Instrument used for i-t measurement. Top: Function generator. Middle: Axon 200B patch-clamp amplifier. Bottom: Axon Digidata 1440A.

2.2.3 Nikon Optical Microscope-based Darkfield Microscope

Instrument

Nikon Inverted Microscope eclipse Ti-U as shown in Figure 2-4. Nikon Optiphot Labophot Dry Dark Field Condenser (0.95-0.80 NA). The home-built Darkfield microscope setup was obtained by changing the original condenser of the microscope to Darkfield condenser.

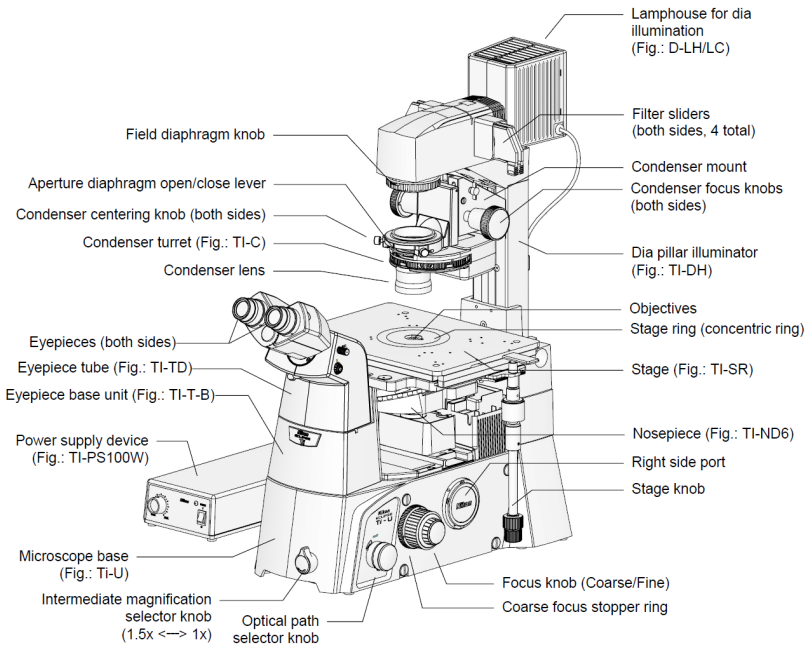

Figure 2-4 The illustration of Ti-S (Ti-U) microscope body. This image is from the Nikon company.

2.2.4 Nikon Optical Microscope-based Raman Spectroscopy

Raman spectroscopy

The home-built Raman microscope setup (Figure 2-5) was based on a Nikon Inverted Microscope body and an excitation laser from a HeNe laser (Melles Griot). If not mentioned otherwise, the excitation laser was set to 632.8 nm. Another excitation laser at 785 nm from a Volume-Holographic-Grating-(VHG) Stabilized pigtail Laser was also used. A dichroic beamsplitter was used to reflect excitation light to the sample through an objective lens (Nikon CFI Super Plan Fluor ELWD, 40x, 0.6 NA). The Raman signal was collected via the same objective lens and then passed through the dichroic mirror and a notch filter before being focused onto the entrance slit of a spectrograph (Acton SP 2356, Princeton Instrument, equipped with a grating 600 grooves/mm, blazed at 500 nm). The spectrum was recorded by a CCD camera (PIXIS 100B_eXcelon, Princeton Instrument).

The laser beam was focused on the bulk chemical for normal Raman spectroscopy. For Surface-enhanced Raman spectroscopy, the laser beam was focused on the Au tip electrode apex that was fixed in a liquid cell installed on a Nikon microscope sample stage. The spectral resolution was about 2 cm^{-1}.

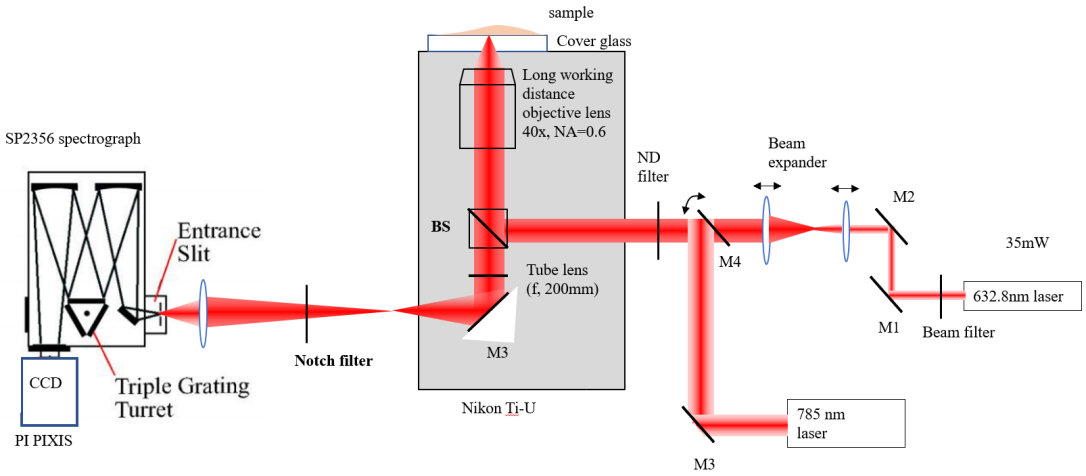

Figure 2-5 Illustration of Home-built Raman spectroscopy.

Laser intensity calibration

The power of the 632.8 nm and 785 nm excitation lasers were attenuated by different neutral-density filters. We rotated the ND filter wheel to select the slot marked as '1.3', which means it is an OD 1.3 ND filter. The laser spot size was about 3 μm. After the laser warmed up (~15 min), the total intensity on the microscope stage position was measured by a power meter. The typical area intensity was calculated and shown in Figure 2-6. The x-axis is the OD number of the ND filter. The y-axis is the corresponding area intensity obtained by total power divided by the laser focus area. Here different dichroic filters could be selected as the beamsplitter. Each one had its own application. If not

mentioned otherwise, the dichroic filter marked HeNe was used. It allows us to monitor Raman shift greater than 300 cm^{-1}. The dichroic filter is marked as "SP", which means both Anti-stokes and stokes Raman scattering can be observed. The dichroic filter marked as "633R" is used for monitoring Raman shift greater than 200 cm^{-1}. When a 633R dichroic filter is chosen, it is important that the corresponding Notch filter also needs to be replaced.

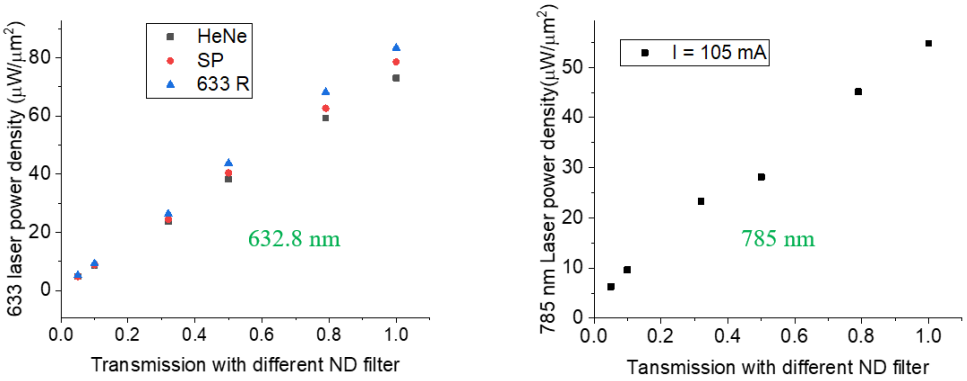

Figure 2-6 Laser intensity focused on samples for Raman spectroscopy.

Excitation Laser alignment

It is essential to check the alignment of the excitation laser regularly. Here is the procedure for the alignment.

a) Block the laser beam entrance to Nikon Microscope with a piece of black cardboard. Turn on the HeNe laser switch key. Warm-up laser for at least 15 min.

b) Turn on Nikon illumination white light Halogen lamp; select the dichroic filter marked as 'HeNe', to reflect red light. The other one marked as 'M' shows a better optical image. However, do not use it for Raman spectroscopic measurement, because its transmission of a broad spectral window centered at 633nm is low.

c) Place a glass cover slide at the Nikon sample stage position; alternatively, use the bottom of home-made sample cell for living cell imaging. Translate the objective lens

up close to focus on the back of the cover slide, and you should see a clear image of dust. For Raman measurement, a 40x objective lens is preferred.

Hint: Keep in mind that the fine focus knob (the small one, 0.1 mm/rotation) is used to get a clear image of the sample. Don't move the coarse focus knob (large one, 5mm/rotation) out of the adjustment range. Turn the knob counterclockwise to move the stage up, and turn it clockwise to move the stage down.

d) Place a box on sample stage to block the scatter of HeNe laser out of the sample glass. For example, use the Faraday cage to cover the sample, but leave the white light to illuminate the sample.

e) You can attenuate the Nikon's illumination white light with the controlling knob, or simply blick it completely by placing a piece of cardboard on top of the sample box.

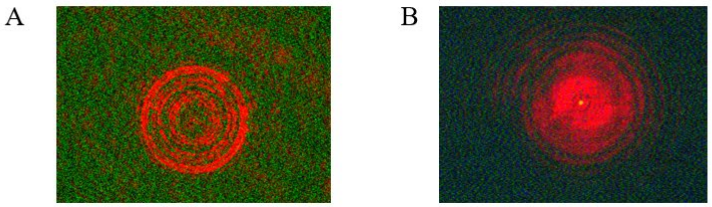

Figure 2-7 (A) Newton Ring, when the objective lens is focused on the cover glass slit; (B) Newton Ring from the back reflection of the objective lens when the objective lens is defocused to sample position.

f) Rotate the ND filter wheel to select the slot marked as '2.5', which means it is an OD 2.5 ND filter. Place the linear ND filter into the beamline. Open the iris in front of the entrance port. Remove the cardboard to allow the HeNe laser beam enter the Nikon microscope. You should be able to see the optical image of Newton rings on the uEye CCD camera, which connects the right port of the Nikon microscope (Figure 2-7A).

g) Slightly open and close the iris that is located at the laser beam entrance port to verify that the laser beam is centered at it. If it is, the beam will markd the center on the coputure screen. If not, adjust the x-, y- translation knob of the steering lens to center the beam to the iris.

h) Move the objective lens down; Take off the linear ND filter. You should see the Newton ring formed by the back reflection of the objective lens (Figure 2-7B). The ring width is larger than that in step f), because the beam is not focused on the camera. Check whether the center of these rings is located at the same spot as the front focusing spot marked in step f). Check if the laser beam is centered on the iris. If it is off, center it to the iris as in step f). Note: normally the image in this step is weaker than that in Step f). You can choose an an ND filter with a lower OD number to get more photons to enter the setup.

i) Move the objective lens up to focus on the glass cover slide at the sample stage again. Check the center position of the laser spot. It should overlay well with that obtained in step g). If not, iterate between step f) and g) a couple of times. When you are satisfied with the alignment, mark the final laser focusing spot on the monitor. These steps of optimization ensure that the excitation laser beam goes through the objective lens perpendicularly.

2.2.5 Simultaneous Electrochemical Current and SERS Measurements

The synchronization of optical and electrical measurements was achieved by two methods: (1) sending an external trigger signal (generated by a Labview program) to both the CCD camera and the Axon Digidata 1440A. (2) Sending a trigger signal from CCD camera to the current recording instrument Axon Digidata 1440A when starting the

acquisition of Raman data. It should be noted that the electrical noise of simultaneous measurements was about three to five times higher than that of separate electrochemical current measurements. This was not induced by laser irradiation because the on/off of the laser did not impact the current noise level. The increased noise was attributed to the less effective electrical shielding by the small Faraday cage on the microscope stage. The sampling rate was reduced to 10 kHz, and a moving average filter was used in data analysis.

2.3 AuNE Fabrication

The Gold nanoelectrode (AuNE) was fabricated in two steps: (1) electrochemical etching and (2) partial insulation by high-density polyethylene (HDPE) or wax. The gold electrode size depends on the coating material, temperature, speed, and shape of the Au Tip. After the characterzation of the fabricated gold electrode, size can be estimated based on electrochemical current and SEM images.

2.3.1 Au Tip Preparation by the Electrochemical Etching Method

Materials

0.2 mm, 99.99% Au wire was purchased from Electron Microscopy Sciences. 0.254 mm, 80% platinum (20% iridium) was from California Fine Wire company. Window high-density foam seal tape and polyethylene foam are used to store etched Au tips. Gauge 25 regular 304 stain steel tube: ID ((.0095/.011) and OD .02/.0205) was bought from Component Supply.

Chemicals

37% Hydrogen Chloride (HCl) and reagent alcohol (EtOH).

Gold etching reaction

$4Au + 8HCl + O_2 \rightarrow 4\,HAuCl_2 + 2H_2O$

Prepare Etching Solution for Au Tip

a) The volume ratio of HCl and alcohol is V(HCl):V(EtOH) = 1:1. Usually, 20 mL HCl and 20 mL alcohol are mixed in a 50 mL plastic centrifuge tube. Note: the use of alcohol is because it's a lower surface tension solution and doesn't form bubbles during the reaction.

b) Use a vortex mixer to homogenize the mixture.

c) It seems to be that the presence of Au ions in the solutions improves etching conditions. Usually, first attempts to etch Au wire are not successful, but when the solution becomes yellow, the results become much better. Thus, to avoid failed first attempts next time, withdraw several mL of yellow etching solution into the freshly prepared etching solution.

Equipment and Connections

Figure 2-8A and B show the AC etching controller and etching stage. They were homemade instruments. Figure 2-8C shows the schematic drawing of the connection between Au wire and Pt wire circle to the tip of the etching controller. The Pt wire circle must just touch the etching solution top surface and hold the etching solution by surface tension and be parallel with the solution surface. The gold wire should dip into the center of the Pt wire circle and extend below the etching solution surface by about 2-3 mm.

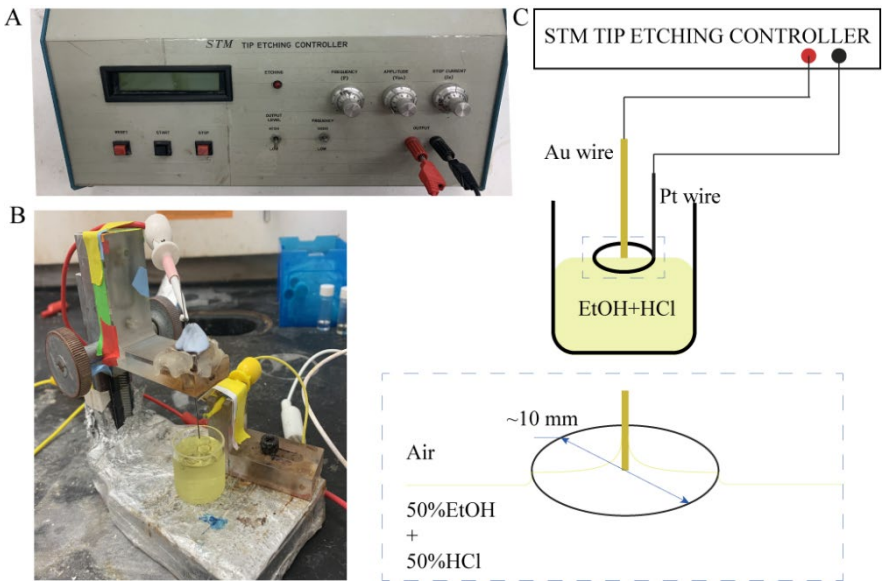

Figure 2-8 Electrochemical etching setup. (A) The optical image of the tip etching controller is also called a scanning tunneling microscope (STM) tip etching controller. (B) Optical image of the stage of the Au tip etching setup, which connects to the tip etching controller with the wires. (C) Illustration of the Au tip etching setup and zoomed in the interface of air and solution.

Etching Procedure

a) The Au tip etching controller provides a square wave AC voltage with a maximum frequency of 4.7 kHz and amplitude around 25.5 V. Adjust "FREQUENCY (F)" and "AMPLITUDE (V_m)" to desired values (shown in the meter). For the HIGH "OUTPUT LEVEL" toggle, set the amplitude to 25.5 V. For the LOW "OUTPUT LEVEL" toggle, set the amplitude to 13.6 V. For the HIGH "FREQUENCY" toggle, set the frequency to 4.2 kHz. The LOW "FREQUENCY" toggle is not used. Switch the "OUTPUT LEVEL" toggle switch to HIGH, "FREQUENCY" toggle switch to HIGH.

b) Set the "STOP CURRENT (Is)" to the minimum value, about 2-3 mA.

c) Immerse the gold wire into the etching solution (2-3 mm below the etching solution surface).

d) Press the “START” button and check the current display in the meter display. The initial

current should be around 300 mA or higher.

Note: the shape and sharpness at the tip end could be optimized by varying the initial biggest current from 300 mA to 500 mA via changing the length of immersed gold wire in the etching solution. The etching voltage and frequency may also affect the tip shape and sharpness. In addition, there shouldn’t be any vibrations of the tip, nor should there be evolution of big air bubbles. Bigger bubbles indicate instability of the solution level at the end of the tip, and resulting tips are usually bad.

e) During etching, the sound from the electrochemical etching of gold can be heard (if not, check wire connections). When the sound disappears, the etching is finished. The etching process is about 1 minute.

f) Rinse the tip with tap water, inspect the tip under an optical microscope (up to x20). Compare the shape with the sketch shown in Figure 2-9 and continue accordingly.

Figure 2-9 Sketch of the Au tip shape possibilities under an optical microscope. (A) Good. (B) Needs a second time etching, continue with step g). (C) Need to restart from the beginning, step a).

g) Second step etching may be needed when the shape is not good at the first-time etching (for example, shape B). Push the “OUTPUT LEVEL” to LOW. The current should be about 20-80 mA. To re-immerse the Au tip, lower it carefully to just touch the etching

solution surface and then immediately (about 0.25 s) pull the tip out of the etching solution after etching start. You may get tip A or tip C in Figure 2.3.

h) If you get shape C, you need to totally remove the tip by a cutter and redo etching from step a).

2.3.2 Insulator Coating of Au Tip

Just before insulation, etched Au Tips need to be cleaned. Our etched Au Tip was cleaned by piranha acid $V(H_2SO_4):V(H_2O_2) = 3:1$. (Piranha solutions are highly corrosive and need to be handled with extreme caution!) for 10 min, rinsed by plenty of DI water, and dried in an Argon flow. Figure 2-10 shows the method used for Au Tip cleaning.

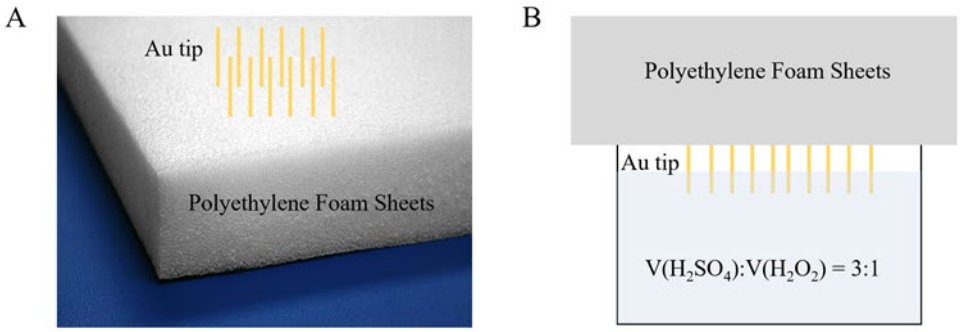

Figure 2-10 Illustration of steps for Au tip cleaning. (A) Insert etched Au tip into the polyethylene foam sheet. (B) Invert the polyethylene form onto a glass Petri dish filled with a piranha solution.

In the second step, the cleaned tip was insulated with high-density polyethylene (HDPE) or wax. Figure 2-11 shows the setup for HDPE or wax insulating of the Au Tip. The temperatures of the "heating plate" for HDPE and wax coating were set to 220 °C and 120 °C, respectively. As Figure 2-11C shows, a Au tip will go through the melted HDPE or wax and pull out from the heating plate. Wax insulation allows Au tip to go back and forth through melted wax without damage to the Au Tip apex, and thus the exposure area

can be controlled to be very small. On the other hand, HDPE insulating only allows one-time coating, but it can be more stable than wax if immersed in an organic solvent such as alcohol. For a molecule that is used with gold surface modification and only dissolved in alcohol, HDPE coated nanoelectrodes should be used. After cooling down, the solid HDPE and wax will shrink and leave the Au Tip apex exposed. Many factors will affect the final exposure area: properties of HDPE and wax, heating temperature, movement speed, and timing. More details about electrochemical etching, insulation, and characterization of the Au Tip electrode can be found elsewhere[1].

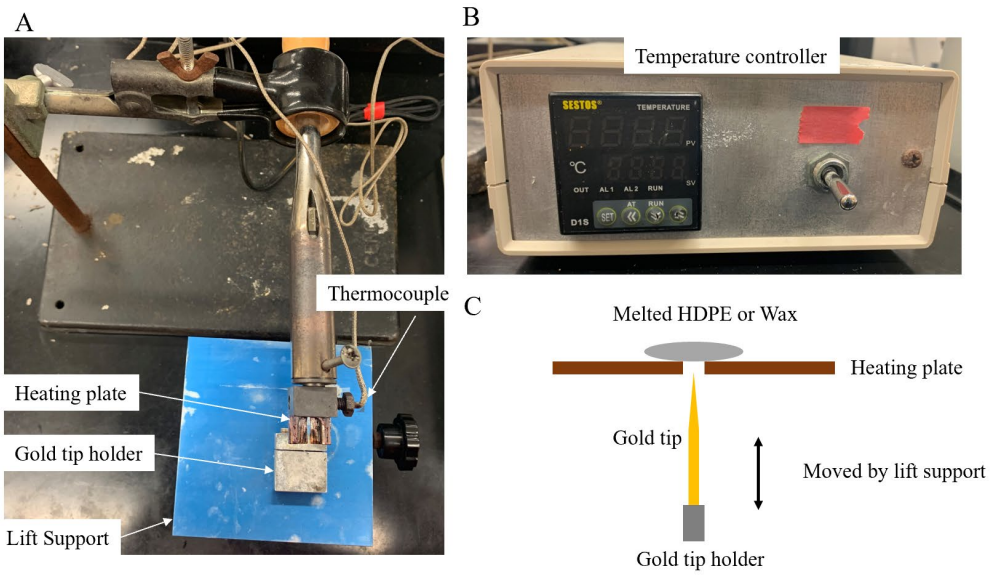

Figure 2-11 Experimental setup for Au Tip insulation. (A) Optical image of experiment setup with text indicating the purpose for each component. (B) A homemade temperature controller which was made by our electrical technician Norman. (C) Sketch of the insulator coating process.

2.4 AuME on Chip Fabrication

Gold microelectrode (AuME) was fabricated on 4-inch SiO_2 fused silica wafers in FIU cleanroom. The brief procedure is a) pattern design; b) AuME fabrication by lift-off; c) Making Su 8 reservoirs by photolithography.

2.4.1 Make Glass Mask by Mask Maker

Before proceeding, design the pattern of AuME and reservoir on Autocad software, respectively, and save as the format of *.dxf 2000. Use Layout software provided by FIU cleanroom to open the file, check every detail, and add all design on the same layer. Using the computer, which connected with the Mask maker (μPG 101) instrument to download the file and rename the design file, make it as easier as possible. It was loading the design file to the software(μPG) on the computer desktop. Then, loading the 5-inch glass substrate (It should be purchased on Fiufom before use) to the Mask maker instrument (detail see the manual of Mask maker).

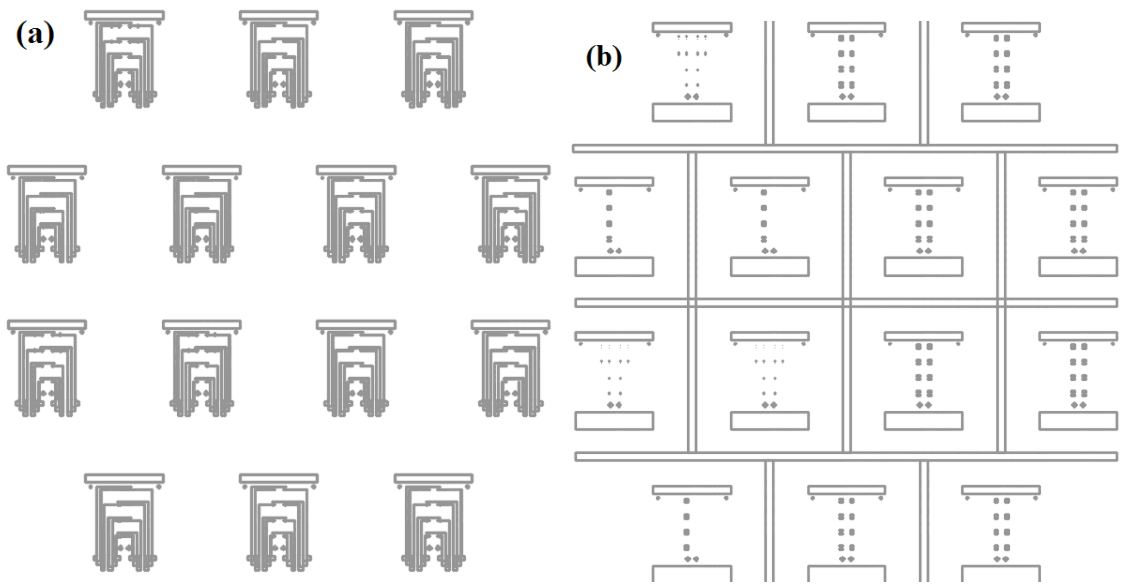

Figure 2-12 The screenshot from Autocad software. (A) The design of AuMEs. (B) The design of reservoirs.

2.4.2 Metal Deposition by Lift-off.

Mask aligner

a) Use ethanol and IPA solvents to clean the 4-inch fused silica by spin coater. (Set the speed of spin coater: First spin speed: 500 rpm, time: 5 s; Second spin speed: 3000 rpm, time: 30s.)

b) Spin coating the photoresist of AZ 1512 on cleaned silica wafer. (First spin speed: 500 rpm, time: 5 s, ramp 250 rpm/s; Second spin speed: 3000 rpm, time: 30s, ramp: 3000 rpm/s.) Note: Do not use adhesion promoter HMDS here.

c) Soft bake on a hot plate at 105℃ for 60 s.

d) Expose at a dose of 70mJ/cm^2. After exposure, the wafer is post-baked on a hot plate 105℃ for 60 s.

e) Immerse the wafer in AZ 300 MIF solvent and develop for 45 s. Check the patterns under the optical microscope.

f) RIE removes the photoresist residues: MARCH 1701. (Press: 400mtorr, power: 100W, time: 40s.)

Metal deposition by E-beam evaporator

Instrument: CHA RAP 600 EVAPORATOR. First, Ti： 5 Å/min, and target thickness: 200A; Au: 5 Å/min, target thickness: 500A.

Lift-off

Soak the wafer in PG remover and followed by DI water rinse. Use ultrasonic if necessary.

Chip cleaning

Before the next step, use RIE clean the chip: MARCH 1701. (Press: 400mtorr, power: 100W, time: 40s.)

2.4.3 Fabricate Solution Reservoirs by Photolithography

a) Spin coat Su 8 photoresist. (First spin: the speed at 500 rpm for 5-10 s with an acceleration of 100 rpm/s; Second spin: the speed at 3000 rpm for 30 s with an acceleration of 300 rpm/s).

b) Prebake on a hotplate at 95 ºC for 10 min.

c) Mask Aligner: (OAI 800 Mask Aligner.) Using microscopy to focus and align the maker. The exposure dose is 175 mJ/cm^2.

d) Post Exposure Bake (PEB) on a hot plate at 95 ºC for 3 min.

e) Rinse and Dry: when using SU-8 developer, spray/wash the developed image with fresh developer solution for approximately 10 s, followed by a second spray/wash with isopropyl alcohol (IPA) for another 10 s. Air dry with filtered, pressurized air or nitrogen.

f) Inspection under a microscope, as shown in Figure 2-13.

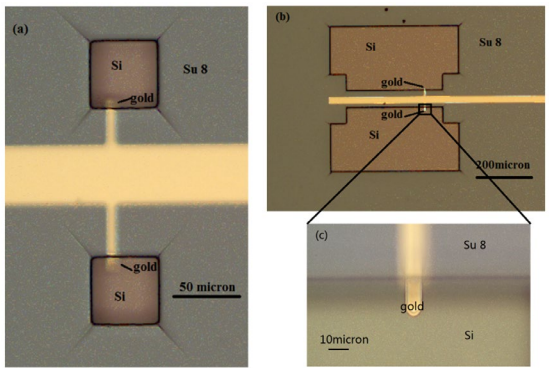

Figure 2-13 Optical images of fabricated AuMEs.

Problems

a) The Alignment has 2-5 μm bias.

b) After completing the fabrication of AuME, a long time and high power oxygen plasma treatment to the gold surface also will damage the Su 8 surface. This damage will lead to leak when using the PDMS microfluidic device to drive the solution to a reservoir (7 w and less than 2 min seem OK, as no leakage current between two reservoirs).

2.5 Glass Nanopipette Preparation

The borosilicate glass capillary with filament (O.D.: 1.0 mm, I.D.: 0.58 mm, 15 cm length, Sutter Instrument Co.) was cleaned by piranha solution (caution: piranha solutions are highly corrosive and need to be handled with extreme caution!) for 30 min. Then rinsed by DI water both inside and outside thoroughly and dried in an oven at 120°C overnight. Glass nanopipettes were prepared from the cleaned glass capillaries by using a laser-based pipette puller (P-2000, Sutter Instruments) as shown in Figure 2-14. Nanopipette with different apex size and flexibility were prepared by using different pulling parameters. There are some general rules for the parameter setting:

1. HEAT, will affect the length and tip size of the pulled nanopipette. Higher HEAT setting tends to give longer and finer tips. Borosilicate glass with proper melting requires the “HEAT” values ranging from 250 to 500.

2. FILAMENT, should be used as “0” to pull electrospray tips.

3. VELOCITY, the suggested range is 15-50.

4. DELAY, controls the amount of time the glass has to cool before the program end.

5. PULL, the greater the pull, the smaller the resulting tip.

The pulling parameters used in this dissertation are shown as following:

Nanopipette i (~1 μm): HEAT = 280, FIL = 4, VEL = 50, DEL = 255, PUL = 100.

Nanopipette ii (~500 nm): HEAT = 400, FIL = 4, VEL = 50, DEL = 255, PUL = 100.

Nanopipette iii (~200 nm): HEAT = 500, FIL = 4, VEL = 50, DEL = 255, PUL = 100.

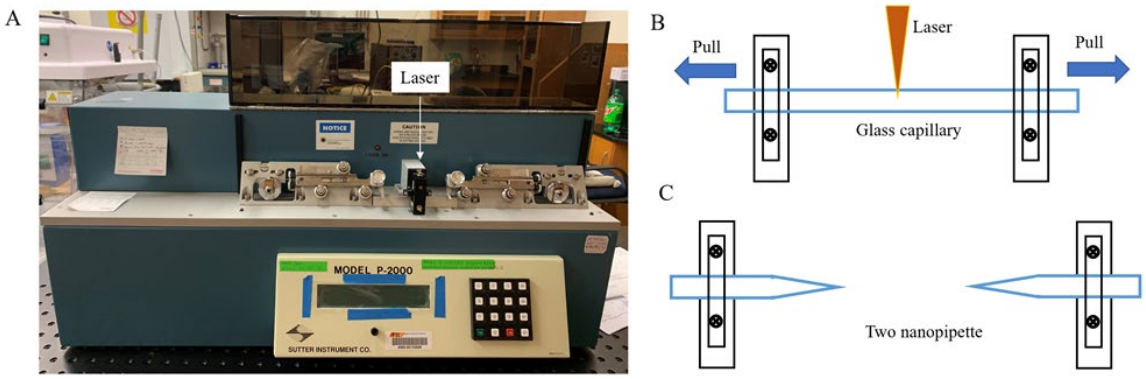

Figure 2-14 Nanopipette fabrication. (A) Optical image of the puller instrument for nanopipette fabrication. The P-2000 contains a 20 W Class IV CO_2 laser with a 3.5mm diameter beam. (B) Illustration of the working mechanism of the puller.

2.6 AuNE and AuNPs Characterization

2.6.1 AuNE Exposure Area Characterization

The fabricated Au Tip electrode was characterized by an optical microscopy, scanning electron microscopy (SEM, JEOL JSM 6335F), and cyclic voltammetry (CV)[2]. Figures 2-15 show the optical microscope and SEM images, for one example Au Tip electrode with wax and HDPE coating. Wax is totally black and HDPE much more transparent. From SEM images, the surface curvature of the tip is about 156 nm. Due to the severe charging

effect on the insulated Au tip electrode with small exposed apex, it needs to be coated with the gold layer before SEM imaging. The addition of gold layer process takes time and ruins the insulator for SEM imaging. Instead, we estimated the effective surface areas (or exposed areas) of the insulated Au tip electrode based on CVs. The steady-state CVs of the Au Tip electrode were recorded in 1 M KCl solution containing 100 mM Ferrocyanide by cycling the electrode potentials (10 mV/s) using a potentiostat (CHI760D). The diffusion-limited current I_d is calculated using the equation $I_d = m\ F\ D\ C\sqrt{2\pi A_{eff}}$ [3]where A_{eff} is the exposed area, m is a geometry factor, F is the Faraday constant (96485 C/mol), D and C are the diffusion constant (7.4×10^{-6} cm^2 /s) and bulk concentration of Ferrocyanide ions, respectively. The geometry factor m = 1 if the electrode is hemispherical. For other geometries, such as inlaid disc, sphere cap, and hemispheroid, m changes slightly (normally less than 10%). For example, m = 1.1 if the aspect ratio of an oblate hemispheroid is 6. Therefore, we used m=1 for the calculation. We performed CV tests for all the insulated Au tip electrode. Figure 2-15C shows an example of CVs for one Au tip electrode. The effective exposed area for this Au tip electrode was 0.27 μm^2 (I_d=9 nA). Figure 2-15D shows the CV for different Au tip electrode, the effective exposing area were between 0.3 and 300 μm^2. For various applications, a Au tip electrode with a different exposing area can be chosen.

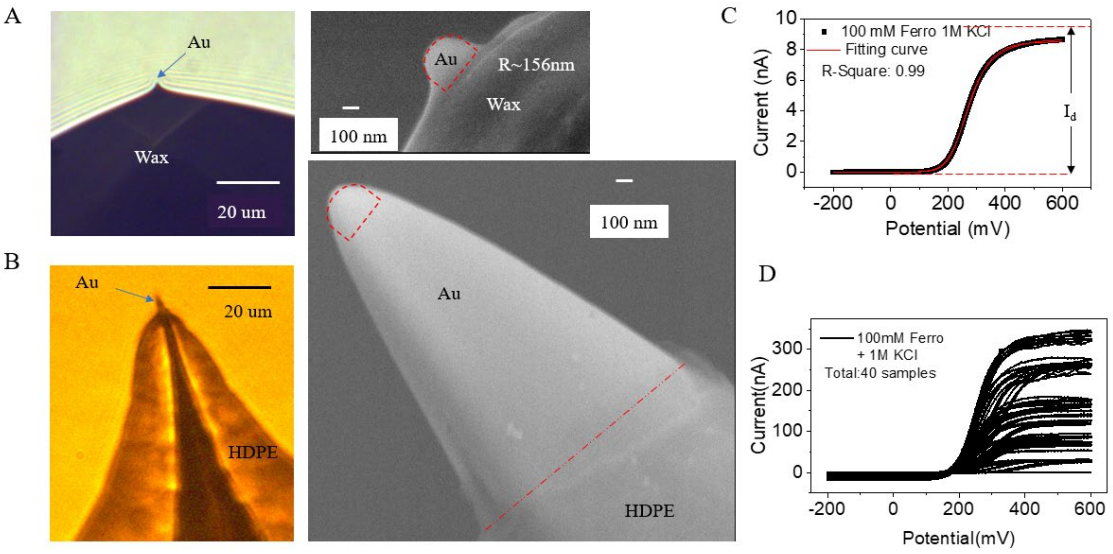

Figure 2-15 Wax and HDPE coated Au Tip. (A) Optical and SEM images of wax-coated Au Tip. (B) Optical and SEM images of HDPE coated Au Tip. (C) Example of the CV curve of AuNE in the electrolyte of 100 mM Ferrocynaide and 1M KCl. Sweep rate: 100 mV/s. The diffusion current I_d is indicated in the figure. (D) The CV curve of 40 AuNEs, indicates the variation of size of AuNE.

2.6.2 AuNPs Size and Surface Charge Characterization

The claimed diameter of 40 nm AuNPs from Ted Pella is confirmed using the transmission electron microscopy (TEM) imaging method. We further calibrate the size and zeta potential of AuNPs by Dynamic Light Scattering (DLS) measurement and SEM imaging. Figure 2-16 shows the size of AuNPs is around 50 nm, which is bigger than the claimed size, possibly owing to the surface charge effect on DLS and SEM measurement. The zeta potential is -103 mV.

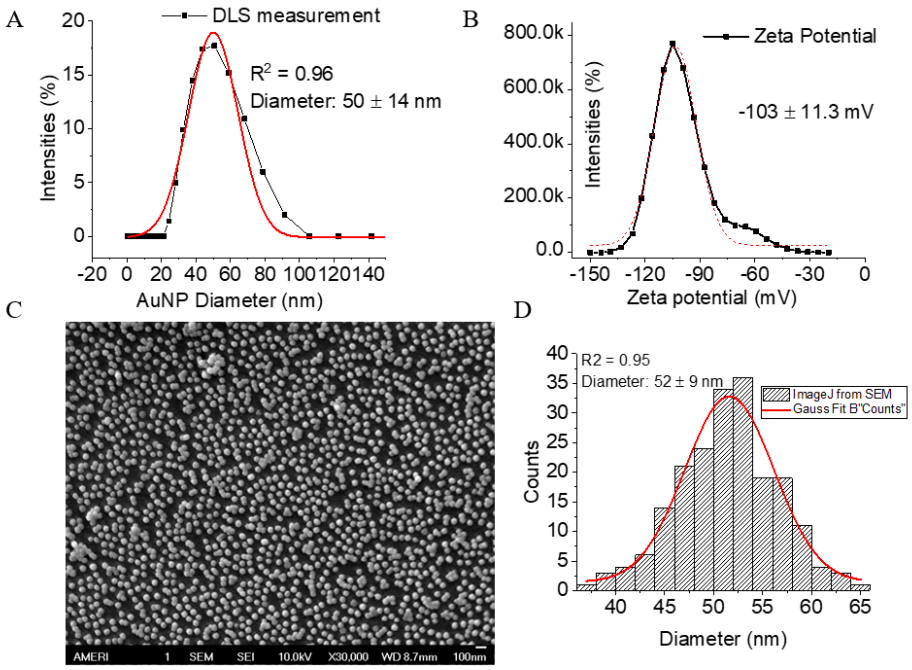

Figure 2-16 (A) Dynamic Light Scattering (DLS) values of the diameter of AuNPs, averaged over three measurements. (B) DLS values of the zeta potential, averaged over six measurements. (C) SEM image of AuNPs on a glass surface. (D) Size distribution is measured from the SEM image of (C) by ImageJ software.

2.7 Surface Functionalization

Due to low surface affinities or weak Raman cross-sections of analytes, surface modifications on SERS-active substrates are becoming more and more critical to achieving quantitative detection. Thiol-based molecules are one class of surface chemistries, they can self-assembled monolayer (SAM) on the surface of the SERS-active substrate. Group 1 in Figure 2-1 shows the thiol-based molecules used in this dissertation. More information about thiophenol-based molecules for SERS can be found in the review paper written by Dr. Qiuming Yu[4].

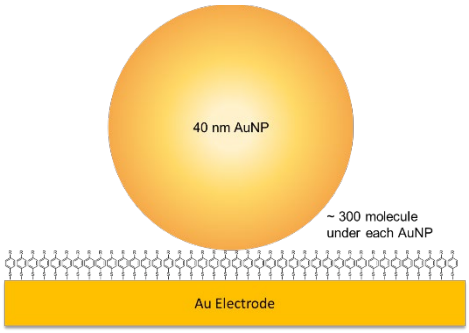

Figure 2-17 Illustration of a NPoNE configuration.

There are some important parameters that must be borne in mind to understand the overall configuration. Typical thiol-based molecular coverage[5] for SAMs is ~3 molecules/nm^2. As shown in Figure 2-17, a 10 nm^2 junction would contain ~30 molecules. The layer thickness of a SAM depends on the chemical structure. With one benzene ring, the layer thickness of the SAM is around 1 nm.

2.7.1 AuNPs Colloid Surface Functionalization

Figure 2-18 shows the procedure. First, prepare 1 mM thiol molecules in an alcohol solvent (NOTE: PEG needs to be dissolved in water). Second, 100 uL prepared thiol molecules solvent must bemixed with 1 mL citrate stabilized AuNPs (40 nm) for 2 hours at room temperature. Third, the molecule–AuNP solution is to be centrifuged at a speed of 5000 rpm for 10 minutes and rinsed 1-3 times to remove the excess molecules in the solution.[6]

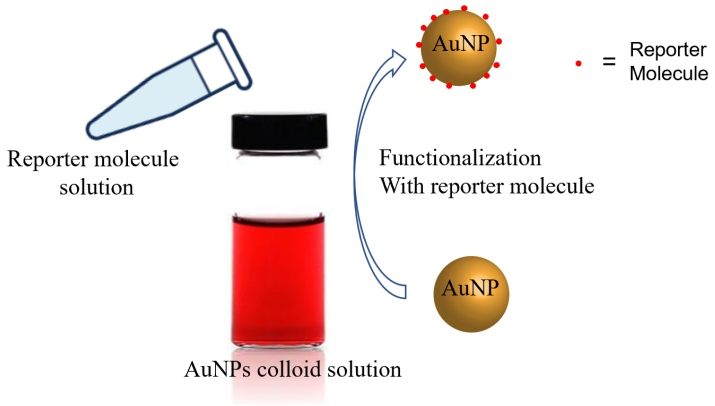

Figure 2-18 Schematic drawing of molecule modification of AuNPs colloid.

2.7.2 AuNE Surface Functionalization

For surface modification, the cleaned Au Tip electrode was immediately immersed in a freshly prepared molecule solution for a various times at room temperature. The experimental condition for surface modification of molecules was given in the Methods section of each chapter. Generally, the molecule molar concentration is 10 mM in reagent alcohol, and the modification time is overnight.

The SAM modified Au Tip electrode was rinsed with ethanol to remove physically adsorbed molecules, followed by DI water rinsing and drying in an Argon flow before measurements. Both the CV curve shape and diffusion-limited current i_d change after SAM modification (red curves in Figures 2-19). This is because the charge transfer from $Fe(CN)_6^{4-}$ to the Au tip electrode is hindered by the presence of the SAM at the Au tip electrode. The magnitude of i_d becomes proportional to the effective area NOT covered by molecules. Here is one example for 4-ATP modified Au tip electrode. Figure 2-19 suggests a full coverage modification of Au tip electrode by 4-ATP. The changes in CV shape and the reduction of saturation current confirm the presence of a molecule.

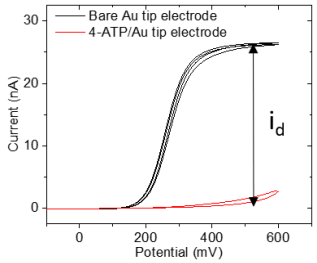

Figure 2-19 The CVs of three Au tip electrodes before molecule modification. The curves depict the CV of insulated Au tip electrodes both before (black) and after (red) 4-ATP modification.

2.7.3 Glass Nanopipette Surface Functionalization

First, prepare the silane molecules in alcohol just before using with a volume concentration used of 0.4%. Second, immerse the fabricated glass pipette into the prepared silane molecule solution for 2 hours at room temperature. Third, rinse the nanopipette with alcohol and dry it in an Argon gas flow.

2.8 Density Functional Theory Calculation for Raman Spectrum

Density functional theory (DFT) calculations of the Raman spectrum were carried out with the GAUSSIAN 09 software package. The structures were optimized using the built-in molecular mechanics, and the DFT calculations of these structures were performed at their ground-state equilibrium geometry conformation. The basis set of B3PW91 was used to calculate the static Raman spectra of molecules without heavy metal atoms. The mixed basis set of LANL2DZ and B3PW91 was used to calculate the static SERS of complexes of thiol molecules binding with Au3 clusters via the thiolate Ag-S bond. One example geometric configuration of the Au3-4-ATP complexes (Figure 2-20A) with a neutral charge and corresponding input file is shown in Figure 2-20B.

A

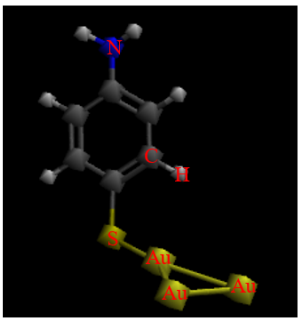

Au3-4-ATP

B

Allows a user-specified basis set Raman activity calculated

```
#t B3PW91/Gen Pseudo=Read opt freq=Raman
```

Key words

```
Title
```

Geometry optimization

```
0 1
C
C                    1     1.4082
C                    2     1.38499  1     120.57536
C                    3     1.4053   2     121.01584  1     0.1131
C                    4     1.40525  3     118.29436  2     359.92446
C                    5     1.38502  4     121.01554  3     0.07752
H                    2     1.08806  1     119.49333  3     179.76433
H                    3     1.08615  2     119.93151  1     180.42601
H                    5     1.08615  4     119.05503  3     180.38805
H                    6     1.08806  5     119.92566  4     179.64806
N                    1     1.38014  2     120.71486  3     182.25428
H                    11    1.01004  1     116.82609  2     338.18297
H                    11    1.01004  1     116.82506  2     199.34897
S                    4     1.7628   3     120.79719  2     176.21282
Au                   14    2.30769  4     104.32855  3     91.90106
Au                   15    3.61014  14    108.84509  4     149.09141
Au                   16    3.08049  15    68.24101   14    66.27911
```

Z matrix of complex structure

```
C H N S 0
6-31G(d)
****
Au 0
LANL2DZ
****
```

User-specified basis set

Figure 2-20 (A) Optimized geometry of Au3-4-ATP complex view, rendered with Avogadro software. (B) The input file to Gaussian 09 for Raman spectra calculation.

2.9 Finite-difference Time-domain Method Simulation

FDTD simulations were carried out by using a commercial software package (Lumerical Solutions, Inc.) We examined the plasmonic configuration for nanoparticles on the AuNE using the 3D-FDTD method. We tested the distribution of electromagnetic (EM) field strength surrounding an Au nanoparticle on a smooth Au surface. The incident light had a wavelength of 632.8 nm, and it was polarized in a direction that perpendicular to the underlying AuNE. There is on symmetric in the boundary condition. The boundary condition is perfectly matched layer (PML) except for the Z minimum, which is metal. Since there existence of facet for different size AuNPs[7], our model used the facet of 13 nm for 40 nm AuNPs. For the BPT monolayer, monolayer thickness 1.3 nm and refractive index of 1.45 were used as reported from previous research[8]. Figure 2-21 shows the region

of greatest field strength that happened in the junction between the AuNP and the electrode surface where the SAM would be located.

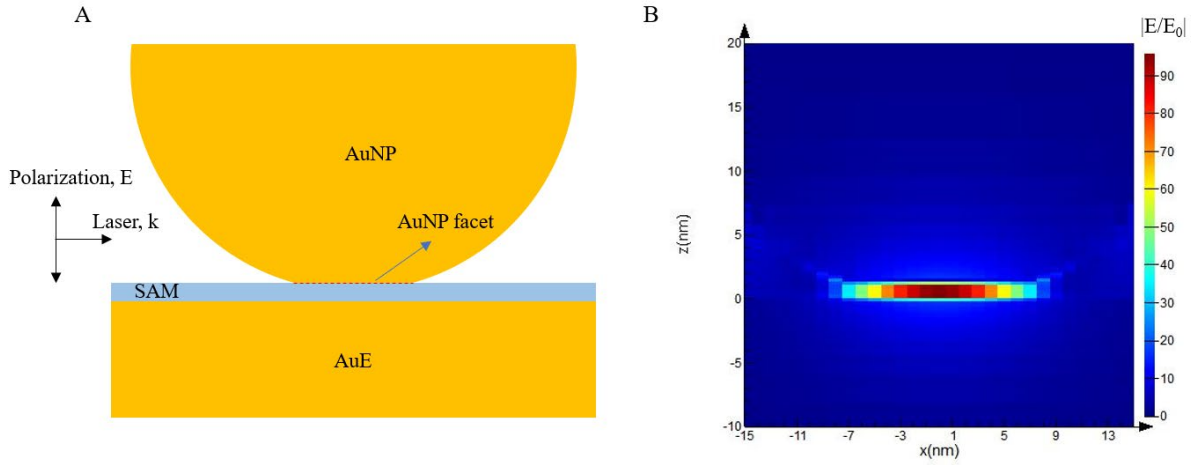

Figure 2-21 Simulations of the EM field surrounding a faceted 40 nm AuNP on the AuNE. The incident light had a wavelength of 632.8 nm. The polarization and boundaries of configuration were as shown. (A) Configuration of AuNP on AuNE. (B) Corresponding Electric field distribution.

2.10 Cell Culture

HeLa cells from human cells and fibroblasts from mouse cells were cultured in Dulbecco's Modified Eagle Medium (Gibco) with 10 % fetal bovine serum at 37 °C, 5 % CO_2, and 90 % humidity. The cells were seeded on the cover slides (pre-modified with 0.01 % poly-L-lysine to increase the cell adhesion). Before SERS measurement, the cells were gently washed two times with 1xPBS, and the culture medium was supplied with K_2HPO_4/KH_2PO_4 buffer with different pH values. 4 % paraformaldehyde was used to fix live cells for 10 min, and they were rinsed with 1xPBS.

2.11 Reference

1. Tuchband, M., et al., Insulated gold scanning tunneling microscopy probes for recognition tunneling in an aqueous environment. Review of Scientific Instruments, 2012. **83**(1): p. 015102.

2. Guo, J., et al., Monitoring the Dynamic Process of Formation of Plasmonic Molecular Junctions during Single Nanoparticle Collisions. Small, 2018. **14**(15): p. 1704164.

3. Vanýsek, P., Modern techniques in electroanalysis. 1996, New York: Wiley.

4. Sun, F., et al., Multi-functional, thiophenol-based surface chemistry for surface-enhanced Raman spectroscopy. Chemical Communications, 2017. **53**(33): p. 4550-4561.

5. Xie, Z., et al., Exceptionally Small Statistical Variations in the Transport Properties of Metal–Molecule–Metal Junctions Composed of 80 Oligophenylene Dithiol Molecules. Journal of the American Chemical Society, 2017. **139**(16): p. 5696-5699.

6. Ma, T., et al., Modulating and probing the dynamic intermolecular interactions in plasmonic molecule-pair junctions. Physical Chemistry Chemical Physics, 2019. **21**(29): p. 15940-15948.

7. Benz, F., et al., SERS of Individual Nanoparticles on a Mirror: Size Does Matter, but so Does Shape. The Journal of Physical Chemistry Letters, 2016. **7**(12): p. 2264-2269.

8. Benz, F., et al., Nanooptics of Molecular-Shunted Plasmonic Nanojunctions. Nano Letters, 2015. **15**(1): p. 669-674.

CHAPTER 3 MONITORING THE DYNAMIC PROCESS OF FORMATION OF PLASMONIC MOLECULAR JUNCTIONS DURING SINGLE NANOPARTICLE COLLISION

3.1 Introduction

The dynamic collision events of individual nanoparticles (NPs) at an ultrasmall electrode (ultramicroelectrode (UME) or nanoelectrode (NE)) have been extensively studied by electrochemical methods.[1-4] This is motivated by the fundamental research in nanoscale electrochemistry,[5] and applications in NP analysis, catalysis, and chemical/biological sensing.[3, 6-8] In one type of single NP collision experiments, a thin layer of an insulator is coated on the UME to suppress direct electron transfer from redox molecules in the electrolyte to the UME. The adsorbed metallic NP after the collision has been discovered to facilitate electron tunneling through the ultra-thin insulating layer.[9, 10] When a self-assembled monolayer (SAM) is used as the insulating layer,[11] plasmonic molecular junctions with well-defined gap distance can be constructed, without using precisely manipulated nanoprobes[12] or advanced nanofabrication techniques.[13] Previous work has demonstrated that the terminal groups of SAM strongly affect the NP collision behavior and the junction formation.[14] However, the molecule level understanding of the chemical interaction and junction formation, which is of remarkable interest to molecular electronics and molecular plasmonics [13, 15] remain elusive.

In chapter 3, we formed plasmonic molecular junctions through the random collision events of gold NPs (AuNPs) in the electrolyte with a gold nanoelectrode (AuNE) modified with a SAM (Figures 3-1A-C). The collision formed AuNP-on-AuNE geometry

is analogous to the widely used "NP-on-Mirror" (NPoM) geometry,[16] in which extremely high Raman signal enhancement and single-molecule sensitivity have been achieved due to the gap surface plasmon mode.[16, 17] However, the adsorption of NP to a flat electrode often happens very fast, and it is difficult to capture the detailed dynamic changes during the formation of molecular junctions in NPoM geometry. In contrast, in the new AuNP-on-AuNE configuration, the adsorbed AuNPs are thermodynamically less unstable at the AuNE apex with large surface curvature. Only one or a few AuNPs can stay stable at the AuNE apex. Therefore, the dynamic formation of molecular junctions in the AuNP-on-AuNE configuration can be monitored at the single NP level for a relatively long time with low background noise. Moreover, different from NPoM approach, continuous electron transport through the formed molecular junctions can be easily monitored at the single NP level in the AuNP-on-AuNE configuration. As shown in Figure 3-1A, the electrons continuously flow through this AuNP-on-AuNE geometry under a bias with the presence of redox molecules. The total current is determined by three sequential steps (i)-(iii).[18-20] The landed AuNP serves as a small electron reservoir, which is continuously charged up by acquiring electrons from the oxidation of redox molecules at the AuNP surface, and then as an electron source to provide electrons for the molecular junctions. For the investigated molecules here (Figure 3-1C), tunneling is the dominant electron transport mechanism in step (iii).[11] Therefore, these NP collisions formed dynamic junctions more or less mimic the repeatedly formed transient molecular junctions in scanning tunneling microscopy STM/mechanical break-junction and fixed-junction methods for single-molecule conductance measurements.[21-23] Using time-resolved electrochemical current measurement and surface-enhanced Raman spectroscopy (SERS), we successfully

observed the transient electrochemical current changes. We monitored the evolution of interfacial chemical bonds in the newly formed molecular junctions with 10 s of ms time resolution, during and after the AuNP collision events.

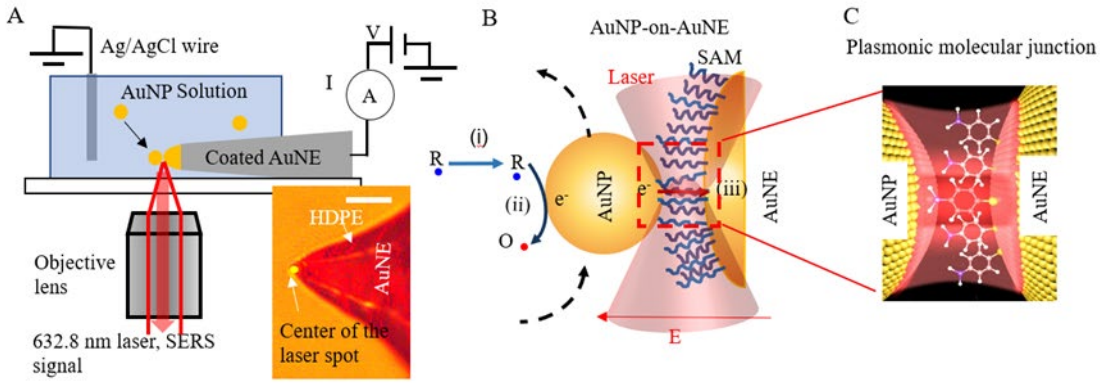

Figure 3-1 Electrochemical current and SERS measurement setup and the AuNP-on-AuNE geometry. (A) The illustration of the setup to perform simultaneous electrochemical current and SERS measurements. The inset at the lower right shows the optical microscope image of an HDPE insulated AuNE irradiated by a laser beam centered at the apex (yellow spot) during the SERS experiment. The scale bar is 5 μm. (B) A schematic representation to show three sequential steps in controlling the current through the AuNP-on-AuNE geometry: (i) mass transport of redox molecules toward the AuNP; (ii) heterogeneous electron transfer from the redox molecules to the AuNP; and (iii) electron transport through the molecular junction. The electric field direction and the laser irradiation are also illustrated. (C) The geometry of the formed plasmonic molecular junctions.

3.2 The Surface Curvature Dependent Distribution of Adsorbed AuNPs at the AuNE Apex

The SAM modification at a AuNE surface serves three important functions: 1) It suppresses direct charge transfer from redox molecules in solution to the AuNE, effectively reducing the background current signal; 2) The terminal groups of the SAM molecules retain AuNPs at the AuNE surface to form molecular tunnel junctions, and their density and binding strength appear to control the number of adsorbed AuNPs; 3) Its thickness (i.e.,

the length of SAM forming molecule) modulates the effect of quantum mechanics in the AuNP/molecule/AuNE plasmonic junctions.

The effects of molecule length and terminal groups of SAM molecules on NP collision events have been investigated.[11, 14, 20, 24] Here, we mainly focused on the effect of the terminal group. We have investigated the AuNP distribution at the molecule modified AuNE apex by using SEM. Due to the charging effect, high-quality SEM images were obtained only on non-insulated AuNEs. Thus, we imaged non-insulated AuNEs after immersed in AuNPs colloid for 20 minutes. Before SEM imaging, these AuNEs were rinsed with DI water and dried by an Argon flow. Figures 3-2A and B show the typical SEM images for bare, and AOT/MHX modified AuNEs. The 4-ATP modified AuNE was shown in Figure 3-3B. Apparently, the distribution of AuNPs on the AuNE apex is non-uniform, which appears to be strongly dependent on the surface curvature. Few AuNPs can be observed at the tip apex, nor any AuNP clusters at the AuNE apex. The density of AuNPs increases with the cross-section radius and decreases with the AuNE surface curvature. For example, for an AOT/MHX modified AuNE, the number of adsorbed AuNP increases obviously with a cross-section radius larger than r1 = 0.5 μm (Figure 3-3B, red dashed line). Note, there are a few AuNP clusters observable at the lower section of the Au Tip. However, this section of the AuNE is coated and protected by HDPE in real experiments. Therefore, only a few AuNPs are able to stay at the AuNE apex. And the formation of AuNP cluster is also suppressed.

We also imaged the insulated AuNEs after collision experiments. Only the AuNEs with a relatively big exposed area can be imaged with acceptable quality because of severe charging. The exposed area of the AuNE in Figure 3-2C is around 3.5 μm^2, while the

typical AuNE exposed area is below 3 μm^2. The AuNPs are indicated by the yellow arrows. The image in Figure 3-2C confirmed 1) only a few AuNPs are adsorbed at the AuNE apex; 2) no AuNP large clusters or aggregations are at the AuNE apex. However, AuNP aggregations or large clusters were indeed observed when the AuNE was exposed to the AuNP solution for a long time (i.e., several hours, see Figure 3-5).

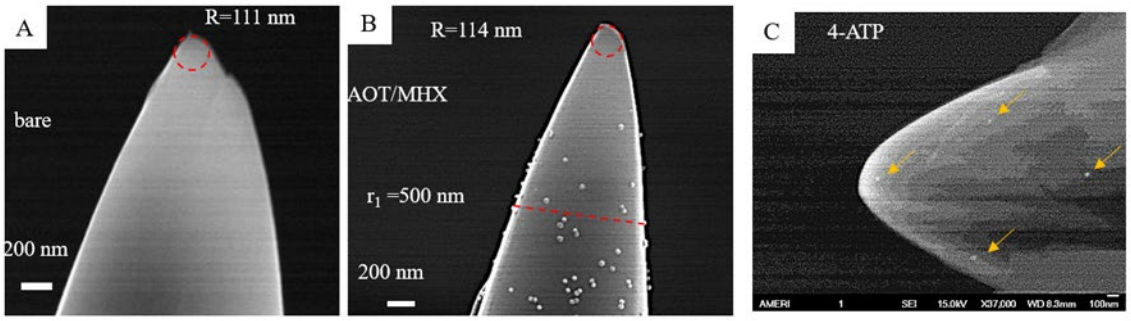

Figure 3-2 (A, B) SEM images for the apex of AuNEs without an insulating coating after immersed in AuNP solution. These AuNEs are bare (A), and modified with AOT/MHX (B). The scale bar for all these images is 200 nm. (C) SEM images for an insulated and 4-ATP modified AuNEs after collision experiments. The yellow arrows indicated the attached AuNPs. The effects of the molecule terminal group to the electrochemical current results

3.3 Surface Chemistry Effects on the Transient Electrochemical Current Changes

The terminal groups of molecules are crucial in forming the molecular junctions, thus defining the characteristics of the current changes seen in the electrochemical measurements. For bare AuNEs without any molecule modifications (trace 1 of Figure 3-3A), no spikes or steps were observed after adding AuNPs in the solution. Neither AuNEs modified with molecules containing a hydroxyl (OH-, i.e., MHX) (trace 2 of Figure 3-3A) nor carboxyl (COOH-, i.e., MHA) terminal groups (trace 3 of Figure 3-3A) can produce detectable current changes as well. In contrast, current changes were observed from the AuNP collisions events at AuNEs modified with amine-terminated SAM. Therefore, we

focus our discussions on two molecules containing an amine (-NH_2) terminal group. One is 4-Aminothiophenol (4-ATP), and the other is 8-amino-1-octanethiol (AOT). (4-ATP and AOT will be discussed in section 3.2.2 and 3.2.3, respectively)

It has been observed before that the current is reduced on the COOH-terminated surface.[14] This was attributed to the electrostatic repulsion and the reduced electron transfer (ET) kinetics at the AuNP surface. The citrate stabilized AuNPs are negatively charged in the experimental electrolyte (zeta potential -103 ± 11 mV). The carboxyl groups of SAM are partially deprotonated and becomes negatively charged at pH 7.4, which repels the AuNP. In contrast, attractive electrostatic force appears between the amine-terminated surface and AuNP. In addition, it is well known that the amine group can form stronger bonding with gold atoms than carboxyl or hydroxyl groups.[25] Through stronger interactions with the AuNP, the amine group can help to retain the AuNP at the AuNE surface and reduce the contact resistance. In contrast, the carboxyl or hydroxyl groups cannot form strong enough bonds with gold, leading to high contact resistance and short residence time of AuNP at the AuNE surface.

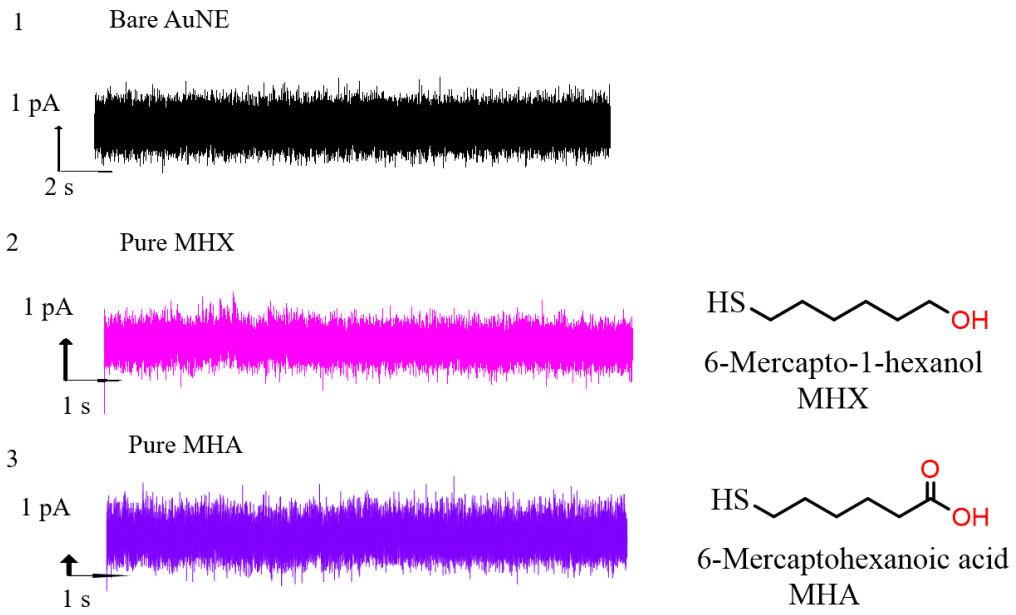

Figure 3-3 Typical featureless *I-t* traces of AuNEs with different molecule modifications with the presence of 40 nm AuNPs in the electrolyte solution. 1. Bare AuNE. 2. AuNE modified with MHX. 3. AuNE modified with MHA. Right column: molecule structures for MHX and MHA.

3.4 Current Changes from -NH_2 Terminal Group Modified AuNEs

3.4.1 Current Changes from 4-ATP Modified AuNEs

Figure 3-4B shows a scanning electron microscopy (SEM) image of a 4-ATP modified AuNE apex after immersed in AuNPs colloid for 20 minutes. To avoid severe charging effects during SEM imaging, this AuNE was not insulated. We simply model the AuNE apex as a cone-shaped tip with a hemispherical cap. The curvature radius R of this tip is about 180 nm, and the typical value is between 100-200 nm. The typical exposed apex area of an insulated AuNE is about 1-3 μm^2 used in this chapter. A SAM with well-packed molecules is formed on the AuNE. The red dashline near cross-section radius 750 nm marks the typical boundary of the insulating HDPE layer, which ensures that only a few AuNP-on-AuNE geometries are in the laser beam.

Figure 3-4C shows the typical *I-t* traces in electrochemical current measurements using 4-ATP modified AuNEs. Before adding AuNPs in solution, the baseline current is stable (see trace (i) of Figure 3-4C). The baseline current is faradic current from the oxidation of $Fe(CN)_6^{4-}$ ions, and a stable baseline current suggests a stable SAM with the absence of contaminations. Upon adding of AuNPs into the solution, current steps and spikes appear. The current steps are typically interpreted as the AuNP 'hit-n-stay' collision events,[26] and are only occasionally observed in our experiments (see one example in Figure 3-4C). This implies that only a few AuNPs can be chemically adsorbed to the AuNE apex stably, consistent with the SEM images (see Figure 3-4B). Current spikes are the dominant signals in the AuNE collision measurements. These transiently enhanced electrochemical current changes are typically interpreted as the AuNP "hit-n-run" collision events. Interestingly, we are able to identify two types of current spikes in our experiment. Type I spike usually appears immediately after adding AuNPs in the solution and tends to be isolated from each other (see trace (ii) of Figure 3-4C). Transient fast-decaying charging current often appears in type I spikes. The magnitude of these type I spikes is typically lower than 6 pA. In contrast, the type II spike often appears at a later time of the experiments, with higher magnitude and longer duration time than that of type I spike (see trace (iii)). They often occur in a cluster form, with more fluctuations in magnitude and sometimes appearing as telegraph noise (see Figure 3-5). These changes cannot be explained by AuNP motion alone, and molecular changes are likely involved as well.

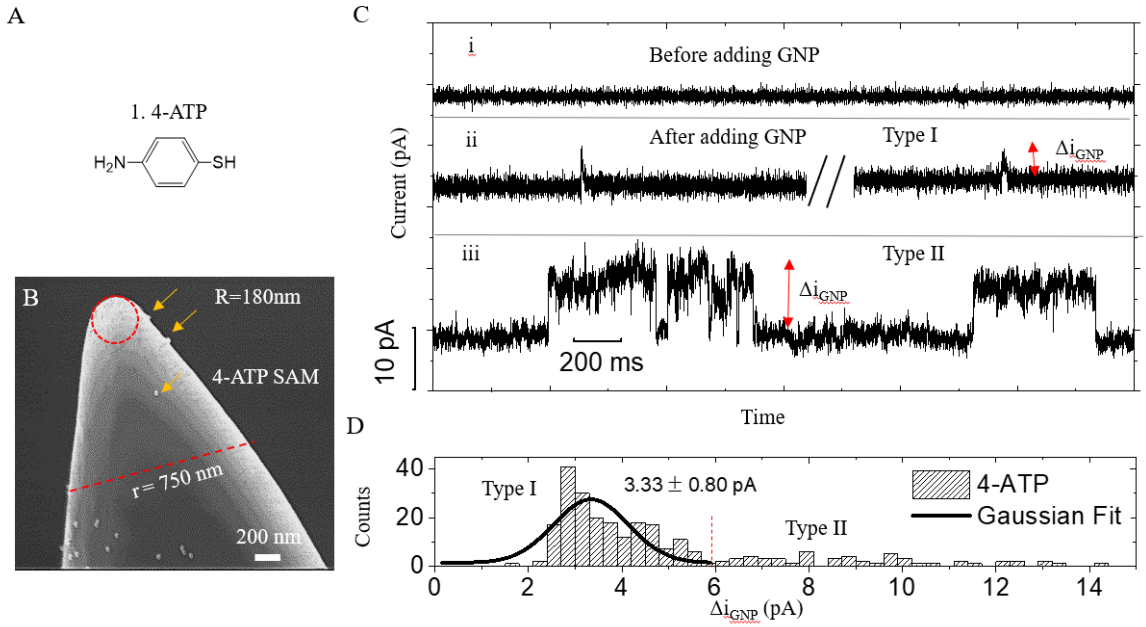

Figure 3-4 AuNPs collision on 4-ATP modified AuNE. (A) Molecular structure of 4-ATP. (B) SEM image of 4-ATP modified AuNE, which is not insulated, after immersed in 150 pM AuNPs colloidal for 20 minutes. (C) Current spikes in electrochemical current measurement. (a) Typical current-time traces for 4-ATP modified AuNEs. (i) before adding AuNPs. (ii) typical type I current spikes. (iii) typical type II current spikes. (D) The histogram of current spike height, which is built from 300 events. The solid line is the Gaussian fit. All the curves were collected at 600 mV in 5 mM PBS with pH=7.4. The redox mediator ($Fe(CN)_6^{4-}$) concentration was 3 mM.

We further analyzed the magnitude of several hundred current spikes statistically. Both the cluster of spikes and the switching events are treated as one event and only counted once. A typical histogram of the spike height is shown in Figure 3-4D. The histogram shows a major peak, with the mean peak value at 3.3 ± 0.8 pA, and a broad distribution above 6 pA. Obviously, the former is from type I spikes, and the latter is from type II spikes. To understand the current spike height, we go back to the three-step electron transfer/transport model depicted in Figure 3-1B. The current change (or spike height) should not be limited by the mass transport of redox species to the AuNP surface in step (i). Because the amine group terminated SAM surface is positively charged at pH 7.4, the

mass transport of redox molecules to the AuNP surface should be enhanced due to the attractive electrostatic force, which is different from the COOH-terminated SAM surface (see Figure 3-3).

The *I-t* trace in Figure 3-5A shows rich type II current change signal, which was likely from an unstable junction formed after a AuNP collision event that producing strong but unstable amine-gold bonds at the AuNP-molecule interface. Due to the unstable molecule-gold contacts of this AuNP on the AuNE surface, both fluctuations and two-level switching are observed in the current trace. The current oscillations near the end of the trace is reminiscent of the SERS signal oscillations observed in Figure 3-9B.

We have discussed earlier that the geometry of AuNE helped to suppress the aggregation of AuNPs at the AuNE surface. However, if the AuNEs exposed to AuNPs for a long time (typically after 1-2 hours), aggregation with a few AuNPs still cannot be avoided. When this happens, cluster of spikes with large amplitude (>37 pA) appeared (Figure 3-5B). The SEM image revealed the presence of AuNP aggregates/clusters at the AuNE surface after long time experiments (Figure 3-5), suggesting that the aggregates/clusters are the most likely origin for these large amplitude signals. The measurements reported typically finished in 20 minutes.

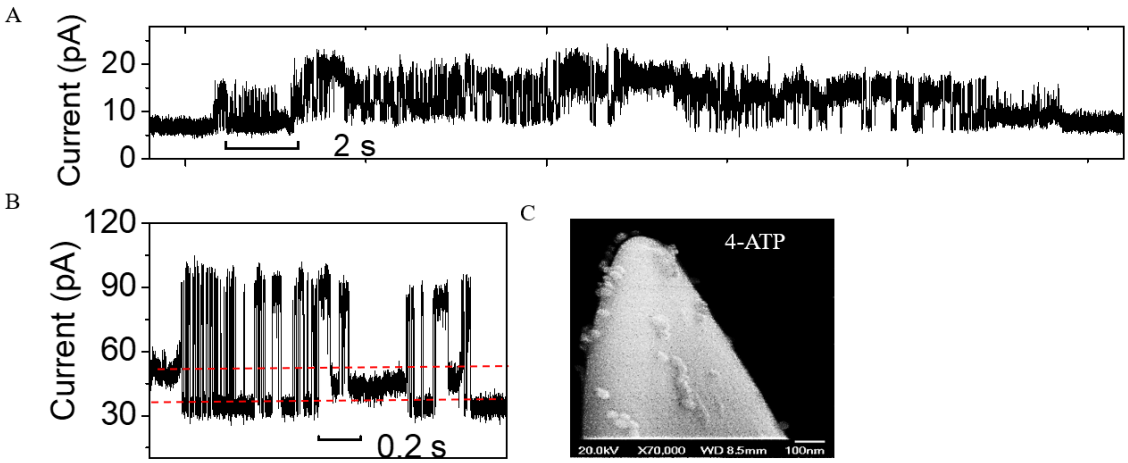

Figure 3-5 (A) A *I-t* trace showing an unstable AuNP-molecule-AuNE junction with continuous type II changes. (B) A *I-t* trace showing large magnitude curernt spikes (>20 pA) after long time (>1 hour) measurements with AuNPs in the solution. The height difference between two red dash lines is typical for a single AuNP caused current changes. Both traces are from 4-ATP modified AuNEs. (C) A SEM image to show the AuNP aggregations at a 4-ATP modified insulated AuNE after long time collision experiments.

3.4.2 Current Changes from AOT/MHX Modified AuNEs

We observed similar current changes, including current steps and spikes, at the AOT/MHX (Figure 3-6A) modified AuNEs. Figure 3-6B shows several current steps that appeared immediately after adding AuNPs in the solution. A few current steps are often observed right after adding AuNPs in the solution. In contrast to the results from AuMEs, the variation of the step height is small, and the value is similar to that of current spikes. This implies that these current steps are due to single AuNP collision events.

Figure 3-6C shows the typical current spikes. A typical histogram of the current spike height (green color) at V = 0.6 V is shown in Figure 3-6D. The mean peak value is 3.5 ± 0.9 pA. The histogram of 4-ATP (the same one in Figure 3-6D) is plotted here for comparison. The results from AOT/MHX modified AuNEs are similar to that from 4-ATP

modified AuNEs. However, spikes with higher magnitudes (>10 pA) are observed more often for 4-ATP modified AuNEs.

The current measurement results indicate that the observed current changes are mainly caused by single AuNP events. This is closely related to the properties of curved AuNEs employed in the experiment. First, the small surface area of AuNE significantly reduces the rate of AuNP collision. Second, the hemispherical shape of the AuNEs suppresses the aggregation of AuNPs at the AuNE. In contrast, large NP aggregations often happen at the edge of the flat microelectrode after collisions,[27, 28] introducing complicated signals arising from clusters of AuNPs. Third, the curvature of AuNE makes the AuNP adsorption difficult. With a reduced number of adsorbed AuNPs at the AuNE, the clean signals from single AuNP collision events can last for a much longer time, comparing to that on a flat AuME.

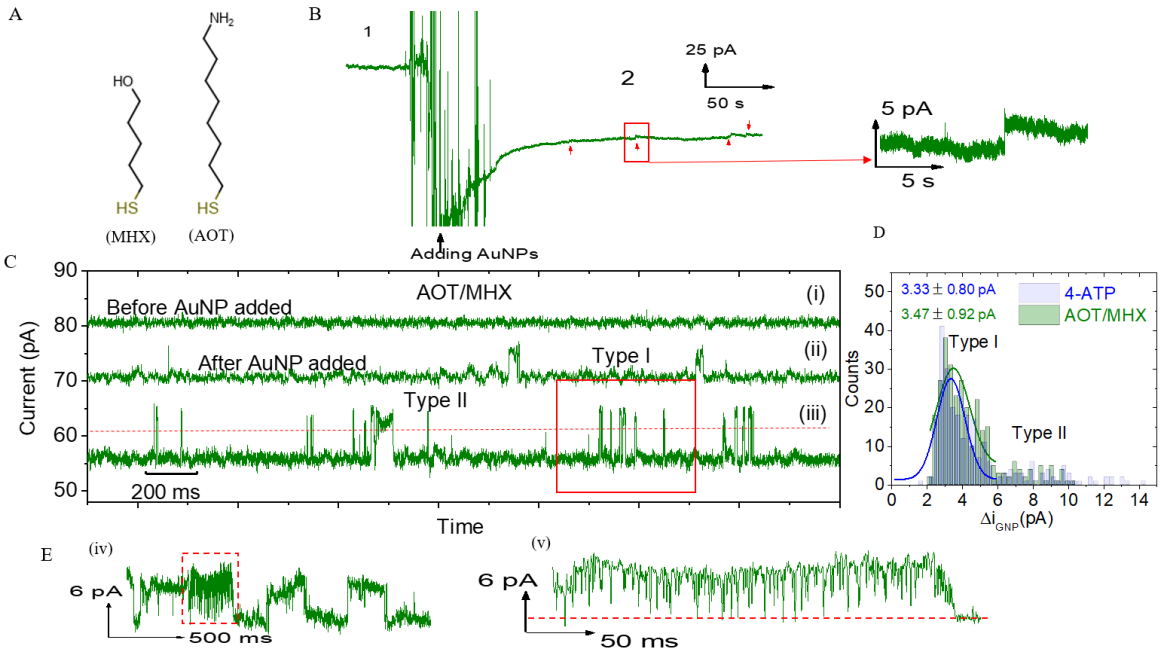

Figure 3-6 Current change signals from AOT/MHX modified AuNEs. (A) Molecular structure of AOT and MHX. (B) A typical *I-t* trace at the beginning of the experiment.

Section 1 of the time trace is before adding AuNPs. The large noise was caused by opening the Faraday cage when adding 40 nm AuNPs (~150 pM in DI water) into the solution. The current reduction is due to the reduction of redox molecule concentration after adding the AuNP solution. Section 2 of the time trace showed multiple current steps, and the red arrows indicated the locations of steps. Zoom in of a current step in the red shaded area is shown in the right. (C) Typical *I-t* traces to show current spikes: (i) before adding AuNPs. (ii) typical type I current spikes. (iii) Typical type II current spikes. The type II spike cluster inside the red rectangular is counted as one spike in statistics. (D) Histogram for the magnitude of current spikes. The histogram of 4-ATP (blue color) is shown here for comparison. (E) A typical *I-t* trace to show a cluster of current spikes (iv) and the fast switching signals in the zoom-in trace (v). These *I-t* traces were measured without SERS measurements. The noise level is smaller.

The estimated diffusion-limited current change is 37 pA, which is larger than the maximum magnitude of type II spike. Here is the estimation: Assuming that the current spike is induced by the transient increase of the diffusion-limited electrochemical current of AuNE (Δi_{AuNP_d}) because of the attachment of a AuNP to the AuNE[2], we estimated the height of the current spike

$$\Delta i_{AuNP\_d} = 4\pi(\ln 2)*F*D*C_R^**R_{AuNP}$$

where R_{AuNP} is the radius of the AuNP (20 nm). Using the concentration (C_R = 3 mM) and diffusion constant (D = 7.6 x10^{-6} cm^2/s) of $Fe(CN)_6^{4-}$ ion, the diffusion-controlled current spike magnitude value Δi_{AuNP_d} is 37 pA.

This is consistent with the observation by Unwin's group.[14] They attributed the smaller current change to the finite intrinsic electron transfer kinetics. Here, the electron transfer kinetics is limited by the electrochemical resistance REC (heterogeneous electron transfer kinetics at the AuNP surface) in step (ii), or/and by the tunneling process through the molecular junctions in step (iii). Since 4-ATP is highly conductive, the tunneling process should be controlled by the contact resistance (electronic coupling) at the molecule-gold interface. Both REC and the contact resistance of molecular junction are

molecule structure independent, which explains the similarity of the histograms for current spike magnitude between 4-ATP and AOT molecules. In the experiment, it is unlikely that the REC at the AuNP surface varies significantly. Therefore, we hypothesize that the current spike height is mainly limited by the contact resistance and, therefore, sensitive to the variations of the interfacial chemical bonds.

3.4.3 Current Changes Results from Gold Microelectrode

For comparison, planar gold microelectrodes (AuME, surface area 200 μm^2) were fabricated and tested (see Figure 3-7A). The planar AuME was fabricated by the standard optical lithography methods in the cleanroom. The molecule modification of AuME can refer to section 2.12. For 4-ATP modification, 2 mM 4-ATP ethanol solution is typically used for 1-2 hours deposition. Immediately after adding AuNPs in the solution, a large number of current steps were observed, and the staircase changes often lasted for 20-30 minutes. As shown in Figure 3-7B trace (i) and (ii), the height of steps is not uniform, suggesting multiple AuNPs can hit-n-stay at the AuME simultaneously. After several minutes, current spikes also appeared. As shown in trace (iii) of Figure 3-7B, a large fraction of current spikes shows a height of current spikes about 20 pA, suggesting type II spikes. The number of type I current spike is much less compared with the results of AuNEs. It is difficult to separate these spikes because they were always clustered together. These results imply that AuNPs are stable on flat AuMEs. Trace (iv) is a typical trace from a 4-ATP modified AuME. Compared with AOT/MHX modified AuMEs, the current spike density is much higher. The current spikes also showed various height levels, similar to the current steps. The multi-level current change is more obvious in the zoom-in trace (v).

These current switching/spikes also show a higher magnitude, suggesting small AuNP aggregations. The SEM image in Figure 3-7C shows a large number of AuNPs on a AuME, including small aggregates with 2 or 3 AuNPs. The image was taken after the collision experiments.

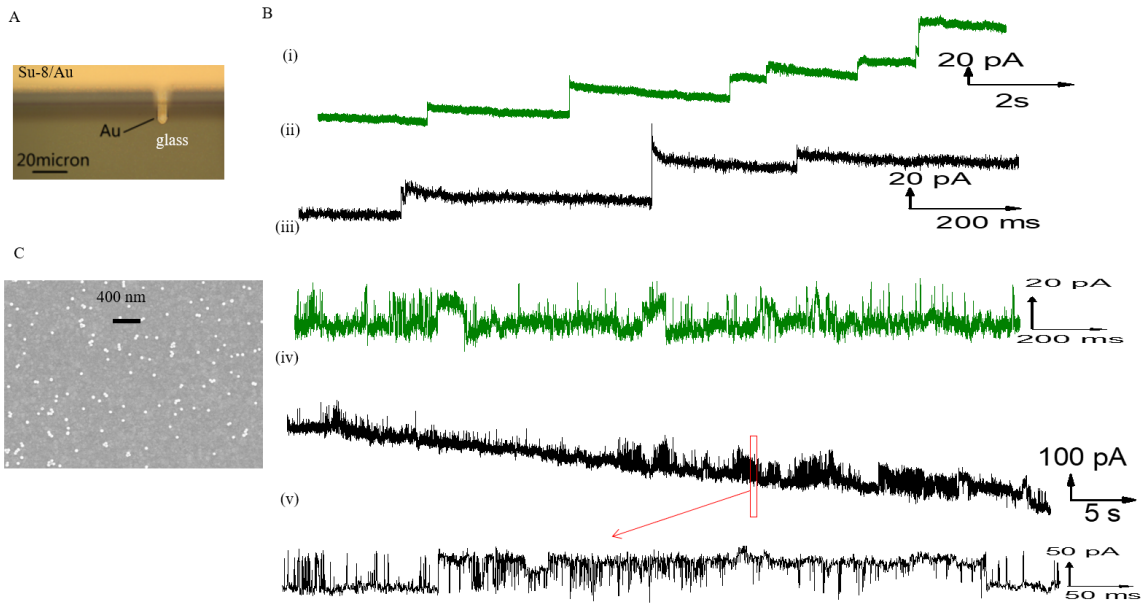

Figure 3-7 (A) An optical microscope image of the AuME. (B) Typical *I-t* traces for AOT/MHX (green) and 4-ATP (black) modified AuMEs right after adding 40 nm size AuNPs in the solution. (C) A SEM image of the AOT/MHX modified AuME after the 40 nm AuNP collision experiments.

3.5 Current Changes from Various Molecules Modified AuNEs

We have tested various molecules with hydroxyl (-OH), carboxyl (-COOH), and amine (-NH_2) terminal groups. No current spikes were observed from AuNEs modified with OH- and COOH- SAM. Therefore, we focus our discussions on two molecules containing amine (-NH_2) terminal group. One is 4-aminothiophenol (4-ATP), and the other is 8-amino-1-octanethiol (AOT). Yellow arrows in Figure 3-4B highlight the locations of a few adsorbed AuNPs at the apex of a 4-ATP modified AuNE. Apparently, the adsorption

of AuNPs is strongly dependent on the curvature of AuNE surface and always there are only a few AuNPs adsorbed at the exposed AuNE apex. The red dashline near cross-section radius 750 nm marks the typical boundary of the insulating high-density polyethylene (HDPE) layer, which ensures that only a few AuNP-on-AuNE geometries are in the laser beam. In contrast, a large number of adsorbed AuNPs were shown uniformly distributed on a planar microelectrode after the collision experiment. The amine groups of 4-ATP or AOT SAM are partially protonated and the SAM is positive in the electrolyte employed in experiment (pH ~7.4).[29] The electrostatic interaction between protonated amine group ($-NH_3^+$) and negatively charged AuNP facilitates the adsorption of AuNPs. Further, chemical interactions happen between amine group and gold. Based on density functional theory (DFT) calculations, the non-protonated amine group can form strong Au-N coordination bond (about 0.5 eV binding energy) with undercoordinated Au atom at the atop site.[30, 31] The amine-gold bond can also be formed in other binding configurations, but with smaller binding energy. The protonated amine group at low pH cannot form a strong bond with gold. Because of the strong and well-defined Au-N coordination bond, the single molecule conductance measurements measured the conductance of 4-ATP and AOT to be about 1 μS and 0.1-1.0 nS, respectively.[23, 30, 32]

3.6 Simultaneous Electrochemical Current and SERS Measurement of Single AuNP Collision Events

To better understand the origin of the two types of current spikes and the molecular changes coupled with the AuNP motion in these collision events, we acquired time-resolved SERS trajectories and *I-t* traces simultaneously. It is widely accepted that two

mechanisms contribute to the enhancement of SERS: the electromagnetic (EM) and chemical enhancement. The former is associated with the surface plasmonic resonances of metal nanostructures[33, 34] and is highly sensitive to the distance change between two metal nanostructures in gap mode. The latter is highly dependent on the electronic resonances at the metal-molecule interfaces, *i.e.*, the charge transfer (CT) between molecule and metal, and thus is sensitive to the chemical bonding at the molecule-metal interface.[35] 4-ATP molecule has been extensively studied in aspect of the chemical enhancement mechanism.[16, 36-39] Moreover, this molecule is able to serve as an effective pathway for quantum tunneling, which has been suggested to affect the SERS spectra.[13]

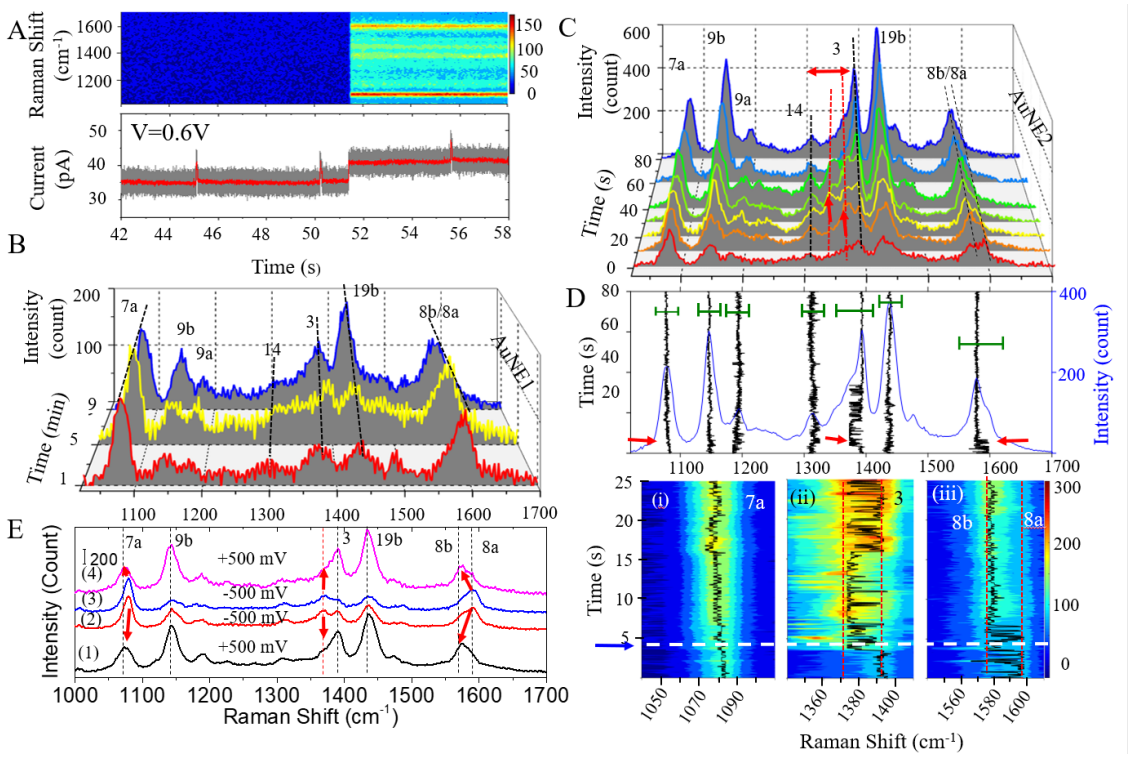

Figure 3-8 The evolution of SERS spectra in newly formed molecular junctions after 'hit-n-stay' collision events. (A) The simultaneously recorded time-resolved SERS trajectory (heat map, 67.3 ms per frame) and *I-t* trace at AuNE1 apex after adding AuNPs in the solution. Color bar shows the intensity of the SERS signal in CCD counts. Grey line shows raw current data with 10 kHz sampling rate, and the red line is smoothed data after applying

a moving average over 15 points. (B) Progressive SERS spectra from AuNE1 showing the evolution of SERS spectra over 9 minutes. Band 8a/8b shows a blue-shift from 1592 cm^{-1} at minute 1 to 1582 cm^{-1} at minute 9. (C) Progressive SERS spectra from AuNE2 showing the evolution of SERS spectra in 80 s after adding AuNPs in the solution. The red arrows indicate the locations of two new transient bands. The applied bias was 0.6 V for (B) and (C). (D) Top: The time traces of spectral peak positions of major vibration modes in spectral windows indicated by the green color scales. The time-averaged SERS spectra are also plotted in blue line for reference. Bottom: Three zoom-in time traces (black lines) of spectral peak position near bands 7a, 3 and 8a/8b at the first 25 s, superposed on the corresponding intensity heat map. (E) Four SERS spectra taken after changing applied bias polarity sequentially from steps 1 to 4.

Figure 3-8A shows a SERS trajectory and the corresponding *I-t* trace recorded from a AuNE1 (A1 = 0.27 μm^2) apex right after adding AuNPs in the solution. In the *I-t* trace, three type I current spikes are shown above a stable baseline, suggesting 'hit-n-run' events. No correlated SERS changes were detected before 51.4 s. These collision events likely occurred outside of the laser spot or were too fast to be detected by the SERS measurement. At 51.4 s, a current step appeared with comparable height as the current spikes. This is a clear sign of a AuNP 'hit-n-stay' event. Coincidentally, SERS signals of 4-ATP molecules appeared promptly and continued to the rest of SERS measurement. Clearly, this demonstrates the origin of 4-ATP SERS signals as arising from the collision formed molecular junctions.

3.6.1 Time Evolution of SERS Spectrum in AuNP 'hit-n-stay' Events

We followed the evolution of the SERS spectrum of AuNE1 over the next several minutes (Figure 3.8B). Here, we focused on the most studied spectral region between 1000 cm^{-1} - 1700 cm^{-1} for 4-ATP. The vibrational bands of 4-ATP in this spectral region have been assigned with a1 (7a, 8a, and 9a), and b2 (9b, 14, 3, 19b, 8b) symmetries (see table 3.1).[39] The initial SERS spectrum is dominated by two strong a1 bands 7a and 8a, due to

the stretching modes of C_{ring}-S and C_{ring}-C_{ring}, respectively. However, the magnitudes of b2 bands (9b, 3, 19b) increase continuously and the magnitudes are more than doubled at minute 9. In contrast, a moderate fluctuation (5-30%) is seen on the magnitudes of 7a over the same time period. Interestingly, we also observed a continuous blue-shift of the 8a band, suggesting a band transition from mode 8a to 8b. The a1 and b2 bands of 4-ATP are well-documented to be governed by EM and CT enhancement mechanisms, respectively. The different intensity changes of the a1 and b2 bands imply different changes occurring to/in the molecular junction. The intensity change of mode 7a can serve as an internal probe to reveal the motion of AuNP near the AuNE surface. The minor changes seen in the 7a band, accompanied with a flat current baseline, exclude any dramatic positional changes of the AuNP after the junction formation at 51.4 s. The selective enhancement of b2 bands and the band transition from 8a to 8b are interpreted as enhanced CT between gold and 4-ATP molecules. The CT enhancement is dependent on the electronic coupling strength at the molecule-gold contact, which can be characterized by the intensity ratio of b2/a1 bands. Therefore, we utilized the changes of intensity ratio b2/a1 (i.e., I_{9b}/I_{7a}) to probe the changes of interfacial chemical bonding. Considering the orientation of the 4-ATP molecule in the SAM at the AuNE surface, amine-gold bond accounts for the most probable and dynamic interfacial chemical bonding in our system. In Figure 3-8B, the intensity ratio of I_{9b}/I_{7a} is steadily increased from 0.39 to 0.55, suggesting continuously improved electronic coupling of the amine-gold interaction during the residence of the AuNP on the AuNE1. However, the 9b band did not reach the height of the 7a band even at minute 9, indicating the amine-gold bonds are still weak in the hotspot.

Table 3-1 4-ATP SERS vibration mode assignment. a) Cited from ref.[40] b) The notations of the modes are ν, stretch, and δ , bend, respectively. c) Follow assignments ref.[40]

SERS in GNP-on-GNE Geometry	Normal Raman [a)]	Assignments [b)]	Mode (Symmetry)[c)]
1079	1089	νCS	7a (a1)
1148		δCH	9b (b2)
	1173	δCH	9a (a1)
1188		δCH	9a (a1)
1313		νCC + δCH	14 (b2)
1386		δCH + νCC	3 (b2)
1439		νCC + δCH	19b (b2)
	1490	νCC + δCH	19 a (a1)
1578		νCC	8b (b2)
1590	1595	νCC	8a (a1)

Figure 3-8C shows a similar but faster evolution of SERS spectra recorded from AuNE2, which has a larger exposed surface area with a smaller average surface curvature (A2 = 3.4 μm^2). The initial spectrum is dominated by 7a band. However, in just 80 seconds, the baseline spectrum is stabilized and the main b2 bands (9b, 3, 19b) are all much higher than the 7a band with the ratio of I_{9b}/I_{7a} = 1.7, suggesting the faster transition to strong amine-gold bonds in the hotspot. In addition to the significant intensity increase of b2 bands, we observed detailed spectral changes in the first 40 seconds, which are clearly shown in the time traces of spectral peak position (black color) in Figure 3-8D, which were obtained by tracking the peak position of major bands in a small spectral range (indicated by the green color scales). The lower panel of Figure 3-8D shows the zoom-in of three traces (black color), which are also superposed on the intensity heat map. In the first 5 s, band 7a was blue shifted. Because mode 7a is the C_{ring}-S stretching mode, the shift in 7a suggests the molecule was affected all the way to the bottom contact.[41] Coincidentally, fast switching appeared between bands 8a and 8b. After 5s, the band 8a was fully shifted to 8b

and fast switching between 8a and 8b stopped. Following the changes in 7a and 8a, the band of mode 3 near 1392 cm^{-1} jumped to 1370 cm^{-1} and fast switching appeared between 1370 cm^{-1} and 1392 cm^{-1}. Sometimes, additional new vibration mode appeared as shoulder peak near 1332 cm^{-1} (indicated by red arrows in Figure 3-8C). The new bands near 1370 and 1332 cm^{-1} do not appear immediately when the amine-gold bond is weak, typically right after the landing of a AuNP. Neither are these bands noticeable when the amine-gold bond is strong, typically when the AuNP is stabilized on the AuNE (*i.e.*, at 80 s in Figure 3-8C). However, the intensity of the 1370 cm^{-1} band is transiently comparable, or even higher than that of the neighboring mode 3 band during the early stabilization stage of the landed AuNP, *e.g.*, 20~40 s in Figures 3-8C and D. The appearance of these transient peaks likely implies the development of intermediate amine-gold bonding geometries in the dynamic molecular junctions formed by collision events.

Interestingly, the new bands have been observed previously when a gold coated atomic force microscopy (AFM) tip made direct top contacts to 4-ATP molecules self-assembled at a gold substrate.[36] The force applied by the AFM tip could deform the 4-ATP molecule structure, leading to the formation of new Au-N bonding configurations. Such a scenario can also be realized in the AuNP-on-AuNE geometry through altering the applied bias at the AuNE. When a large positive (or negative) bias is applied at the AuNE, the adsorbed negatively charged AuNP is expected to be slightly displaced by the electrical force.[42, 43] The molecular junction underneath the AuNP can be mechanically compressed or stretched. The amine-gold bond at the top interface, as well as the associated CT process, is likely to be affected the most. As shown in Figure 3.8E, we altered the applied bias on the AuNE between +0.5 V and -0.5 V and monitored the spectral changes. When changing

the applied bias from -0.5 V to + 0.5 V (from spectrum 3 to 4, or from spectrum 2 to 1), we found remarkable similarities in the spectral changes compared with those observed in AuNP "hit-n-stay" events: (1) the selective intensity increase of b2 bands compared with a1 bands; (2) the notable new band near 1370 cm^{-1} at – 0.5 V becomes indistinguishable at + 0.5 V; (3) the band of 7a is slightly blue-shifted; (4) the band of 8a is blue-shifted and converted to band 8b. The dramatic changes happen at b2 bands suggest the strong Au-N bond developed at + 0.5 V was weakened with deformed binding geometry at - 0.5V. The SERS spectrum is also fully recovered at the end after applying +0.5 V to the AuNE ((4) of Figure 3-8E). This reversibility clearly rules out the possibility of permanent detachment of the adsorbed AuNP from the AuNE surface during the bias cycle, as well as, any concern of non-reversible chemical reactions. With the new insight from the bias experiments, we are able to interpret the dynamic changes that happened in the newly formed plasmonic molecular junction during AuNP "hit-n-stay' event. The collision and the following stay of the AuNP, often slightly deform the molecules underneath. The interactions at the SAM-AuNP interface normally begins with weak amine-gold interactions. With the conformational changes of molecule, intermediate Au-N bonding geometries often appear. Eventually, strong Au-N bonds with undercoordinated Au atoms at the atop sites at the AuNP surface can be developed, greatly improving charge transfer between molecule and gold. This strong Au-N bonds developed in AuNP/4-ATP/AuNE junction can also be weakened by bias or pH.

3.6.2 SERS Spectral Changes in AuNP 'hit-n-run' Collision Event

SERS spectral changes in Figure 3.8 revealed the dynamic changes that happened in the newly formed junctions after the 'hit-n-stay' events. Same as the observations in electrochemical current changes, there are more 'hit-n-run' events induced transient intensity and spectral changes in the SERS trajectory. A large number of these SERS transient changes only show major changes at 7a and 8a, but modest or no changes at b2 bands. The $\Delta I_{9b}/\Delta I_{7a}$ change ratio is much less than 1. Figure 3-9A panel (i) shows an example, using a difference SERS trajectory after subtracting a constant baseline spectra. The corresponding *I-t* trace in panel (ii) shows a type I current spike. It is interesting to note that the duration of current spike is shorter than the 'on' time for the SERS signal. In addition, the rise and fall for the current spike are much faster than that of the Raman signal. The changes of a1 bands between 9.5 and 10.5 s are not accompanied by current changes. This is likely induced by a AuNP collision event with weak or no amine-gold bond formation during the collision. The approaching of a AuNP to the AuNE surface is expected to first enhance the intensity of a1 bands, resulting from the EM enhancement mechanism. If no amine-gold bonds are formed, b2 bands will not be enhanced before the departure of the AuNP. Correspondingly, no current changes can be detected. If weak amine-gold bonds are formed, type I current spike will appear. Because of the large curvature of the AuNE, a AuNP 'hit-n-run' event often cannot immediately produce reliable electrical contacts at the molecule-AuNP interface. This is why we observed a large number of type I spikes instead of type II spikes, as shown in Figure 3-8.

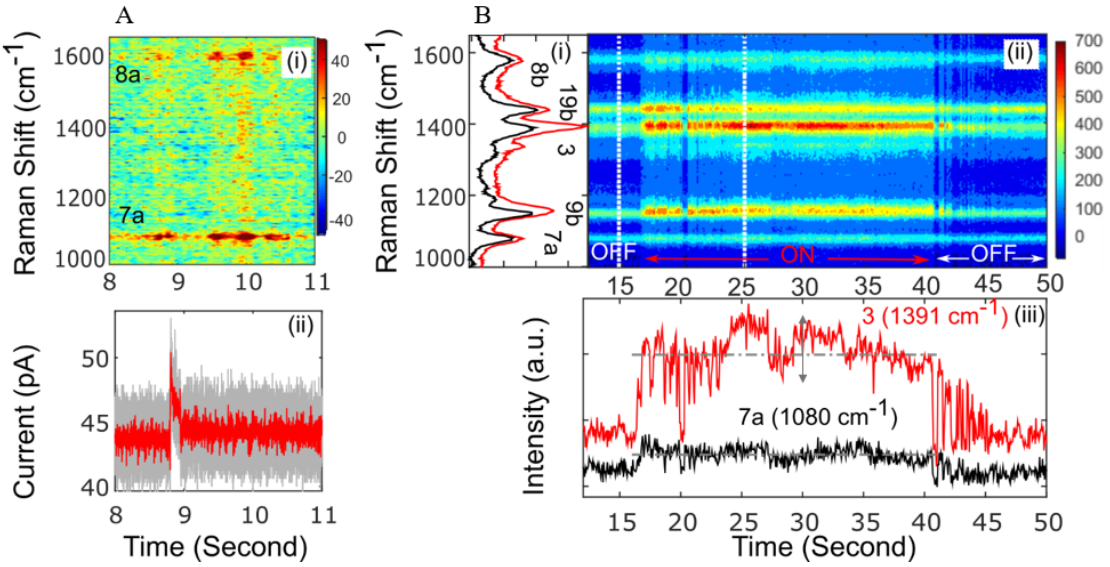

Figure 3-9 Transient SERS and current changes induced by AuNP 'hit-n-run' collision events. (A) (i) The difference SERS trajectory (67.3 ms time resolution) constructed by subtracting background SERS (at 6.0 s) from the entire trajectory. (ii) The simultaneously recorded *I-t* trace (V = 0.6 V). Grey lines show raw data with a 10 kHz sampling rate, and red lines represent data after applying a moving average over 15 points. (B) (i) SERS spectrum in 'on' (red curve) and 'off' (black curve) states, sliced from the SERS trajectory (shown in (ii)) at two dashed white lines marked positions in 'on' and 'off' region, respectively. We assign 'on' and 'off' states in the SERS trajectory based on the intensity variation of 7a band. At 'on' state, the increased signal intensity and spectral shift indicate the stay of the AuNP at the AuNE surface. (ii) The SERS trajectory. (iii) Intensity-time trace of vibrational modes 3 (red) and 7a (black), respectively. Gray dash-dot lines show the average SERS intensities of these two bands at an 'on' state (17 ~ 40 s). The two traces are offset for clarity. The measurements were carried out in solution with the presence of AuNPs (30 pM).

Similar to type II current spikes, only a small fraction of SERS transient changes showed distinct changes in both a1 and b2 bands (see Figure 3-9B). Individual 'snapshot' SERS spectrum at 'off' (black color) and 'on' state (red color), respectively, are shown in (i) on the left of a SERS trajectory (ii). Time traces for modes 3 (b2) and 7a (a1) are shown in (iii). The amplitude increase from 'off' to 'on' state for mode 3 is about three times higher than that of mode 7a. If the prompt intensity jump of mode 7a at 17 s signals the landing of a AuNP, the simultaneous and drastic intensity increase in mode 3 trace suggests

the prompt formation of strong amine-gold bonds. The most striking feature in the trajectory is the oscillations in both a1 and b2 bands at the beginning and the ending of the 'on' state. They are attributed to the back-and-forth movement of the AuNP and the fast breaking and reformation of the amine-gold bonds. These oscillation features have never been observed when the changes of b2 bands are small. Obviously, the strong interfacial amine-gold bonds alter the AuNP motion in a 'hit-n-run' collision event. Larger intensity fluctuation is often seen in the mode 3 trace than in the mode 7a trace in the middle of the 'on' state, *e.g.* during 22 ~ 35 s of (ii) and (iii). In addition, the fluctuation is also significantly enhanced at 'on' state than at the 'off' state. These fluctuations should originate from molecule fluctuations, and lead to frequent current fluctuations in type II spikes.

Mode-specific spectral and temporal fluctuations, and discrete changes in time-resolved SERS trajectories are intriguing. In line with argument for single molecule SERS,[32] it would be difficult to synchronize a large number of molecules to generate discrete intensity/spectral fluctuation and mode specific frequency changes. The fast switching between two vibration modes also strongly suggest single molecule level behaviors. Therefore, we conclude that the significant fluctuations in the CT active SERS bands are likely induced by only one or a few molecules in the plasmonic molecular junctions. Tunneling current fluctuations/switching are also ubiquitous in similar size STM tip formed molecular junctions at room temperature, revealed by various single molecule conductance measurements.[22, 44-46] Very recently, it has been reported that single gold atom positional change in the plasmonic molecular junctions of the NPoM configuration can lead to the transient formation of a "picocavity", which leads to a high SERS

enhancement and makes single molecule changes observable in the SERS trajectories.[47] Nanoscale surface curvature also plays important roles to promote such variations.[48] Therefore, it is reasonable that single molecule fluctuations can be observed in these highly dynamic AuNP/molecule/AuNE junctions involving tens to hundreds molecules.

3.7 Conclusion

In summary, we have shown that the AuNP collisions at a SAM modified AuNE enable the construction of plasmonic molecular junctions. Compared with flat microelectrodes, the large curvature of AuNE renders the AuNP thermodynamically unstable, limiting the number of adsorbed AuNPs at the AuNE apex to a few and slowing down the process of formation of strong interfacial chemical bonds between AuNP and the SAM. We have successfully monitored the dynamic formation of new junctions, which are initiated by a AuNP collision event and followed by the development of interfacial chemical bonds between the landed AuNP and the SAM molecules at the AuNE. Transient intermediate states of the interfacial amine-gold bond are revealed. We believe the reported results will shed light on the molecule conformational and inter- and intra- chemical bonding changes in the transiently formed tunnel junctions in solution by STM/mechanical break-junction and fixed-junction methods. By changing the shape, size, materials and surface chemistry of both NE and NP, this method can become a versatile platform to study various chemical interactions in molecular junctions. The new AuNP-on-AuNE geometry and the simultaneous SERS/electrochemical measurements also have a great potential to be utilized in the study of single-molecule chemical reaction confined in a nanocavity or nanoreactor[49] and the interplay between molecular electronics and plasmonics.[13, 15]

3.8 Experimental Section

Chemical Modification of the AuNE. The details of electrochemical etching, insulation and characterization of AUNE can be found in Supporting Information and elsewhere.[50] The quality of SAM is critical to achieve reproducible signal. Parameters such as molecule concentration and deposition time were optimized to produce a high-quality SAM at the curved AuNE surface. 50 mM molecule concentration was used and the deposition time varied from 7 hours to overnight, in order to achieve a saturated 4-ATP SAM at the AuNE apex. We noted that the deposition concentration of 4-ATP was much higher than the one used for the modification of a planar electrode.

Electrochemical Current Measurement. The *I-t* measurement setup (Figure 3.1A) was placed in a suspended Faraday cage on an optical table to reduce electrical noise and mechanical vibrations. An Axon 200B patch clamp amplifier (Molecular Devices Inc., CA) in voltage clamp mode was used to supply the bias and amplify the current. A 10 kHz Bessel low-pass filter was typically used for current measurements. An Axon Digidata 1440A (Molecular Devices Inc., CA) was used to record data at 50 kHz. The setup has the sensitivity to detect a current change less than 1 pA with a temporal resolution better than 1 ms. The AuNE was used as the working electrode. The Ag/AgCl electrode was grounded and used as the *quasi* reference electrode. The *I-t* traces were typically recorded at +0.6 V in 5 mM PBS (pH=7.4) with the presence of 3 mM Potassium Ferrocyanide as redox mediator. The applied bias value was chosen such that the electrochemical current reached the saturation value limited by the mass transport of redox mediators. The concentration of citrate stabilized 40 nm AuNP in the solution varied and a typical concentration was 30 pM. The color of the solution in the liquid cell was uniform immediately after AuNP

injection. No AuNPs aggregation or precipitation was observed during experiments. All the measurements were performed at room temperature.

SERS Measurement. SERS was performed on a home-built Raman microscopy setup. The laser beam was focused at the AuNE apex that was fixed in a liquid cell installed on a Nikon microscope sample stage. The time-resolved SERS trajectories were collected with a time resolution of 67.3 ms (if not mentioned otherwise). Spectral resolution was about 2 cm^{-1}. The power of 632.8 nm excitation laser was attenuated by ND filters to 0.5 mW. The laser spot size was about 3 μm and the typical area intensity was about 0.17 $mW/\mu m^2$. Signals from HDPE in the 1000-1700 cm^{-1} spectral region were ignored because they were at least an order of magnitude smaller than that of 4-ATP.

Simultaneous Electrochemical current and SERS Measurements. A small faraday cage was used to shield the liquid cell on the sample stage of Nikon microscope. The synchronization of optical and electrical measurements was achieved by sending an external trigger signal (generated by a Labview program) to both CCD camera and Axon Digidata 1440A. It should be noted that the electrical noise of simultaneous measurements was about 3-5 times higher than that of separate electrochemical current measurement. This is not induced by laser irradiation because the on/off of laser dose not impact the current noise level. The increased noise is attributed to the less effective electrical shielding by the small faraday cage on the microscope stage. We reduced the sampling rate to 10 kHz and a moving average filter was used in data analysis.

Data Analysis. The data were analyzed by home-built Labview (National Instruments) and Matlab (MathWorks Inc.) programs. The current spikes were detected by a threshold event detection method.[51, 52] We normally used the mean value of points at the top of current

spike for the spike height. Current spikes with charging current contribution were not used in the histogram.

3.9 Reference

1. Quinn, B.M., P.G. van 't Ho, and S.G. Lemay, Time-Resolved Electrochemical Detection of Discrete Adsorption Events. Journal of the American Chemical Society, 2004. **126**(27): p. 8360-8361.

2. Xiao, X., et al., Current Transients in Single Nanoparticle Collision Events. Journal of the American Chemical Society, 2008. **130**(49): p. 16669-16677.

3. Dick, J.E., C. Renault, and A.J. Bard, Observation of Single Protein and DNA Macromolecule Col-lisions on Ultramicroelectrodes. Journal of the American Chemical Society, 2015.

4. Robinson, D.A., et al., Collision Dynamics during the Electrooxidation of Individual Silver Nanoparticles. Journal of the American Chemical Society, 2017. **139**(46): p. 16923-16931.

5. Oja, S.M., et al., Nanoscale Electrochemistry Revisited. Analytical Chemistry, 2016. **88**(1): p. 414-430.

6. Castañeda, A.D., et al., Electrocatalytic Amplification of Nanoparticle Collisions at Electrodes Modified with Polyelectrolyte Multilayer Films. Langmuir, 2015. **31**(2): p. 876-885.

7. Dick, J.E., et al., Electrochemical detection of a single cytomegalovirus at an ultramicroelectrode and its antibody anchoring. Proc Natl Acad Sci U S A, 2015. **112**(17): p. 5303-8.

8. Li, D., et al., Real-time electrochemical monitoring of covalent bond formation in solution via nanoparticle-electrode collisions. Chemical Communications, 2015. **51**(91): p. 16349-16352.

9. Zhao, J., et al., Nanoparticle-mediated electron transfer across ultrathin self-assembled films. J Phys Chem B, 2005. **109**(48): p. 22985-94.

10. Shein, J.B., et al., Formation of Efficient Electron Transfer Pathways by Adsorbing Gold Nanoparticles to Self-Assembled Monolayer Modified Electrodes. Langmuir, 2009. **25**(18): p. 11121-11128.

11. Xiao, X.Y., et al., Single Nanoparticle Electrocatalysis: Effect of Monolayers on Particle and Electrode on Electron Transfer. Journal of Physical Chemistry C, 2009. **113**(33): p. 14978-14982.

12. Cui, X.D., et al., Reproducible Measurement of Single-Molecule Conductivity. Science, 2001. **294**(5542): p. 571-574.

13. Zhu, W., et al., Quantum mechanical effects in plasmonic structures with subnanometre gaps. Nature Communications, 2016. **7**: p. 11495.

14. Chen, C.-H., et al., Impact of Surface Chemistry on Nanoparticle–Electrode Interactions in the Electrochemical Detection of Nanoparticle Collisions. Langmuir, 2015. **31**(43): p. 11932-11942.

15. Wilson, A.J. and K.A. Willets, Molecular Plasmonics. Annu Rev Anal Chem (Palo Alto Calif), 2016. **9**(1): p. 27-43.

16. Park, W.-H. and Z.H. Kim, Charge Transfer Enhancement in the SERS of a Single Molecule. Nano Letters, 2010. **10**(10): p. 4040-4048.

17. Sigle, D.O., et al., Observing Single Molecules Complexing with Cucurbit[7]uril through Nanogap Surface-Enhanced Raman Spectroscopy. J Phys Chem Lett, 2016. **7**(4): p. 704-10.

18. Chazalviel, J.-N. and P. Allongue, On the Origin of the Efficient Nanoparticle Mediated Electron Transfer across a Self-Assembled Monolayer. Journal of the American Chemical Society, 2011. **133**(4): p. 762-764.

19. Hill, C.M., J. Kim, and A.J. Bard, Electrochemistry at a Metal Nanoparticle on a Tunneling Film: A Steady-State Model of Current Densities at a Tunneling Ultramicroelectrode. Journal of the American Chemical Society, 2015. **137**(35): p. 11321-11326.

20. Kim, J., et al., Tunneling Ultramicroelectrode: Nanoelectrodes and Nanoparticle Collisions. Journal of the American Chemical Society, 2014. **136**(23): p. 8173-8176.

21. Xu, B. and N.J. Tao, Measurement of Single-Molecule Resistance by Repeated Formation of Molecular Junctions. Science, 2003. **301**(5637): p. 1221-1223.

22. Haiss, W., et al., Measurement of single molecule conductivity using the spontaneous formation of molecular wires. Physical Chemistry Chemical Physics, 2004. **6**(17): p. 4330-4337.

23. Reed, M.A., et al., Conductance of a Molecular Junction. Science, 1997. **278**(5336): p. 252-254.

24. Krause, K.J., et al., Influence of Self-Assembled Alkanethiol Monolayers on Stochastic Amperometric On-Chip Detection of Silver Nanoparticles. Analytical Chemistry, 2016. **88**(7): p. 3632-3637.

25. Chen, F., et al., Effect of Anchoring Groups on Single-Molecule Conductance: Comparative Study of Thiol-, Amine-, and Carboxylic-Acid-Terminated Molecules. Journal of the American Chemical Society, 2006. **128**(49): p. 15874-15881.

26. Wang, W. and N. Tao, Detection, Counting, and Imaging of Single Nanoparticles. Analytical Chemistry, 2014. **86**(1): p. 2-14.

27. Boika, A., S.N. Thorgaard, and A.J. Bard, Monitoring the Electrophoretic Migration and Adsorption of Single Insulating Nanoparticles at Ultramicroelectrodes. The Journal of Physical Chemistry B, 2013. **117**(16): p. 4371-4380.

28. Fosdick, S.E., et al., Correlated Electrochemical and Optical Tracking of Discrete Collision Events. Journal of the American Chemical Society, 2013. **135**(16): p. 5994-5997.

29. Bryant, M.A. and R.M. Crooks, Determination of surface pKa values of surface-confined molecules derivatized with pH-sensitive pendant groups. Langmuir, 1993. **9**(2): p. 385-387.

30. Venkataraman, L., et al., Single-Molecule Circuits with Well-Defined Molecular Conductance. Nano Letters, 2006. **6**(3): p. 458-462.

31. Quek, S.Y., et al., Amine−Gold Linked Single-Molecule Circuits: Experiment and Theory. Nano Letters, 2007. **7**(11): p. 3477-3482.

32. Zrimsek, A.B., et al., Single-Molecule Chemistry with Surface- and Tip-Enhanced Raman Spectroscopy. Chemical Reviews, 2017. **117**(11): p. 7583-7613.

33. Ciracì, C., et al., Probing the Ultimate Limits of Plasmonic Enhancement. Science, 2012. **337**(6098): p. 1072-1074.

34. Aravind, P.K., R.W. Rendell, and H. Metiu, A new geometry for field enhancement in surface-enhanced spectroscopy. Chemical Physics Letters, 1982. **85**(4): p. 396-403.

35. Campion, A. and P. Kambhampati, Surface-enhanced Raman scattering. Chemical Society Reviews, 1998. **27**(4): p. 241-250.

36. Uetsuki, K., et al., Experimental Identification of Chemical Effects in Surface Enhanced Raman Scattering of 4-Aminothiophenol†. Journal of Physical Chemistry C, 2010. **114**(16): p. 7515-7520.

37. Zhou, Q., et al., Charge Transfer between Metal Nanoparticles Interconnected with a Functionalized Molecule Probed by Surface-Enhanced Raman Spectroscopy. Angewandte Chemie International Edition, 2006. **45**(24): p. 3970-3973.

38. Fromm, D.P., et al., Exploring the chemical enhancement for surface-enhanced Raman scattering with Au bowtie nanoantennas. The Journal of Chemical Physics, 2006. **124**(6): p. 061101.

39. Osawa, M., et al., Charge transfer resonance Raman process in surface-enhanced Raman scattering from p-aminothiophenol adsorbed on silver: Herzberg-Teller contribution. Journal of Physical Chemistry, 1994. **98**(48): p. 12702-12707.

40. Osawa, M., et al., Charge transfer resonance Raman process in surface-enhanced Raman scattering from p-aminothiophenol adsorbed on silver: Herzberg-Teller contribution. The Journal of Physical Chemistry, 1994. **98**(48): p. 12702-12707.

41. Xu, B., X. Xiao, and N.J. Tao, Measurements of Single-Molecule Electromechanical Properties. Journal of the American Chemical Society, 2003. **125**(52): p. 16164-16165.

42. Shan, X., et al., Detection of Charges and Molecules with Self-Assembled Nano-Oscillators. Nano Letters, 2014. **14**(7): p. 4151-4157.

43. Niroui, F., et al., Tunneling Nanoelectromechanical Switches Based on Compressible Molecular Thin Films. ACS Nano, 2015. **9**(8): p. 7886-7894.

44. Donhauser, Z.J., et al., Conductance Switching in Single Molecules Through Conformational Changes. Science, 2001. **292**(5525): p. 2303.

45. Ramachandran, G.K., et al., A Bond-Fluctuation Mechanism for Stochastic Switching in Wired Molecules. Science, 2003. **300**(5624): p. 1413-1416.

46. Chang, S., et al., Tunnel Conductance of Watson-Crick Nucleoside-Base Pairs from Telegraph Noise. Nanotechnology, 2009. **20**(18): p. 185102-185102.

47. Benz, F., et al., Single-molecule optomechanics in “picocavities”. Science, 2016. **354**(6313): p. 726-729.

48. Villarreal, E., et al., Nanoscale Surface Curvature Effects on Ligand–Nanoparticle Interactions: A Plasmon-Enhanced Spectroscopic Study of Thiolated Ligand Adsorption, Desorption, and Exchange on Gold Nanoparticles. Nano Letters, 2017.

49. Choi, H.-K., et al., Metal-Catalyzed Chemical Reaction of Single Molecules Directly Probed by Vibrational Spectroscopy. Journal of the American Chemical Society, 2016. **138**(13): p. 4673-4684.

50. Tuchband, M., et al., Insulated gold scanning tunneling microscopy probes for recognition tunneling in an aqueous environment. Review of Scientific Instruments, 2012. **83**(1): p. 015102.

51. Plesa, C. and C. Dekker, Data analysis methods for solid-state nanopores. Nanotechnology, 2015. **26**(8): p. 084003.

52. Chang, S., et al., Electronic Signatures of all Four DNA Nucleosides in a Tunneling Gap. Nano Letters, 2010. **10**(3): p. 1070-1075.

CHAPTER 4 EFFECTIVE ELECTROCHEMICAL MODULATION OF SERS INTENSITY ASSISTED BY CORE-SHELL NANOPARTICLESs

4.1 Introduction

Metal adatoms and adparticles (small clusters) at submonolayer coverage are believed to have electronic properties that can deviate significantly from those of the bulk material. Such variations in electronic properties have been studied extensively in terms of their fundamental aspects as well as in their application to catalytic systems. In addition, the adsorption and deposition of metal atoms on foreign metal substrates represents a very attractive family of systems for study because the strong adatom/substrate bonding can control the growth behavior and the resulting structures, especially as a function of surface coverage. Particularly attractive is the study of such systems by electrochemical techniques. especially within the context of underpotential deposition (UPD).

The advent of in-situ techniques eliminated much of the uncertainties involved and, as a result, generated a great deal of interest, and the techniques offered the opportunity of characterizing these systems under active electrochemical control. Of particular importance were the application of spectroscopic techniques such as FT-IR, Raman, and second harmonic generation (SHG). The development of in- situ structural techniques based on either X-ray based methods (such as grazing incidence X-ray scattering, surface SEXAFS, and X-ray standing waves, among others) or scanned probe microcopies (STM, AFM, and related methods) further enhanced the ability to examine surfaces and surface structure at unprecedented levels of detail.

In this review we examine the underpotential deposition of metal mono- and multilayers on singlecrystal electrode surfaces.

4.2 Results and Discussions

4.2.1 The Formation of Au@Ag NPoNE Structure

The exposed apex area of the partially insulated AuNE is in the range of 30-80 μm^2. A monolayer of biphenyl-4-thiol (BPT) was self-assembled on the AuNE apex. Figure 4-1A shows the typical SEM image of a AuNE tip after immersion in solution with 40 nm AuNPs. The average number density of the adsorbed AuNPs on the exposed AuNE apex is about 11 /um^2 (see 4.2.2). The typical laser spot focused on the AuNE apex can cover up to ~50 AuNPs. Nanocavities are formed in these Au NPoNE structures, as shown in Figure 4-1B. Using the setup illustrated in Figure 4-1C, Ag was deposited on the surface of the adsorbed AuNPs on the AuNE apex. The deposition was carried out by the chronoamperometry method at a reduction potential of -0.2 V with 10 μM $AgNO_3$, in the electrolyte.[1] The amount of deposited Ag was controlled by the deposition time, which varied from 20-600 s. Figure 4-1D shows the time-resolved changes of simultaneously acquired reduction current (top panel, red color trace) and SERS signal in heatmap (bottom panel) during the Ag deposition. While the reduction current magnitude increases slightly, the SERS intensity increases significantly with the deposition time. The rapid increase of SERS intensity is also demonstrated in Figure 4-1E, showing four SERS spectra at different time sampled from the SERS trajectory in Figure 4-1D. All spectra show three major peaks of BPT (see 4.2.3, peak assignment of BPT), confirming the formation of NPoNE structures.

Figure 4-1F shows the SEM image of a AuNE apex after 30 min of Ag deposition. The size of Au@Ag NPs is much bigger than the initial 40 nm size of AuNPs. It should be noted that the 30 min deposition time is much longer than the actual time we used for SERS measurements, which is only used here to visualize the Ag deposition by SEM. It is clear that the silver deposition mainly happens on the adsorbed AuNPs. It has been well-studied that metal NP-mediated electron transfer across an insulating thin film, including SAM, is highly effective.[2] Therefore, the adsorbed AuNPs can serve as the nucleation sites for Ag deposition. The BPT SAM prevents random silver deposition and facilitates the *in situ* fabrication of Au@Ag core-shell NPs on the AuNE apex, leading to the formation of Au@Ag NPoNE structures and the enhancement of SERS intensity.

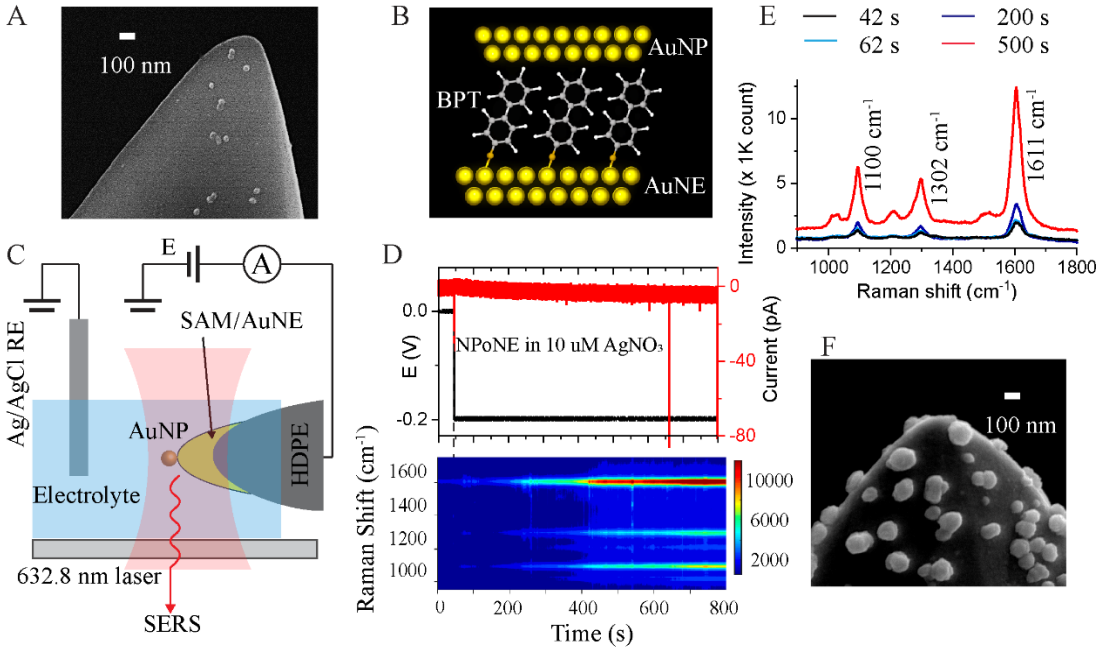

Figure 4-1 The fabrication of Au@Ag NPoNE structures. (A) Scanning electron microscopy (SEM) image of BPT modified AuNE apex with adsorbed AuNPs. To improve the SEM image quality, the AuNE was not insulated. (B) The plasmonic BPT molecular junctions in the Au NPoNE structure. (C) The scheme of experimental setup for the EC-SERS measurements. The AuNE is partially insulated by high-density polyethylene

(HDPE). Electrode potential E was applied to the working electrode AuNE, and the Ag/AgCl wire electrode was the quasi reference electrode (RE). (D) Top panel: chronoamperogram of Ag deposition. The applied electrode potential (solid black line) and acquired electrochemical current (solid red line) are plotted. Bottom panel: the corresponding SERS intensity heatmap. (E) Selected SERS spectra from the heatmap before Ag deposition at t = 42 s and after Ag deposition at t = 62, 200, and 500 s. (F) SEM image of a AuNE apex with Au@Ag NPs after 30 min of Ag deposition.

4.2.2 AuNPs Number Density on the Exposed Area of AuNE

To improve the quality of the SEM image, the imaged AuNE was not insulated. Figure 4-2 shows one typical SEM image of BPT modified AuNE apex with adsorbed AuNPs. The surface area is ~ 13 μm^2, and the total number of AuNPs attached is 143. Thus, the AuNPs number density is around 11/μm^2. The average number is 330-880 for 30-80 μm^2 AuNE. Please note that all those AuNPs will contribute to the electrochemical signal, but the SERS signal only comes from the AuNPs on the apex of AuNE where the incident laser focus on. The laser spot size is ~ 3 μm, so the maximum AuNPs in the laser spot is ~ 50.

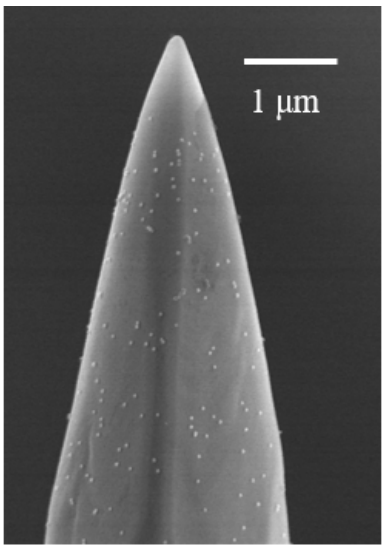

Figure 4-2 SEM image of AuNPs attached to the AuNE.

4.2.3 BPT Raman Peaks Assignment

We assigned the Raman bands based on the literature and density functional theory (DFT) calculation. We have used DFT (Gaussian 09 package) to calculate the Raman spectra of BPT and 4-MBA molecule on gold. The peaks assignment of 4-MBA also can find from our previous study.[3] The gold NP was represented by a Au3 cluster. The DFT calculation was conducted based on the energy minimized ground-state geometry using hybrid exchange–correlation functional (B3LYP). The 6-31G** basis set was used for molecule, and LANL2DZ basis set was used for gold atoms. As shown in Figure 4-3A, the calculated and measured SERS spectra (Figure 4-3B) of BPT matched very well. The mode assignments to the SERS spectrum of BPT based on reference[4, 5] and the DFT calculation are summarized in the table of Figure 4-3C.

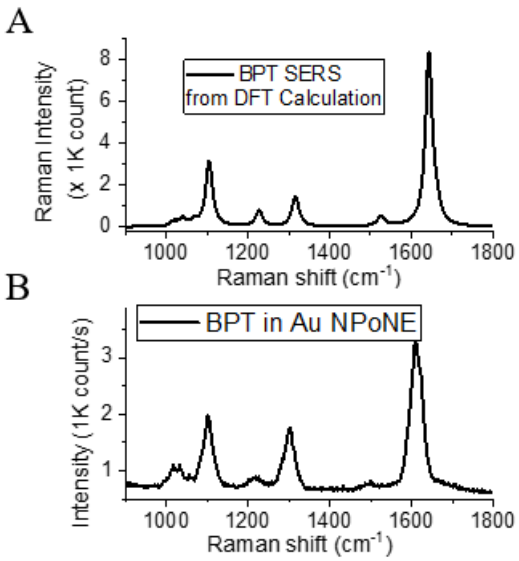

C

BPT	
Assignment	SERS (cm^{-1})
vCS + CC stretch (a1)	1100
HC=CH Dihedral scissor	1220
C-C stretch + C-S-Ag/Au	1300
HC=CH rocking	1500
Ring stretch (a1)	1611

Figure 4-3 (A) The SERS spectrum of BPT from DFT calculation. (B) BPT molecule in the nanocavity of Au NPoNE. (C) The table of SERS bands assignment for BPT.

4.2.4 The Reversibility of SERS Intensity Modulation by Potential

To evaluate the potential modulation of SERS intensity and the reversibility of the system, we performed double potential step chronoamperometry on the fabricated Au@Ag NPoNE structures in 1xPBS electrolyte. The silver atom was oxidized to silver ion (Ag^+) at the positive potential step, and the Ag^+ ion was reduced back to Ag at the negative potential step. In a representative current time trace ((i) of Figure 4-4A), a current spike appears at the beginning of each square wave, which is due to the charging current. Following the charging current peak, faraday current due to Ag redox reaction is gradually stabilized. The magnitude of the faraday current is bigger when the step potential magnitude is increased from 0.2 to 0.4 V, indicating more Ag atoms are involved in the redox process at the higher potential. Figure 4-4A (ii) shows the corresponding SERS trajectory. The SERS intensity of BPT molecule was clearly modulated even at 0.2 V, suggesting the potential modulation is highly effective. The potential modulation is also highly reversible at both potential magnitudes.

The reversibility of the SERS intensity modulation depends on the thickness of the Ag shell. Based on the SERS intensity ratio ($I^{-0.4}/I^{0.4}$) and the reversibility, the performance of the prepared Au@Ag NPoNE structures can be divided into three categories, which clearly associated with the silver deposition time. Here, $I^{-0.4}/I^{0.4}$ is defined as the Raman intensity ratio of BPT at E = -0.4 V and 0.4 V. Figure 4-4B shows the typical SERS spectra pair of all three types. Type I structures are normally obtained when $\Delta t < 30$ s. For this type, the $I^{-0.4}/I^{0.4}$ is close to 1. The short deposition time leads to a thin and incomplete shell, resulting in negligible intensity change. Type II structures are obtained when Δt is between 30 s and 200 s. The intensity modulation ratio is between 1 and 2 and the modulation is

highly reversible. The example in Figure 4-4A belongs to this category. Type III structures are obtained when $\Delta t > 200$ s. For this type, the intensity modulation ratio is bigger than 2, although the reversibility is compromised (see heatmap in 4.2.5). This type of structure will be very useful in applications that reversibility is not important.

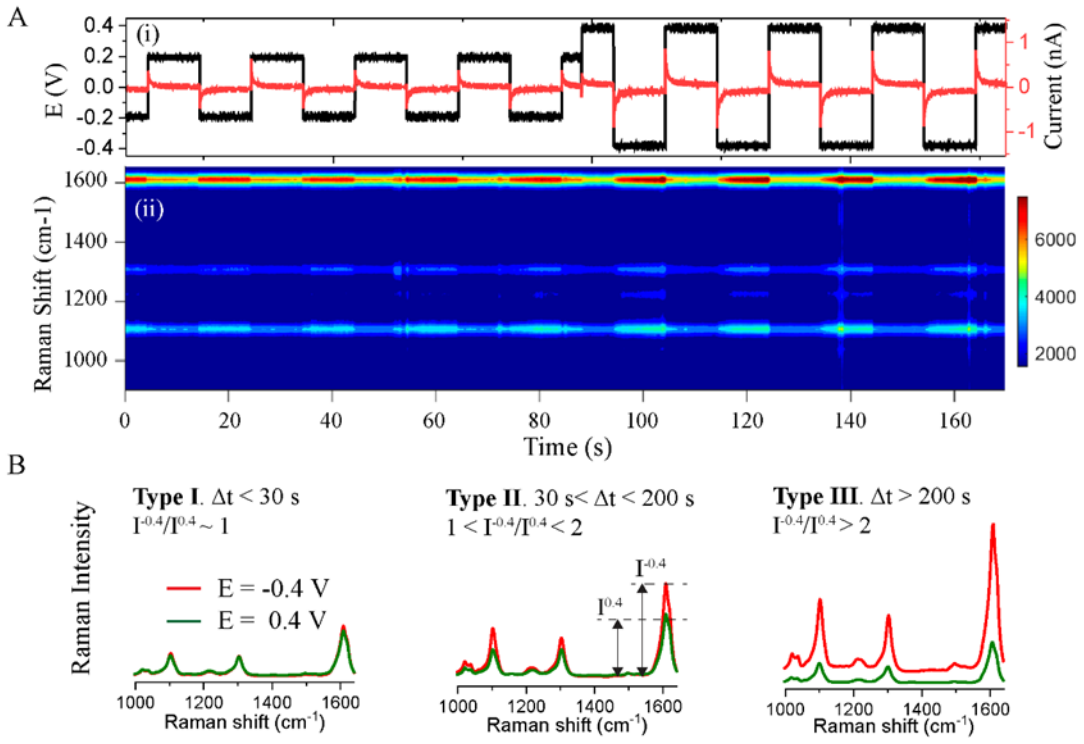

Figure 4-4 The SERS intensity tuning at different Ag deposition time (Δt). (A) Top panel: the double potential step chronoamperogram shows the applied potential waveform (black line) on Au@Ag NPoNE and recorded EC current (red line) in 1xPBS. The period of the square potential waveform is 20 s. Bottom panel: The corresponding SERS intensity heatmap of BPT. (B) The typical Raman spectra of BPT in three types of nanocavities of Au@Ag NPoNE structures at E = -0.4 V (red line) and 0.4 V (olive line).

4.2.5 Type III SERS Intensity Modulation

To evaluate the reversibility of SERS intensity modulation by potential change for fabricated type III Au@Ag NPoNE (600 s Ag deposition), we performed potential step chronoamperometry

(Figure 4-5A) on the it in 1xPBS electrolyte. Figure 4-5B shows the corresponding SERS heatmap of BPT in the nanocavities of type III Au@Ag NPoNE. Figure 4-5C shows the time traces of the three main peaks intensity of BPT under potential modulation. Obviously, the intensity of the second -0.4 V is much lower than the first -0.4 V. Figure 4-5D shows two selected time in Figure S3 to plot the Raman spectra. The value of $I^{-0.4}/I^{0.4} = 3.4$ also indicate it belongs to the type III SERS modulation. However, square potential modulation results show that the reversibility of type III SERS modulation is bad. By normalizing Raman spectra to I_{1100}, we found all the peaks modulated proportionally. A similar phenomenon was observed for the 4-MBA molecule, as shown in Figure 4-6. The only difference is the selective band enhancement due to the charge transfer effect, as discussed in the main text.

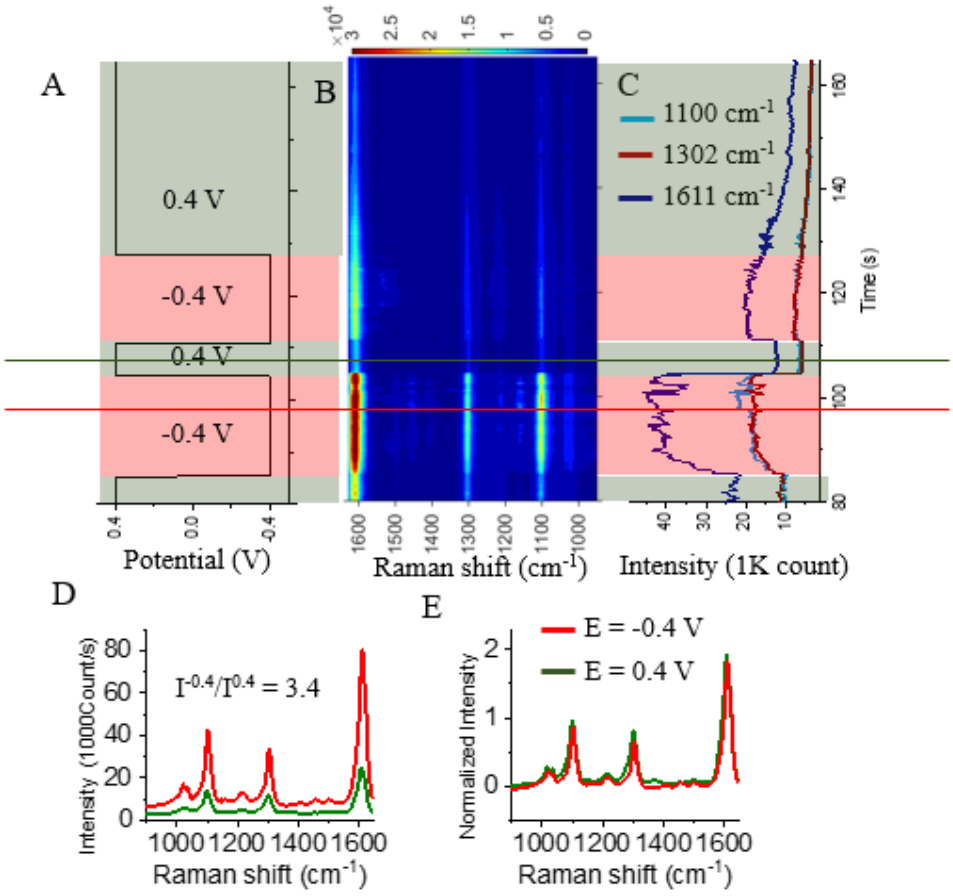

Figure 4-5 Type III modulation of BPT in the nanocavities of Au@Ag NPoNE. (A) Potential E applied to AuNE. (B) Raman intensity heatmap of BPT with potential modulation. (C) Three main peaks time traces of BPT. (D) Selected SERS spectra, as indicated as a red line and olive line from the heatmap. (E) Normalized SERS spectra.

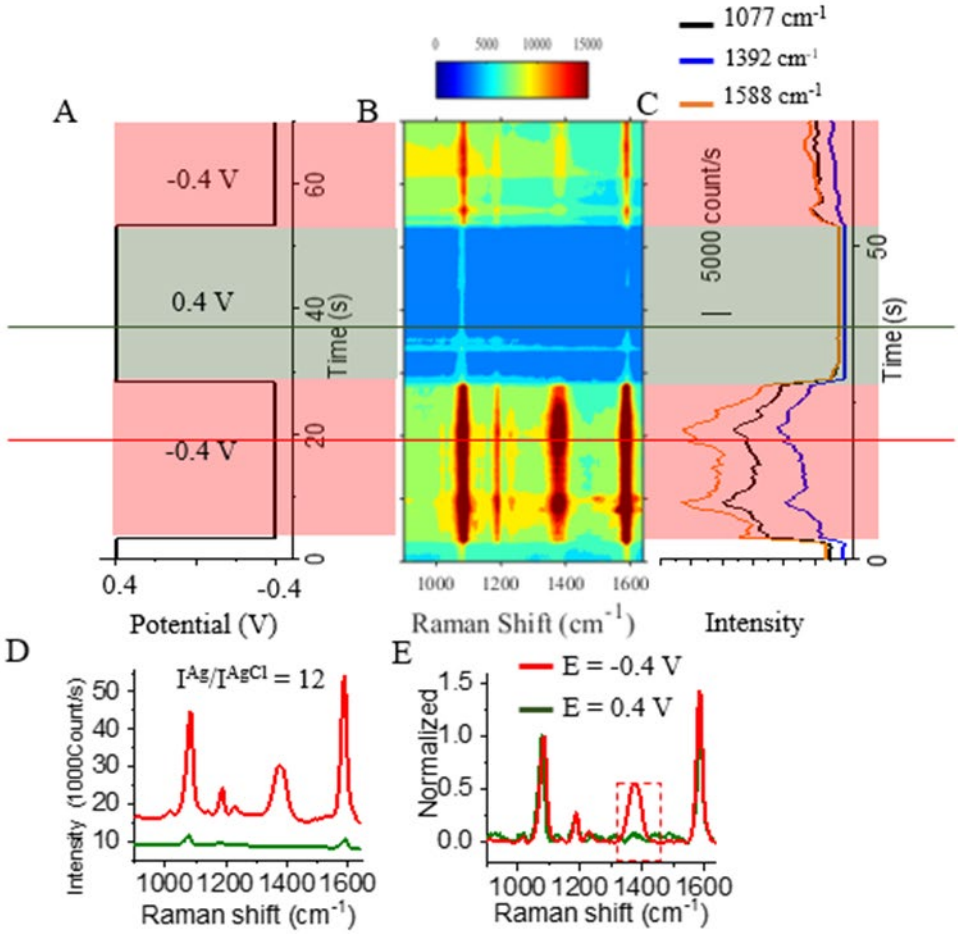

Figure 4-6 Type III modulation of 4-MBA in the nanocavities of Au@Ag NPoNE. (A) Potential E applied to AuNE. (B) Raman intensity heatmap of 4-MBA with potential modulation. (C) Three main peaks time traces of 4-MBA. (D) Selected SERS spectra, as indicated as a red line and olive line from the heatmap. (E) Normalized SERS spectra.

4.2.6 The Mechanism of Silver Assisted Large Modulation of SERS Intensity by Electrode Potential.

We further investigated the mechanism of silver assisted potential modulation of SERS intensity. To understand the redox reaction of the shell, CV and SERS measurements

were conducted simultaneously. As shown in Figure 4-7A, the electrode potential was swept between -1 and 0.4 V in 1x PBS solution. The EC current-time (*i-t*) traces (white color) are superposed on the SERS intensity heatmaps in Figures 4-7B and C. Interestingly, stochastic current spikes are observed in the *i-t* trace of Figure 4-7C. The corresponding CVs of AuNPs without (black curve) and with (red curve) Ag shells are shown in Figures 4-7D and E, respectively. Figures 4-7F and G show the corresponding intensity changes of three main Raman peaks of BPT as a function of E. As shown in Figure 4-7F, the SERS intensity of all three peaks only increased slightly at the negative potential beyond -0.4 V. In the negative potential region, the possible Faradaic process is the hydrogen evolution reaction (HER). The correlation coefficient of current magnitude and Raman intensity is 0.86, indicating a strong correlation between HER and Raman enhancement. A similar phenomenon was observed in previous research.[6, 7] The pH-dependent experiment, as shown in 4.2.7, further confirms the correlation between HER and the observed Raman intensity enhancement.

The CV in Figure 4-7E of Au@Ag NPOPE structures shows new oxidation peaks at E_1= 0.07 V and reduction peaks at E_2 = -0.05 V. From the oxidation potential, this pair of redox peaks are from the redox reaction of Ag/AgCl on the surface of adsorbed AuNPs.[20] The oxidation potential to form Ag_2O is much higher at about 0.4 V.[8, 9] In addition, we also did control experiments by replacing the chlorine ions in the solution with nitrite ion. Instead, no oxidation peaks were observed at the same potential range (see 4.2.8). The small oxidation and reduction peaks are expanded at the right side of Figure 4-7E. It is clear that the redox peaks are composed by a series of stochastic spikes (also see Figure 4-7C). For comparision, the redox peaks from bulk silver wire electrode are rather smooth.

The stochastic nature of Ag/AgCl redox peaks suggests only a small number of silver atoms are involved in the redox process of Ag coated AuNE. Figure 3G shows the significant Raman intensity jump near the Ag/AgCl redox potential of all three bands. Therefore, the effective SERS modulation is attributed to the reversible redox process $Ag + Cl^- \leftrightarrow AgCl + e^-$ happened at the Ag shell of Au@Ag NPoNE. To avoid HER, a potential range between -0.4 and 0.4 V was used in most of our experiments. In this potential range, the SERS intensity modulation is mainly induced by the chlorination and dechlorination of the Ag shell. The level of modulation can be defined by the value of $I^{-0.4}/I^{0.4}$ (or I^{Ag}/I^{AgCl}) for Au NPoNE or Au@Ag NPoNE. For example, $I^{-0.4}/I^{0.4}$ of vibrational mode at 1100 cm^{-1} is only 1.09 for Au NPoNE but increases to 1.78 for Au@Ag NPoNE.

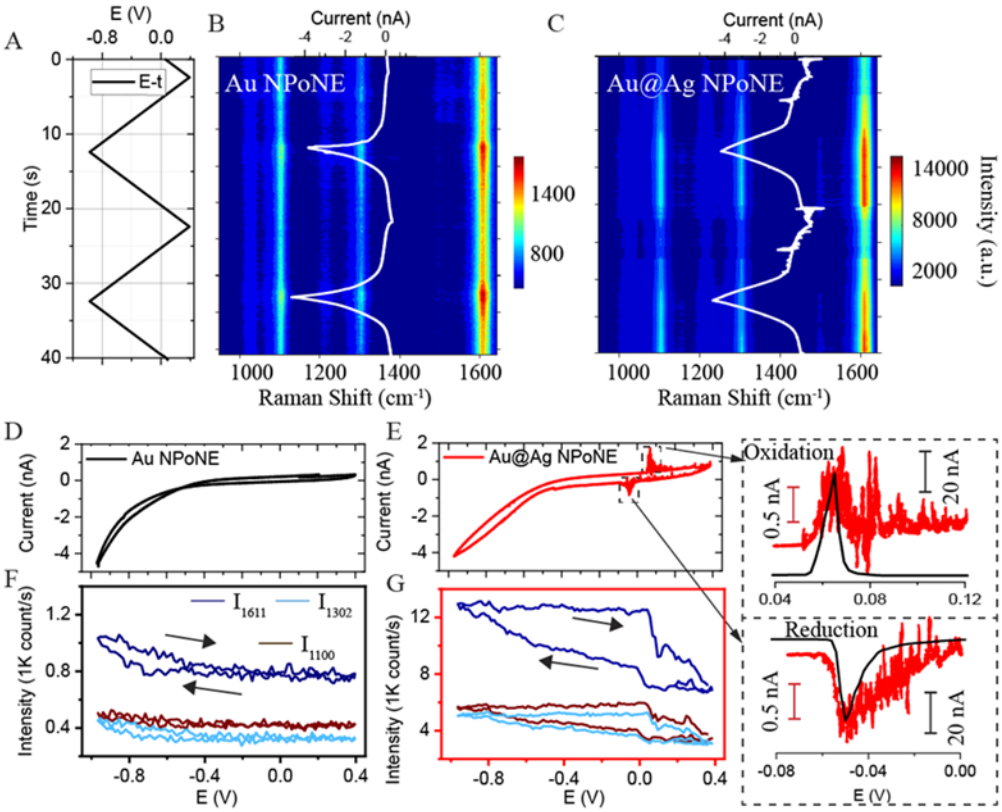

Figure 4-7 The comparison of CV and SERS measurements of Au and Au@Ag NPoNE structures. (A) The triangle waveform applied to the AuNE in 1xPBS electrolyte. Sweep rate: 0.14 V/s. (B-C) The SERS intensity heatmap of BPT in the nanocavities of Au NPoPE (B) and Au@Ag NPoPE (C) structures. SERS spectra were recorded at 10 frame/s. The EC current (solid white line) is superimposed on the heatmp. (D-E) EC current and SERS intensity of three main peaks of BPT as a function of E for Au NPoPE (D) and Au@Ag NPoPE structures. Arrows indicate the sweeping direction of E. Right panel: zoom-in of oxidation and reduction peaks of silver on NPoNE. The oxidation and reduction peaks of a bulk silver wire electrode (black line) with adjusted height is added as the reference.

4.2.7 pH Dependent SERS Intensity Tuning of BPT in the Nanocavity of Au NPoNE

Previous studies[6, 7] have found the SERS intensity tuning of molecules in the nanocavity of plasmonic NPoM by applying -1 to 0.3 V on NPoM in the electrochemical cell. They proposed four scenarios for NPoM reconfiguration with applied potential, which tuning the local charge density and surrounding dielectric environment. The conclusion is hydrogen evolution maybe play the most important role to the SERS modulation as shown in Figure 4-8A. Hydrogen evolution will cause charge density change through BPT molecule. Figure 4-8B shows that CV of Au NPoNE in different pH electrolyte. Electrode in the lower pH shown higher electrochemical current at negative bias indicate the electrochemical reaction is hydrogen evolution. Figure 4-8C and D show the pH dependent SERS modulation of Au NPoNE. Clearly, hydrogen evolution on NP is correlate with SERS modulation.

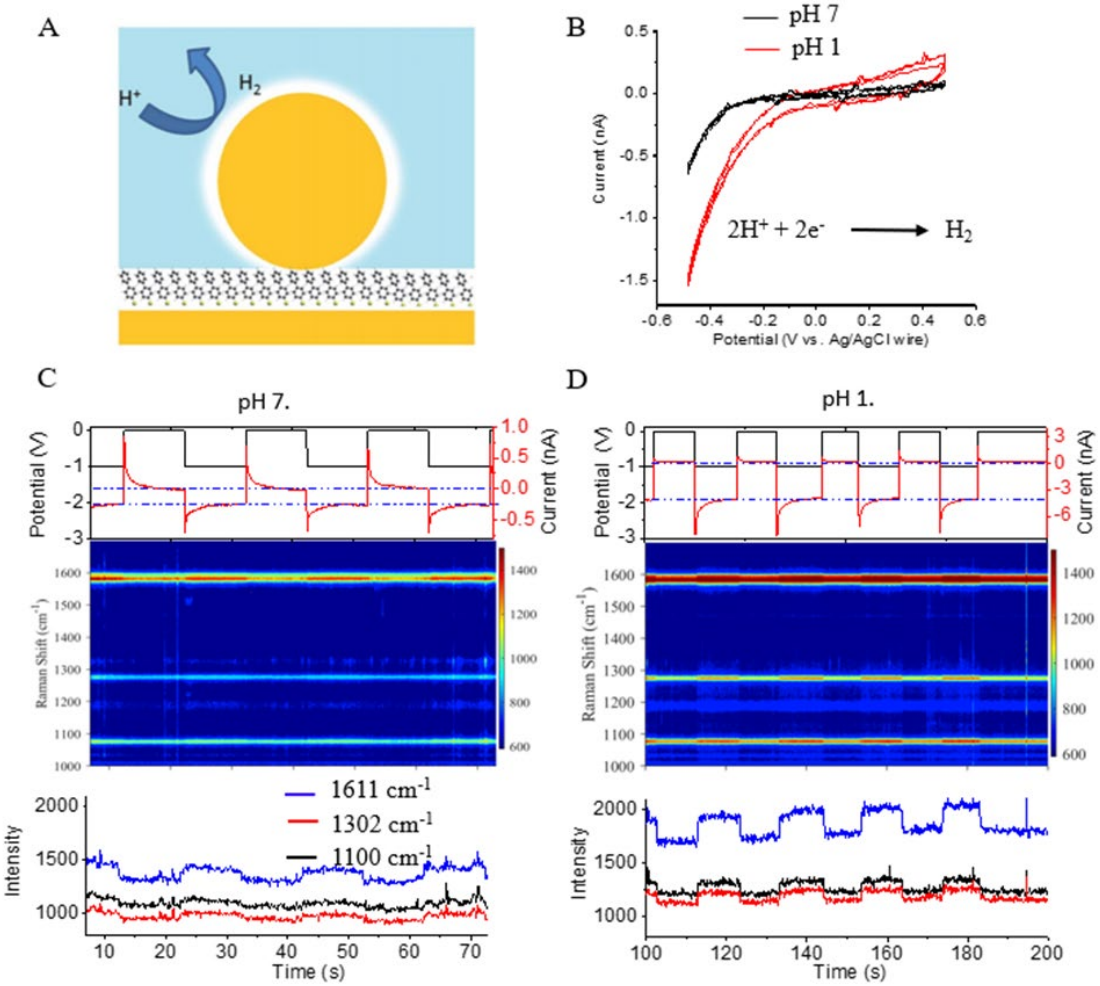

Figure 4-8 (A) Proposed hydrogen evolution model for SERS intensity modulation by electrochemical potential from literature.6 (B) CVs of Au NPoNE structures in pH 1 (red color) and pH 7 (black color) electrolyte solution. (C-D) SERS intensity tuning in the electrolyte with pH 7 (C) and pH 1 (D).

4.2.8 CV of Au@Ag NPoNE in the Electrolyte Without Chlorine Ion

Comparing the effect of chlorine ion concentration in the electrolyte to the oxidation reaction of Ag. We replaced the 137 mM NaCl in the electrolyte to $NaNO_3$ and 2.7 mM KCl to KNO_3. Figure 4-9 is the CV of the fabricated Au@Ag NPoNE. No oxidation peak observed at E = 0.07 V.

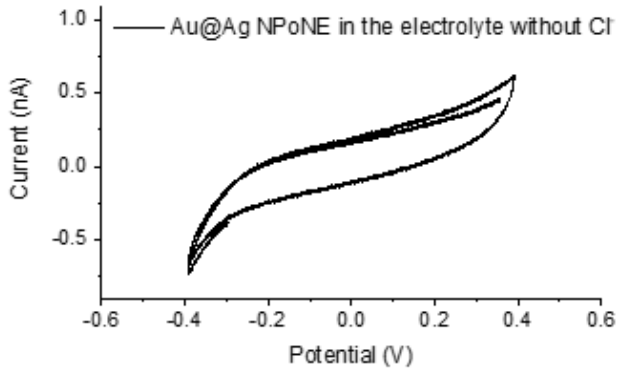

Figure 4-9 The CV of the Au@Ag NPoNE in a phosphate buffer without chloride ions (80 mV/s).

4.2.9 Simulations of Electromagnetic Enhancement in Au@Ag and Au@AgCl NPoNE Structures

To better understand the geometry of the nanocavity and the potential modulation mechanism, we simulated the EME in the NPoNE nanocavity using Finite-Difference Time-Domain (FDTD) method. Figure 4A shows the schemes of two possible configurations we have simulated. More possible configurations were simulated in 4.2.10. The main difference is the structure of the shell. For the configuration (i), the deposited Ag covers the whole AuNP surface, leading to a full shell and a Au/Ag-molecule-Au junction configuration in the cavity. For the configuration (ii), the Ag deposition only happens on the exposed surface of the adsorbed AuNP but does not penetrate into the nanogap, leaving an incomplete shell and a Au-molecule-Au junction configuration in the cavity. Figure 4-10B shows the normalized electric field amplitude ($|E/E_0|$) distribution of the configuration (i) of Au@Ag NPoNE geometry. $|E_0|$ is the electric field amplitude of the incident laser. The 40 nm AuNP, which is covered with a uniform Ag shell of 2 nm thickness, sits on a AuNE surface modified with a SAM. Because the AuNPs have different facets,[10] we used

a facet diameter of 13 nm for the 40 nm AuNPs to form the nanogap. Considering the BPT SAM, we used a thickness of 1.3 nm with a refractive index n = 1.45 based on the previous report.[11] The greatest field strength appears in the nanogap between the Ag shell and the AuNE surface where the SAM locates, which is the so-called 'hotspot'. By applying a positive electrode potential on the AuNE, the Ag layer is transformed to the AgCl layer. The shell thickness should be slightly bigger due to the intercalation of chloride ions into the silver metal. For simplicity, we still assume the shell thickness remains as 2 nm. A dielectric constant n = 2.02 was used for the AgCl layer. Figure 4C shows the $|E/E_0|$ distribution in the Au@AgCl NPoNE geometry. The light field is greatly reduced in the nanogap, with the extension of the field to the AgCl shell.

Figure 4-10D compares the enhancement factor (EF) in the center of the nanogap as a function of position in the x-axis. The EF is the fourth power of $|E/E_0|$. The maximum EF was denoted as EF^{Ag} and EF^{AgCl} when the shell is Ag and AgCl, respectively. We also calculated EM field strength in the center of the hotspot with different d_{Ag}. Figure 4D shows the EF^{Ag}/EF^{AgCl} (solid black square dots) as a function of shell thickness from the FDTD simulation. Also, the simulation result of configuration (ii) (solid gray square dots) was ploted in Figure 4D. But configuration (ii) of Au@Ag NPoNE causes almost no intensity modulation when shell transforms from Ag to AgCl (see S7). The experiment data (red solid square) is also plotted in right y-axis for better comparison. The d_{Ag} of experiment data is based on the total charge transferred during AgCl/Ag redox process by assuming the Ag form a uniform shell on the AuNPs (see detailed calculation in 4.2.10). The experimental values of the I^{Ag}/I^{AgCl} is in between the simulated EF^{Ag}/EF^{AgCl} of configuration (i) and (ii). The descrepency is likely due to the uniform Ag depositon

assumption. It is reasonable to expect that more Ag is deposited on the exposed AuNP surface than inside the nanogap, considering the hinderd diffusion of Ag^+ ions. Thus, a more realistic configuration to include the nonuniform depositon model is shown in the inset of Figure 4-10E. Alothogh the Ag layer thickness estimation inside the cavity of experimental data is not accurate, we found configuration (i) and experiemtnal results still follow the same exponential decay equation with substitute d_{Ag} with experimental (d_{Ag}-2), supporting the proposed configuration.

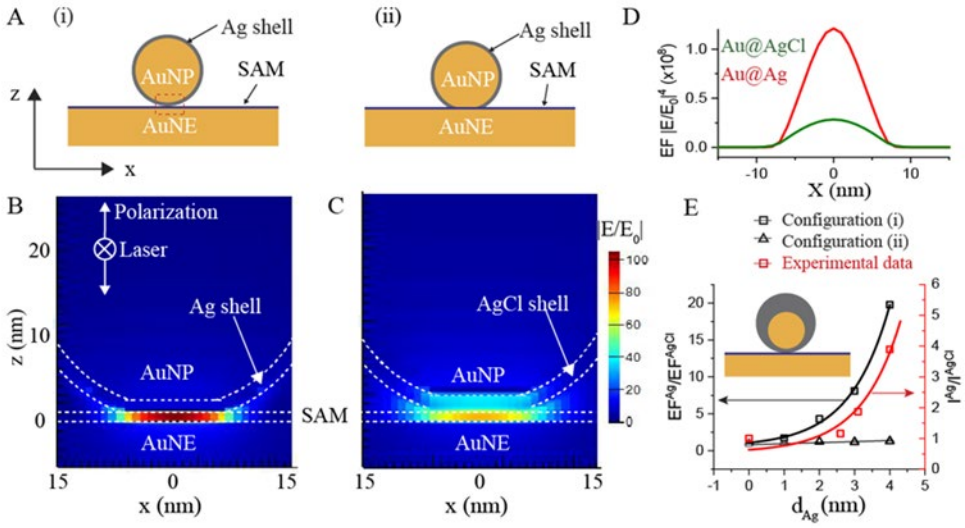

Figure 4-10 FDTD simulations of EC modulation of EME mechanism in the cavity of Au@Ag NPoNE structure. (A) Two possible configurations of Au@Ag NPoNE structures. (B-C) $|E/E_0|$ distribution in the nanogap of configuration (i) with Ag (B) and AgCl shell (C) of 2 nm thickness. The incident direction and polarization of 632.8 nm light are shown. A dielectric constant n = 2.02 was used for the AgCl shell. (D) Electric field enhancement (EF) distribution at the center of SAM (z = 0.65 nm) along the x-axis in the nanogap of (B) (red color) and (C) (olive color). (E) Left y-axis: FDTD simulation results of EF^{Ag}/EF^{AgCl} at x = 0 and z= 0.65 nm as a function of dAg for configuration (i) (black open squares) and configuration (ii) (black open triangles). The black solid line is the fit by exponential equation: $0.55\exp(d_{Ag}/1.12)+0.54$ (R^2 = 0.99). Right y-axis: Red open squares are experimental data at 1611 cm-1 of BPT, which are fitted by exponential equation: $0.55\exp((d_{Ag}-2)/1.12)+0.54$ (red line, R^2 = 0.90).

4.2.10 The FDTD Simulation of Possible Configurations

Due to up to 50 AuNPs adsorbed on the AuNE, here we ignore the curvature effect of AuNE in the FDTD simulation. Figure S7A shows the schematic structure of the Au NPoNE. Figure 4-11B is the screenshot on 3D-FDTD simulation software of the Au NPoNE structure. Figure 4-11C is the EM field surrounding a faceted 40 nm AuNP on the AuNE from FDTD simulation. Similarly, the proposed configuration (i) in the main text as shown in Figure S7D also simulated. Figure 4-11E and F are EM distribution when the shell is Ag and AgCl. Figure 4-11G plot enhancement factor profile at the center of the SAM layer. Figure 4-11H shows the enhancement factor ratio of SAM in the configuration of Au@Ag to Au@AgCl NPoNE. It shows that there is very small EF tuning ($EF^{Ag}/EF^{AgCl} < 1.3$) even with 4nm Ag shell, which is not consistent with experimental results. Also, Figure 4-11I shows configuration (iii) of possible Au@Ag NPoNE. Other than sphere shell of Ag formed on AuNP. However, the EF of configuration (iii) is even lower than Au NPoNE structure as shown in Figure 4-11J and K.

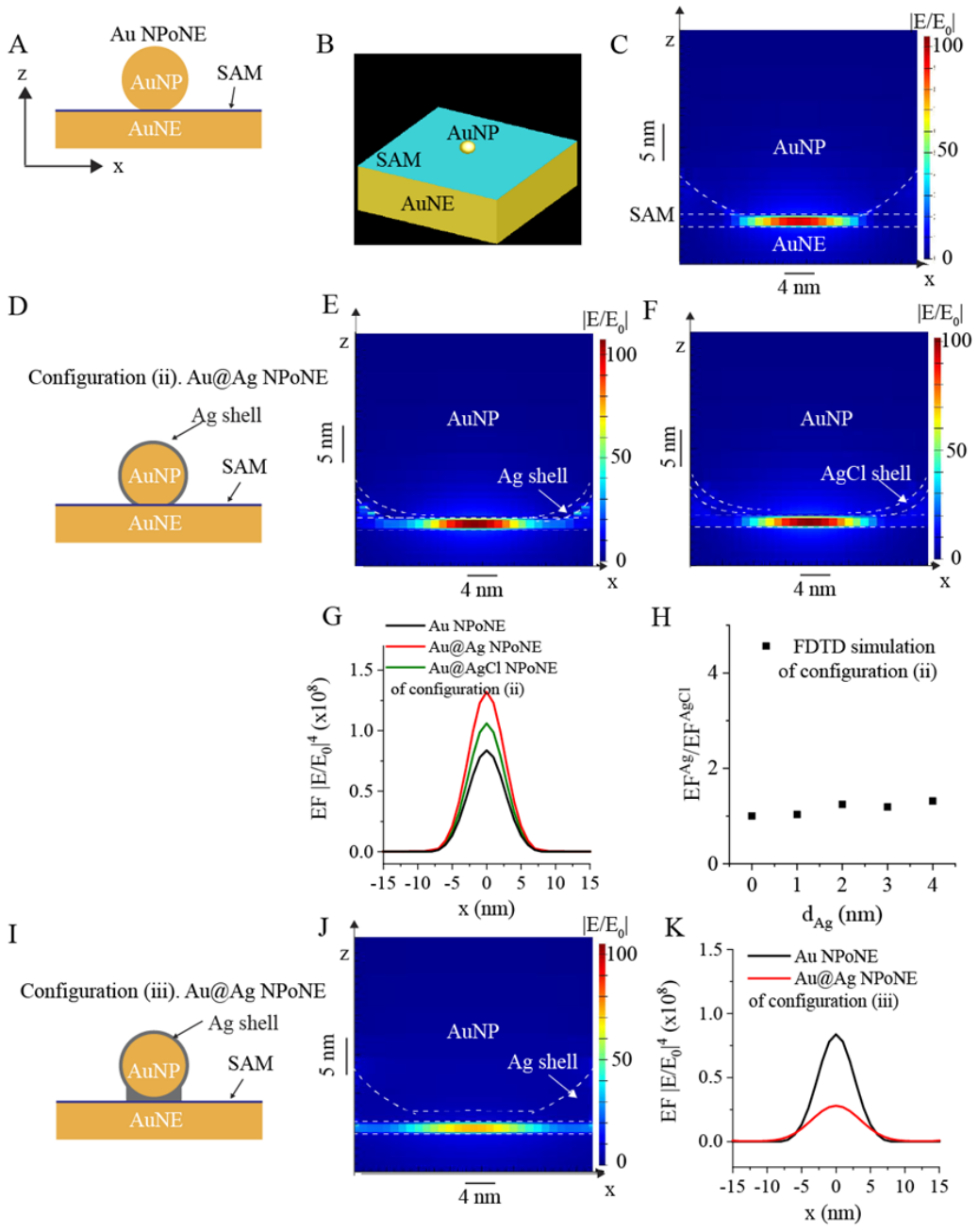

Figure 4-11. FDTD simulations of several NPoNE structures. (A) Illustration of Au NPoNE structure. (B) The 3D model of Au NPoNE structure in FDTD simulation. (C) Normalized electric field distribution ($|E/E_0|$) for Au NPoNE. (D) Schematic of Au@Ag NPoNE structure without Ag in the nanogap. (E-F) Electric field distribution for Au@Ag NPoNE (E) and Au@AgCl NPoNE (F) when $d_{Ag} = 2$ nm. (G) EF profiles at the center of SAM (z = 0.65 nm) along the x-axis for both Ag (red color) and AgCl (black color) layers. (H) The EF ratio EF_{Ag}/EF_{AgCl} at x = 0 for different d_{Ag}. (I) Another alternative configuration of the Au@Ag NPoNE structure. (J) Normalized electric field distribution for the configuration in Figure I. (K) EF profile at the center of SAM (z = 0.65 nm) along the x-

axis for this configuration and Au NPoNE.The EF profile of the Au NPoNE structure (black color curve) is also shown for comparison.

4.2.11 Modulation of Chemical Enhancement.

4-mercaptobenzoic acid (4-MBA, see Figure 4-12A) molecule has been widely used for the investigation of molecule-substrate charge transfer (CT) based CE mechanism in SERS.[12-19] We further studied the CE modulation by electrode potential using the same sytem. The scheme in Figure 4-12A shows that the carboxyl group of 4-MBA can interact with Ag, but not AgCl. As shown in Figure 5B, a square-wave potential was applied to the 4-MBA modified AuNE to modulate the Ag/AgCl transformation of the AuNP shell. The SERS intensity of all 4-MBA vibration peaks are high at E = -0.4 V, and low at E = 0.4 V. The intensity modulation by the electrode potential is fully reversible over continued cycles, which is consistent with the case of BPT molecule. Because of the Ag-4-MBA interaction, the CE mechanism also contributes to the observed intensity increase at the negative potential. To decouple the CE from the EME, the intensity of the spectra is normalized to the I_{1077} of ν(C-S), which is mainly affected by the EME but less affected by the Ag-carboxyl interaction induced CE. Figure 4-12C shows two normalized Raman spectra taken from two time spots in the SERS trajectory of Figure 4-12B, indicated by the red and green dash lines. The red and green spectra are at -0.4 V and 0.4 V, respectively. The biggest spectral change happens near 1392 cm^{-1}, which is from the stretching mode of COO^-. This mode is greatly enhanced by the Ag-carboxyl interaction at -0.4V. In addition, small relative intensity increases of the aromatic ring ν(C-C) vibration mode at 1588 cm^{-1} were observed in the normalized spectra at -0.4 V, which is also affected by the CT.

Figure 4-12D summarized the intensity modulation ratio of three major peaks for both 4-MBA and BPT molecules. The ratio I^{Ag}/I^{AgCl} is ~ 1.5 for all the bands of BPT and two bands of 4-MBA. The modulation of these bands is attributed to the EME mechanism, as discussed in FDTD simulation. However, the ratio is ~ 6.8 for the band at 1392 cm^{-1} of 4-MBA. The selective enhancement of about 4.5 times for this specific band is attributed to the Herzberg-Teller CT induced CM.[20, 21]

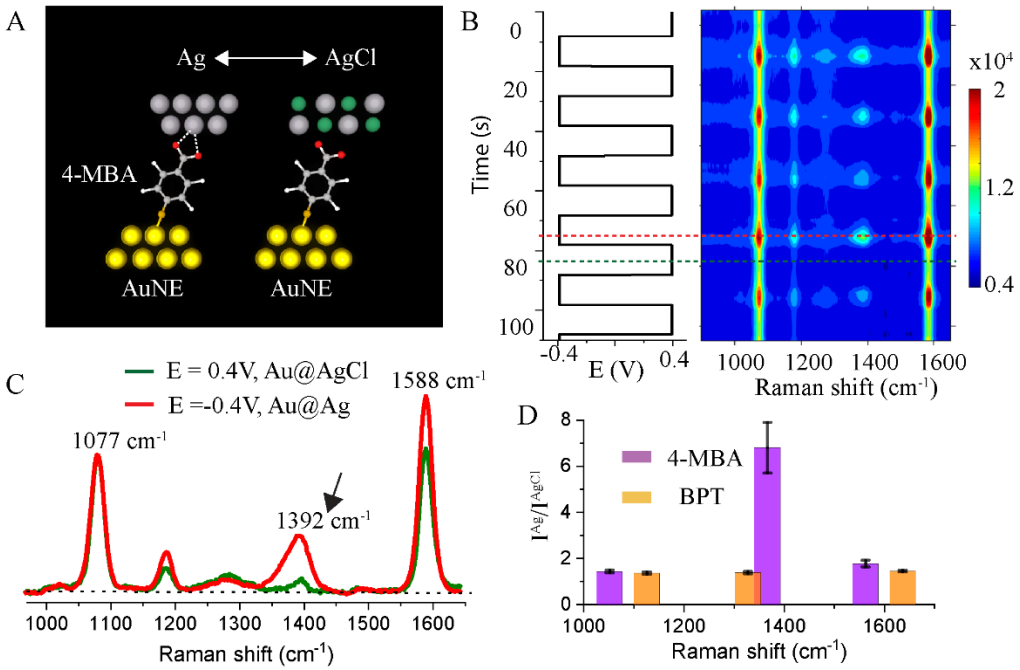

Figure 4-12 EC modulation of CM. (A) Illustration of molecule-metal interaction between 4-MBA carboxyl group and Ag or AgCl. (B) SERS intensity heatmap of 4-MBA in the nanocavity of Au@Ag NPoNE as a function of electrode potential in square waveform (|E| = 0.4 V, T = 20 s). (C) Selected SERS spectra at E=-0.4V (t = 75 s) and E=0.4V (t = 82 s) from the heatmap in (B). Black dashline is the baseline of Raman spectra. (D) The electrical tunning induced intensity ratio of three main bands for both BPT and 4-MBA molecules. The error bar is the standard deviation from 3 experiments on different AuNEs.

4.2.12 Ag Shell Thickness Estimation

Figure 4-13A shows the time trace of potential (black line) and current (red line) of the fabricated Au@Ag NPoNE. The AuNE exposure area is 80 um^2. Figure 4-13B shows current reduction peaks

of the Au@Ag NPoNE after baseline correction. Here we used the area under the current reduction peak (filled with red color) to calculate total charge transferred (Q_{total} =1.18*10^{-10} C) during AgCl/Ag redox process. We assuming the Ag formed a uniform shell on the AuNPs.

For R = 20 nm AuNP core with d_{Ag} nm shell, the volume of shell:

$V_{shell} = V_{total} - V_{core} = \frac{4}{3}\pi((20 + d_{Ag})^3 - 20^3)$ …….…….. Eq.1

The lattice constant of the Ag unit cell is 0.409 nm, the volume of a single unit cell:

$V_{unit} = (0.409)^3$ nm^3 = 0.068 nm^3……..…….Eq.2

This enables us to determine the number of unit cells making up the shell from $N_{unitcell} = V_{shell}/V_{unit}$.

Since the number of atoms per unit cell is 4, we get the total number of atoms to make up the shell:

$N_{atomshell} = 4*N_{unitcell} = 246 *(d_{Ag}^3+60*d_{Ag}^2+1000*d_{Ag})$……Eq.3

Meanwhile, for the AuNE with the exposure area A_{AuNE} = 80 um^2, the total number of AuNPs attached is N_{AuNP} = 880. As the total charge transferred is Q_{total} = 1.18*10^{-10} C, the number of Ag atoms on each AuNP is 8.6 *10^5 from the calculation of Eq.4.

$N_{atomshell} = (Q_{total})/(e * N_{AuNP})$……..……Eq.4

Where, e is the elementary charge (1.602*10^{-19} C).

Combine Eq.3 and E.4 we can calculate the thickness of Ag shell d_{Ag} = 2.6 nm.

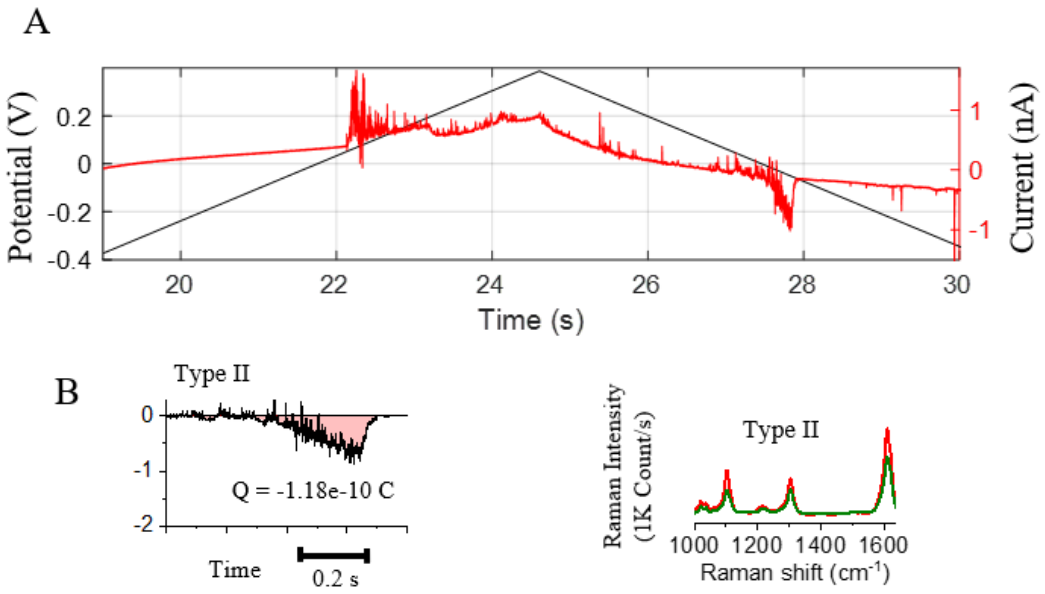

Figure 4-13 The total charge transferred used to calculate the shell thickness of silver (d_{Ag}). (A) Raw data of current and potential time trace. (B) Left: current reduction peaks of the fabricated type II Au@Ag NPoNE. Blackline is the reduction current peaks after subtracting the baseline. The area under the peak is filled with red color. Right: corresponding type II SERS tuning.

4.3 Conclusion

In summary, this study shows that effective and reversible electrochemical tuning of SERS intensity can be achieved with the assistant of the chemical transformation of the Ag shell of shell-core plasmonic NPs. The Au@Ag NP can be formed *in situ* on the SAM covered AuNE surface, and the formation of Ag shell can be interrogated in real-time through monitoring both the EC current and SERS changes. When the electrode potential was swept on the formed Au@Ag NPoNE structures, the simultaneously acquired EC current and SERS revealed the strong correlation between the redox reaction of silver shell and the SERS intensity modulation. The degree and reversibility of SERS tuning were controlled by the Ag deposition time on AuNPs. 3D-FDTD simulation confirmed the EME modulation is mainly due to the large refractive index change of the shell when the metallic

Ag is converted to insulating AgCl. In addition to the modulation of EME, the CE can also be modulated during the choloriation of Ag shell. The specific molecular-metal interaction can be switch on and off during the chemical conversion of the shell between Ag and AgCl. The combination of EME and CE modulation can further enhance the tuning effect. With the tuning of EME and CE, this work can help to better understand the EME and CE mechanisms and metal-molecule interactions in plasmonic molecular junctions. Furthermore, the *in situ* fabricating and controlling of NPs electrochemistry and SERS monitoring can easily integrate with plasmonic sensing. Direct chemical and optical electrochemistry measurements can help us fully understanding the role of plasmons and eventually utilizing for catalyzing and sensing. The electrode potential also provides a facile and fast means to tune SERS intensity and can trigger new applications in electroanalysis, heterogeneous catalysis, photocatalysis, plasmonics, molecular electronics, and biosensing.

4.4 Experimental Section

Chemicals: 4-Mercaptobenzoic acid (4-MBA, 99%) and Bipheyl-4-thiol (BPT, 97%) were purchased from Sigma-Aldrich. Phosphate buffered saline (PBS) powder (for pH 7.3−7.5), potassium chloride, and reagent ethanol (histology grade) were purchased from Fisher Scientific. Potassium ferrocyanide (98.5%) was purchased from Acros Organics. Citrate stabilized 40 nm diameter AuNPs were purchased from Ted Pella, Inc.. Silver nitrate ($AgNO_3$, 99.9%) was purchased from Alfa Aesar. All the chemicals were used without further purification. All the aqueous solutions were prepared using deionized (DI) water (~18 M ohm, Ultra Purelab system, ELGA/Siemens).

Fabrication and Chemical Modification of the AuNE: The details of electrochemical etching, insulation, and characterization of AuNEs have been reported previously.[22, 23] The tip of the cleaned AuNE was soaked in 10 mM molecule (BPT or 4-MBA) ethanol solution for a various time from 7 h to overnight. The chemically modified AuNE was then rinsed thoroughly with ethanol and dried with argon gas.

The Formation of Au@Ag NPoNE structures: The AuNE covered with a SAM was immersed in 75 pM AuNPs aqueous solution for 20 min and then rinsed to remove excess NPs. For Ag deposition, the Chronoamperometry setup was used at a constant electrode potential of -0.2 V in 10 μM $AgNO_3$ with 1xPBS as supporting electrolyte. The AuNE with adsorbed AuNPs on the SAM was served as the working electrode, and the Ag/AgCl wire was served as the quasi reference electrode.

4.5 Reference

1. Chirea, M., et al., Spectroelectrochemistry of Silver Deposition on Single Gold Nanocrystals. The Journal of Physical Chemistry Letters, 2014. **5**(24): p. 4331-4335.

2. Zhao, J., et al., Nanoparticle-Mediated Electron Transfer Across Ultrathin Self-Assembled Films. The Journal of Physical Chemistry B, 2005. **109**(48): p. 22985-22994.

3. Guo, J., et al., Dynamic single-cell intracellular pH sensing using a SERS-active nanopipette. Analyst, 2020. **145**(14): p. 4852-4859.

4. Indrasekara, A.S.D.S., et al., Dimeric Gold Nanoparticle Assemblies as Tags for SERS-Based Cancer Detection. Advanced Healthcare Materials, 2013. **2**(10): p. 1370-1376.

5. Shin, H.-H., et al., Frequency-Domain Proof of the Existence of Atomic-Scale SERS Hot-Spots. Nano Letters, 2018. **18**(1): p. 262-271.

6. Di Martino, G., et al., Plasmonic response and SERS modulation in electrochemical applied potentials. Faraday Discussions, 2017. **205**(0): p. 537-545.

7. Di Martino, G., et al., Tracking Nanoelectrochemistry Using Individual Plasmonic Nanocavities. Nano Letters, 2017. **17**(8): p. 4840-4845.

8. Choi, Y.-J. and T.-J.M. Luo, Electrochemical Properties of Silver Nanoparticle Doped Aminosilica Nanocomposite. International Journal of Electrochemistry, 2011. **2011**: p. 1-6.

9. Oje, A.I., et al., Electrochemical energy storage of silver and silver oxide thin films in an aqueous NaCl electrolyte. Journal of Electroanalytical Chemistry, 2018. **829**: p. 59-68.

10. Benz, F., et al., SERS of Individual Nanoparticles on a Mirror: Size Does Matter, but so Does Shape. The Journal of Physical Chemistry Letters, 2016. **7**(12): p. 2264-2269.

11. Benz, F., et al., Nanooptics of Molecular-Shunted Plasmonic Nanojunctions. Nano Letters, 2015. **15**(1): p. 669-674.

12. Han, B., et al., Probing the charge-transfer of Ag/PEDOT:PSS/4-MBA by surface-enhanced raman scattering. Spectrochimica Acta Part A: Molecular and Biomolecular Spectroscopy, 2020. **239**: p. 118451.

13. Guo, L., et al., Surface-enhanced Raman scattering (SERS) as a probe for detection of charge-transfer between TiO2 and CdS nanoparticles. New Journal of Chemistry, 2019. **43**(1): p. 230-237.

14. Xue, X., et al., Surface-enhanced Raman scattering of molecules adsorbed on Co-doped ZnO nanoparticles. Journal of Raman Spectroscopy, 2012. **43**(1): p. 61-64.

15. Liu, H.-W., et al., Recent progresses in small-molecule enzymatic fluorescent probes for cancer imaging. Chemical Society Reviews, 2018. **47**(18): p. 7140-7180.

16. Jiang, X., et al., Revealing interfacial charge transfer in TiO2/reduced graphene oxide nanocomposite by surface-enhanced Raman scattering (SERS): Simultaneous a superior SERS-active substrate. Applied Surface Science, 2019. **487**: p. 938-944.

17. Zhang, X., et al., Charge-Transfer Effect on Surface-Enhanced Raman Scattering (SERS) in an Ordered Ag NPs/4-Mercaptobenzoic Acid/TiO2 System. The Journal of Physical Chemistry C, 2015. **119**(39): p. 22439-22444.

18. Jiang, L., et al., Surface-enhanced Raman scattering spectra of adsorbates on Cu2O nanospheres: charge-transfer and electromagnetic enhancement. Nanoscale, 2013. **5**(7): p. 2784-2789.

19. Zhou, L., et al., Irreversible accumulated SERS behavior of the molecule-linked silver and silver-doped titanium dioxide hybrid system. Nature Communications, 2020. **11**(1): p. 1785.

20. Lombardi, J.R., et al., Charge‐transfer theory of surface enhanced Raman spectroscopy: Herzberg–Teller contributions. The Journal of Chemical Physics, 1986. **84**(8): p. 4174-4180.

21. Arenas, J.F., et al., The role of charge-transfer states of the metal-adsorbate complex in surface-enhanced Raman scattering. The Journal of Chemical Physics, 2002. **116**(16): p. 7207-7216.

22. Tuchband, M., et al., Insulated gold scanning tunneling microscopy probes for recognition tunneling in an aqueous environment. Review of Scientific Instruments, 2012. **83**(1): p. 015102.

23. Guo, J., et al., Monitoring the Dynamic Process of Formation of Plasmonic Molecular Junctions during Single Nanoparticle Collisions. Small, 2018. **14**(15): p. 1704164.

CHAPTER 5 DETECTION OF BIOMARDERS BY SERS

5.1 Introduction

The previous review papers[1-4] have shown the development of SERS-active nanoprobe for single-cell analysis. There are two types of SERS-active nanoprobes: untethered plasmonic NPs and tethered plasmonic nanoprobes, as shown in Figure 5-1. Plasmonic NPs have been attracting considerable attention in the fields of molecular recognition, medicine delivery, disease diagnosis, and cancer treatment. NPs have numerous advantages for single-cell biological applications, including the ease with which they can be functionalized with reporter molecules, low toxicity, biocompatibility, efficiency in uptaking by cells, and their ability to concentrate light around their surfaces. However, the cellular retention time is typically long, and the intracellular location of these nanoprobes is uncontrollable. The internalized nanoprobes are often trapped in the endosomes, leading to NP aggregation.

To address the problems associated with the uncontrollable location of untethered nanoparticles, a tethered substrate was used for "point-and-shoot" single-cell analysis. The tethered substrates include carbon nanotubes,[5, 6] fiber-optic tips,[1] nanopipettes, nanoelectrodes,[7] and nanopores.[8, 9] In recent years, nanopipette with the apex size of a few hundred nanometers have attracted attention for intercellular measurements. Pourmand's group has pioneered the nanopipette robotic 'nanobiopsy' system for single-cell genome sequencing. The nanopipette is also compatible with the traditional patch-clamp system. Flexible nanopipettes have been used to perform in vivo electrophysiology in live cells or tissue with minimized cell damage.[10, 11] Plasmonic nanopipettes have also

been prepared for intracellular measurements.[12-17] In addition to electrical and electrochemical measurements, SERS can be performed on the plasmonic substrate coated on the surface of a glass nanopipette. Plasmonic nanopipettes have been used for pH sensing by using pH-sensitive gold porous sphere (GPS)[9] and SERS optophysiological probes.[11] However, the ~1-micron diameter of the GPS will damage small cells, and the optophysiological probes are mainly focused on live tissue (brain) sensing applications. Although interesting, the development of plasmonic nanopipettes for intracellular measurement is still at the early stage.

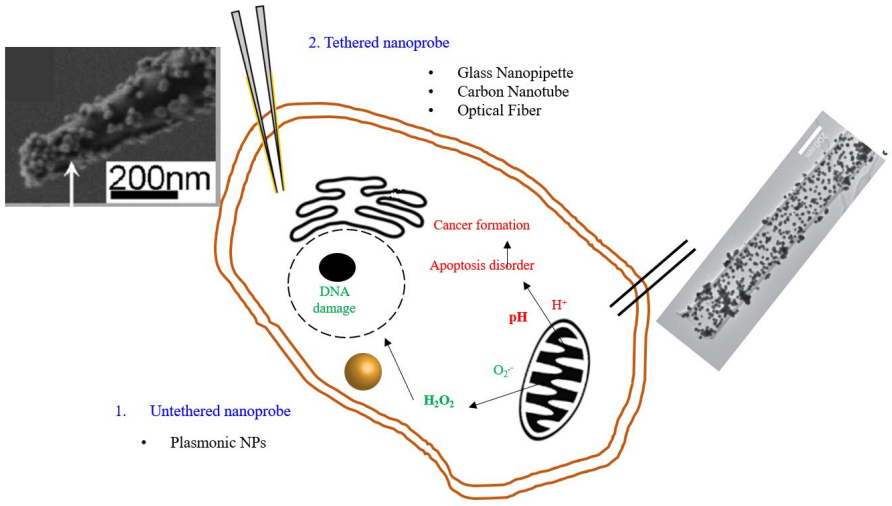

Figure 5-1 Summary of SERS nanoprobe for single cell analysis.

5.2 Untethered Gold Nanoparticle Colloid as Nanoprobe

5.2.1 Reporter Molecule Functionalized AuNPs

The method of AuNPs conjugation with different molecules is described in Chapter 2. Figure 5-2A shows the functionalized AuNPs used as a nanoprobe for intracellular sensing by the SERS technique. Figure 5-2B shows the reporter molecules which are used to functionalize the AuNPs. Different reporter molecules are used for sensing various

biochemical. AuNPs-based nanoprobes for pH, hydrogen peroxide (H_2O_2), and glucose detection were developed. Before applying to intracellular sensing, AuNPs-based nanoprobes were tested without the presence of cells. We took 100-200 μL of a colloid of prepared AuNPs-reporter molecules, then placed it in the liquid cell for SERS measurement.

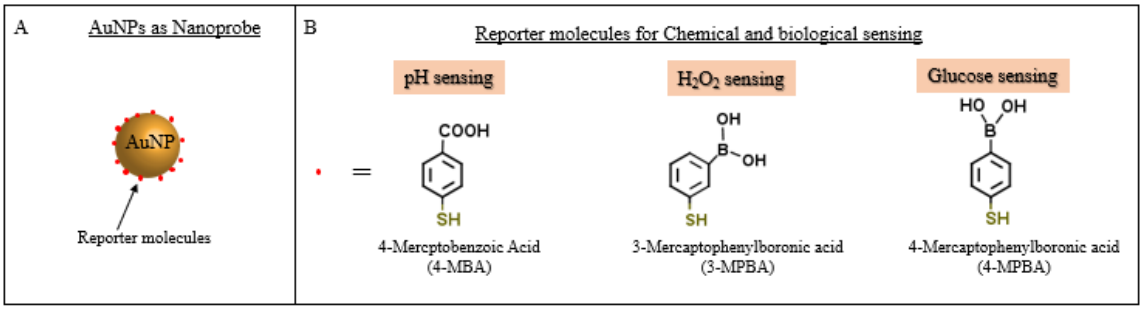

Figure 5-2 AuNPs nanoprobe for single-cell sensing by SERS. (A) Schematic of reporter molecules modified AuNP. (B) Chemical structure of reporter molecules and corresponding analyte as a highlight with an orange box.

5.2.2 Calibration of AuNPs-4-MBA as a pH Nanoprobe

Intracellular pH plays essential roles in a range of cell functions and behavior, including proliferation, metabolic state, and migration.[18, 19] Figure 5-3 shows the mechanism for the pH sensing of AuNPs-based nanoprobes. The bath solution pH would alternate the position of the proton on the carboxylic group (-COOH), which would induce a Raman spectrum change. Figure 5-3B shows the normalized spectra of AuNPs-4-MBA with different bath solution pHs. Normalization is used to avoid sample to sample variation. There are two obvious spectra intensity changes. One is associated with ν ($-COO^-$) at 1400 cm^{-1}. Their other one is from ν (C=O) at 1700 cm^{-1}. Figure 5-3C summarizes the response of AuNPs-4-MBA at the above-mentioned bands in the batch solutions of various pHs.

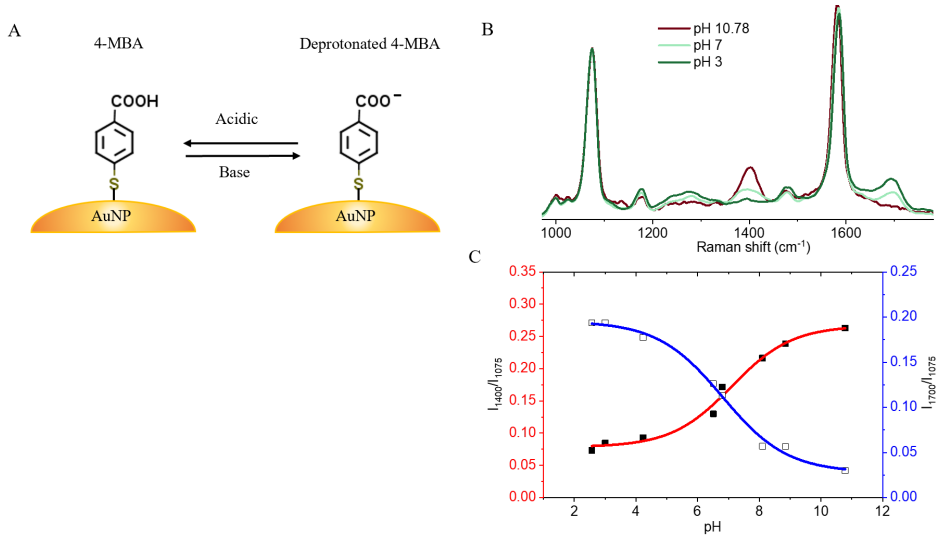

Figure 5-3 AuNPs-based pH nanosensor. (A) Mechanism of AuNPs-4-MBA as a pH nanosensor. (B) Normalized Raman spectra of AuNPs-4-MBA in the different pH bath solution. (C) The plot of ν (-COO^-) and ν (C=O) versus bath solution pH.

5.2.3 Calibration of AuNPs-3-MPBA as a H_2O_2 Nanoprobe

H_2O_2 is vital to cells as it influences cell signaling, protein folding, and biosyndissertation. [20-22] Oxidative stress is associated with the misregulation of H_2O_2. It is the cause of many diseases, such as, diabetes, chronic inflammation, cancer, and Alzheimer's. Figure 5-4A shows the mechanism of AuNPs-3-MPBA as a H_2O_2 sensor. The presence of H_2O_2 with AuNPs-3-MPBA causes the chemical transformation of 3-MPBA to 3-HTP, which gives a Raman spectrum change. Figure 5-4B shows the Raman spectra of AuNPs-3-MPBA with different concentrations of H_2O_2. The specific line at around 880 cm^{-1} for 3-HTP was used as the concentration indicator of H_2O_2. It shows the sensitivity of AuNP-3MPBA is at least 500 μM for H_2O_2 detection. The response time is around 7 min.

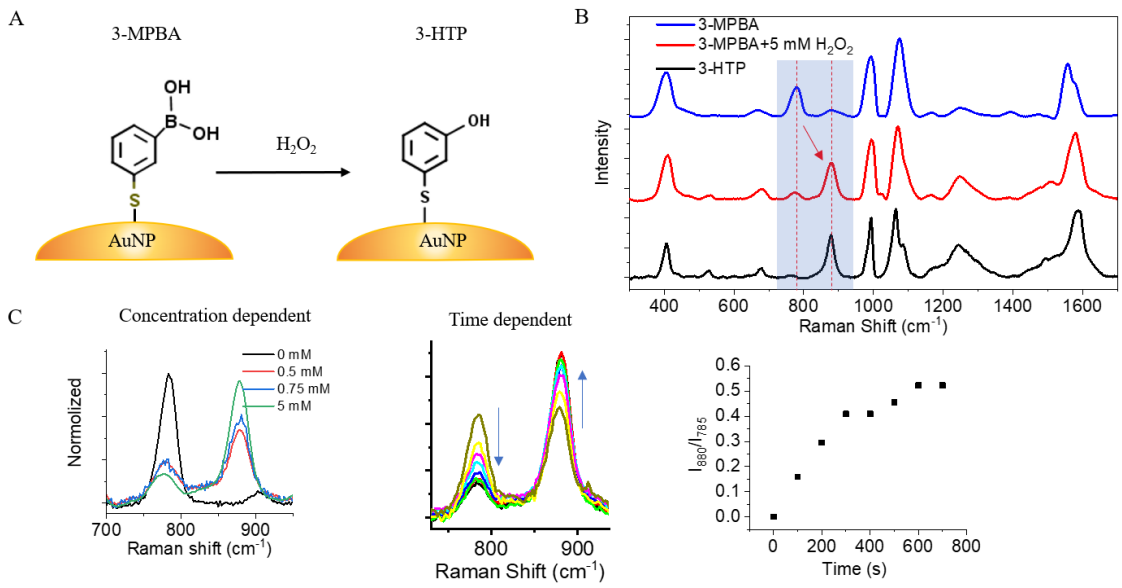

Figure 5-4 AuNPs-based H_2O_2 nanosensor. (A) Mechanism of AuNPs-3-MPBA as a H_2O_2 nanosensor. (B) Normalized Raman spectra with the band at 1000 cm^{-1} of AuNPs-3-MPBA in the different pH bath solution. (C) Raman spectra of AuNPs-3-MPBA with different H_2O_2 concentration and time-dependent.

5.2.4 Calibration of AuNPs-4-MPBA as a Glucose Nanoprobe

Diabetes is one of the top 10 causes of death, according to the World Health Organization (WHO) in 2015. Thus, the last nanoprobe is for glucose level detection. Figure 5-5A shows the mechanism of glucose detection, in which the combination between 4-MPBA and glucose breaks the symmetry of the benzene ring. [23, 24] Figure 5-5B shows the Raman spectrum of AuNPs-4-MPBA with 2.5 mM Glucose at a different time. Figure 5-5C shows the zoom-in of the bands from 1500 cm^{-1} to 1660 cm^{-1} of Figure 5-5B. Figure 5-5D summarizes the Raman intensity ratio of I_{1556}/I_{1582} versus time. It shows it takes about 13 min for the AuNPs-4-MPBA to finish the detection of glucose at a concentration of 2.5 mM.

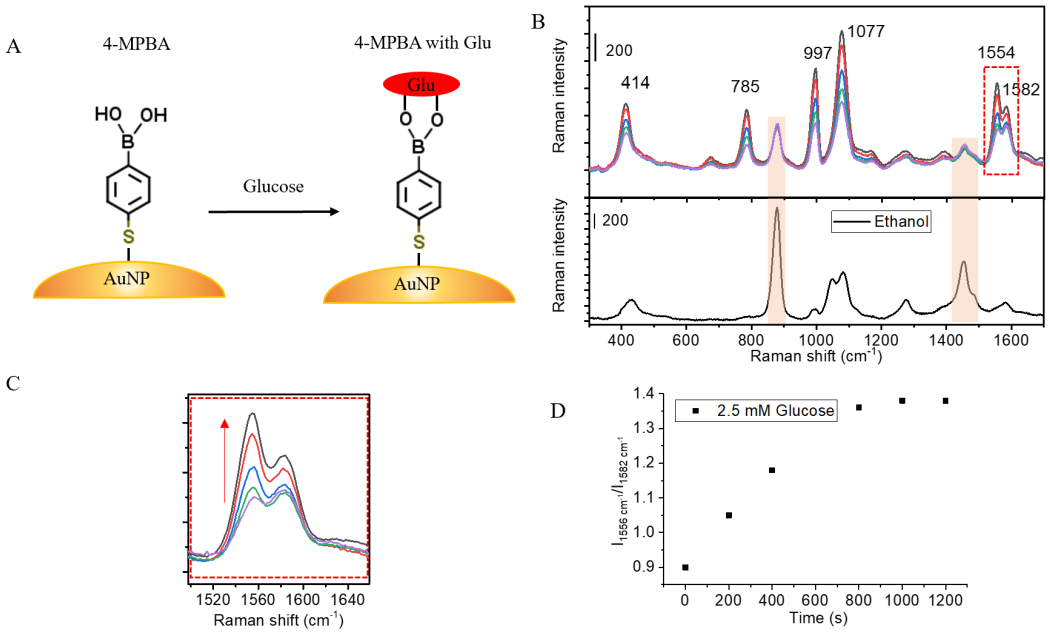

Figure 5-5 AuNPs-based glucose nanosensor. (A) Mechanism of AuNPs-4-MPBA as a glucose nanosensor. (B) Raman spectra of AuNPs-4-MPBA in 2.5 mM glucose for a different time. Bottom: the Raman spectrum of the ethanol contamination in the AuNPs-4-MPBA colloid. (C) Zoom-in of sensitive band to the presence of glucose. (D) The plot of I_{1556}/I_{1582} over time of AuNPs-4-MPBA with 2.5 mM glucose.

5.2.5 AuNPs-based Nanoprobes for Single Cell pH Sensing

After the calibration of AuNPs-based nanoprobes, they were applied for single-cell analysis. Figure 5-6 shows the brightfield image (BF) and darkfield image (DF) of HEK293 cells with and without incubation with AuNPs. The bright spot in the DF image of HEK293 cells indicates the location of AuNPs inside the cell.

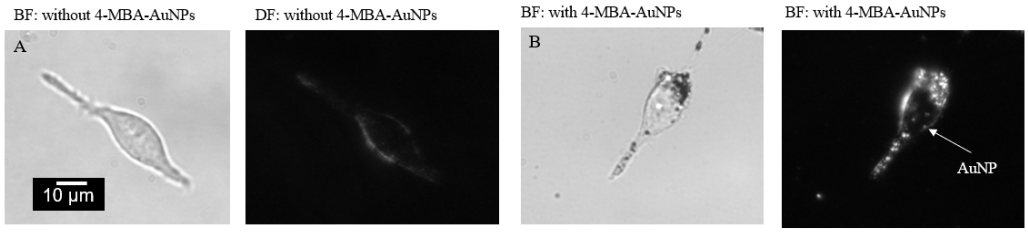

Figure 5-6 Darkfield image of AuNPs incubated HEK293 cells.

With the evidence that AuNPs enter the cell, SERS measurements were performed on those AuNPs. Figure 5-7A shows the SERS spectra of 4-MBA modified AuNPs inside the cells. The spectra of the majority of the AuNPs-4-MBA are shown in Figure 5-7A in blue and red. Note how the these are distinct from the black calibration spectrum. Only minor locations of AuNPs-4-MBA (black spectra in Figure 5-7A) shown the same spectra as calibration. Thus, we only chose the spectra similar to the black spectrum to indicate the intracellular pH. This is summarized in Figure 5-7B. Figure 5-7 B shows the results of different incubation times of AuNPs-4-MBA with HEK293 cells. Different incubation times gives similar I_{1400}/I_{1077}. In comparison with the calibration curve shown in Figure 5-3C, the pH of AuNPs-4-MBA located inside the cell is around 5.6. The acidic pH indicates that those AuNPs-4-MBA were in the endosome of the cell, which cannot represent the intracellular pH.

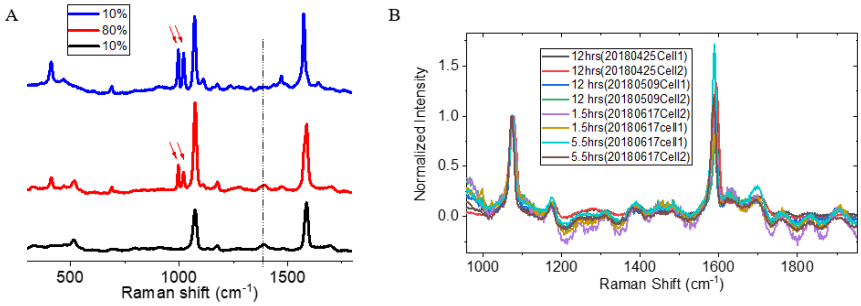

Figure 5-7 (A) SERS spectra of AuNPs-4-MBA in HEK293 cells. The red arrow indicates the new bands show up. The dashed line indicates the pH-sensitive band. (B) Summarize useful SERS spectra of AuNPs-4-MBA in HEK293 cells with different AuNPs incubation time.

Figure 5-8 shows the SERS spectra of AuNPs-3-MPBA inside the HEK293 cells. The responding bands (red arrow) of 3-MPBA to analyte disappear when AuNPs aggregate inside the cells. A similar phenomenon was observed for the 4-MBPA reporter molecule.

Since the reporter molecules of 3-MPBA and 4-MPBA did not respond to the analyte, I will not continue the investigation with those reporter molecules. My assumption is the chemical transformation of the reporter molecule in the hot spot of AuNPs aggregations as their Raman spectrum changed compared to those AuNPs used in the colloid and DFT calculation.

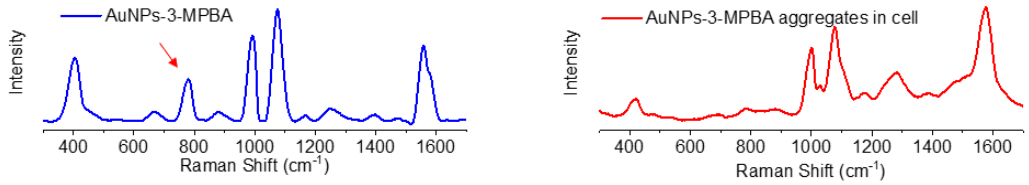

Figure 5-8 Same reporter molecule when AuNPs are colloid (blue) and aggregates (red).

5.3 AuNPs-loaded Nanopipette as Nanoprobe for Intracellular pH Sensing

Herein, we developed a SERS-active nanopipette for intracellular pH (pH_i) sensing for individual eukaryotic cells. The pH_i is an important parameter for regulating cellular functions, behaviors, and pathological conditions.[18] However, effective intracellular sensors are still limited.[25] We further reduced the nanopipette apex size to below 200 nm. The geometry of the nanopipette has also been optimized to increase its flexibility, which minimizing cellular damage during the insertion of the nanopipette. By optimizing the distribution, density, and surface chemistry of the adsorbed AuNPs on the outer surface of the nanopipette, we obtain a uniform, stable, and reproducible SERS-active substrate with a high enhancement of Raman intensity. Molecule 4-mercaptobenzoic acid (4-MBA) was used as the probe molecule, and the ratiometric intensity signal of COO^- stretching vibration mode was calibrated for pH sensing. To evaluate the dynamic response of the nanopipette to pH changes in real-time, the nanopipette was first tested in the controlled

fluidic flow in a microfluidic device. Then, the nanopipette was applied to study the pH_i change of individual live cells. By changing the extracellular pH (pH_e), we compared the cytoplasmic pH changes between cancer cells and normal cells.

5.3.1 Cell Damage Test with the Insertion of Nanopipette

Nanopipette has been successfully used in intracellular studies. However, the insertion of nanopipette into small mammalian cells may damage the cell membrane.[26, 27] With the aim of minimizing the cellular damage, both the apex size and the stiffness of the nanopipette tip are optimized. In a recent report, the nanopipette showing minimized invasive in the intracellular measurement has a spring constant of 0.08 N/m.[10] Therefore, we prepared nanopipettes with a long-taper (shank length ~12.2 mm) geometry and a small tip diameter (sub-200 nm) using a pipette puller. The short-taper nanopipette was used as a comparison. The parameters for long-taper nanopipette: HEAT = 500, FIL = 4, VEL = 50, DEL = 255, PUL = 100. Parameters for short-taper nanopipette: HEAT = 400, FIL = 4, VEL = 50, DEL = 255, PUL = 150. The optical images of long-taper and short-taper nanopipette are shown in Figure 5-9A. We can see the short-taper is about half the length of long-taper. Figure 5-9B and C show the SEM images of side-view of long-taper and short-taper nanopipette, which can provide dimension information. From classical beam theory, the spring constant k for a hollow cylindrical tube can be approximated by Equation (1) with the cantilever approximation.

$$k = \frac{3*E*I}{L^3} \qquad (1)$$

Here $I \approx \pi * R^3 * t$ is the geometric moment of inertia of a cylindrical tube. E is Young's modulus of the material (70 x10^9 N/m^2 for quartz). L is the length of the cylindrical tube. The model is shown in Figure 5-9D.

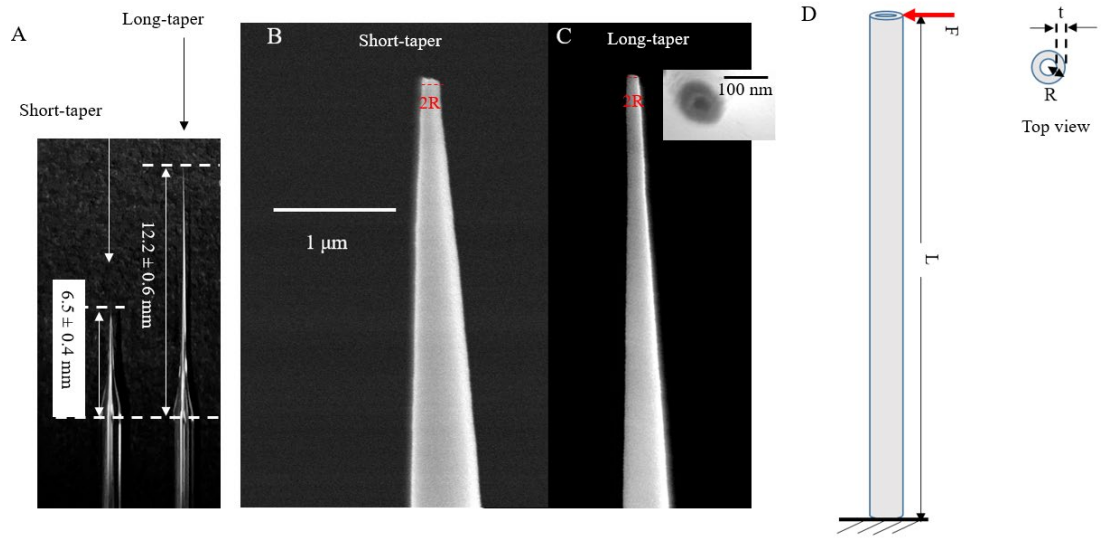

Figure 5-9 (A) Optical images of short-taper and long-taper nanopipettes. (B) and (C) SEM images of short-taper and long-taper nanopipette, respectively. The inset image in (C) is the top view of long-taper nanopipette. (D) Schematic drawing of the cantilever approximation model for the beam theory.

Here, we treated the tip section as a cylindrical tube with the radius R. The radius is indicated in Figure 5-9B and C with a red line. The thickness t of the tube can be estimated from the top view of nanopipette, as indicated in the inset of Figure 5-9C. The derived spring constant k is around 0.056 N/m and 0.504 N/m for long-taper and short-taper nanopipette by using Equation 1, respectively.

We used a Trypan blue assay to evaluate the cellular damage induced by the intrusion of the long-taper nanopipette. A stiff nanopipette was used as the control. Fibroblast live cells on the cover glass are immersed in 1xPBS with 0.04% Trypan blue dye. When observed by naked eyes using the microscope, the cell inserted by the short-

taper nanopipette tip shows blue color only after 2 min, suggesting the cell is dying. Recorded by a black and white CCD camera, the dead cell appears darker (enclosed by the blue color circle) in the gray-scale image, as shown in the left panel of Figure 5-10. However, the cell inserted by the long-taper nanopipette tip still remains clear in the image after 60 min, as shown in the right panel of Figure 5-10.

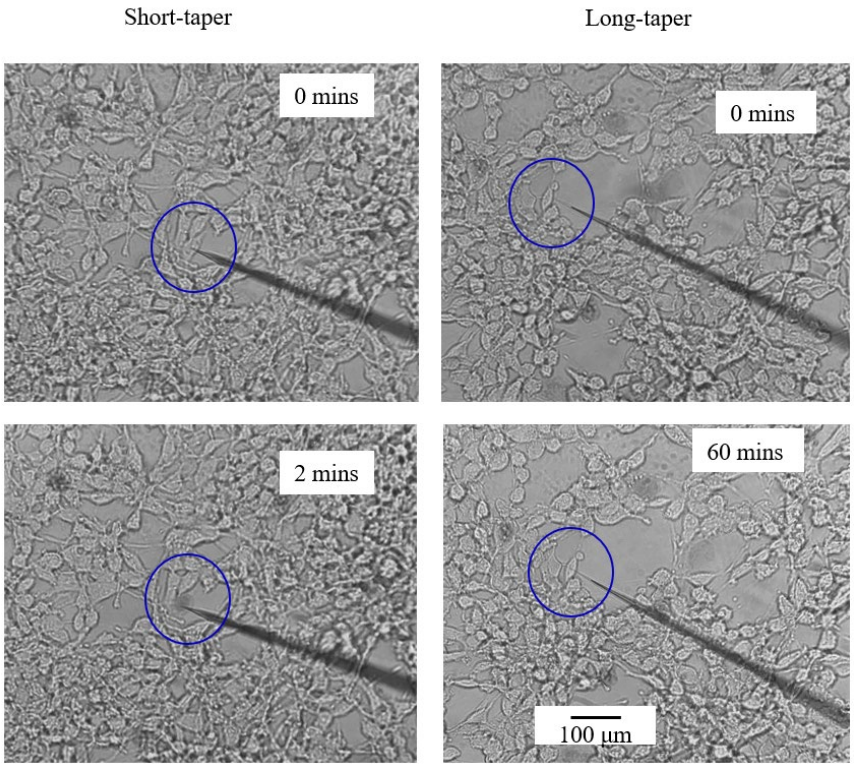

Figure 5-10 Optical images of Fibroblast cells immersed in 1xPBS buffer solution with 0.04% trypan blue. Left: Insertion of a short-taper nanopipette probe. Right: Insertion of a long-taper nanopipette probe.

5.3.2 AuNPs-loaded Nanopipette Fabrication

In order to demonstrate the flexibility of the long-taper nanopipette, the nanopipette tip is bent ~ 30° at a distance ~3.4 mm from the apex and is then fully recovered after relaxing, as shown in Figure 5-11A. The flexible tip can be repeatedly bent without

breakage. It demonstrates that the flexible long-taper nanopipette is preferable for intracellular measurements. Figure 5-11B shows fabrication procedures. The prepared long-taper glass nanopipette was soaked in 0.4 % (v/v) ethanol solution of APTES for 1.5 hrs. After rinsing with ethanol, the nanopipettes were dried by the argon gas flow. Subsequently, APTES modified nanopipette was immersed in 150 pM AuNPs with 40 nm diameter for a different time at 40 ºC in the refrigerator. To introduce a reporter molecule 4-MBA, the AuNP modified glass nanopipette was soaked in 1 mM ethanol solution of 4-MBA for 1 hr. After cleaning, the prepared nanopipette was stored in 1x PBS before use.

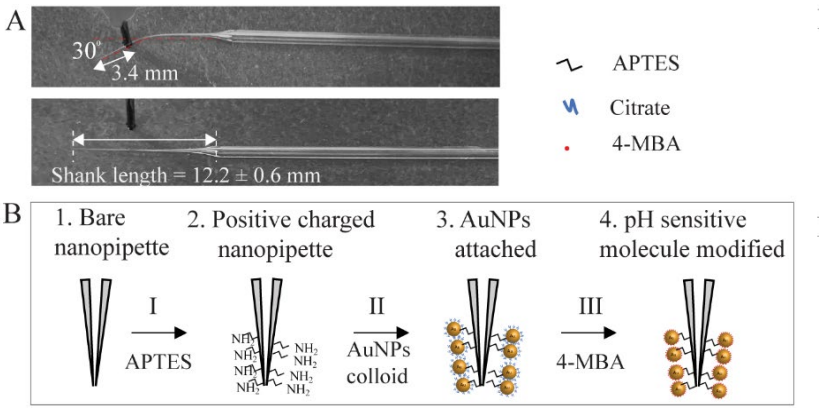

Figure 5-11 (A) Optical images demonstrate the flexibility of a long-taper nanopipette tip. (B) Scheme of the procedures for surface modification of a pH-sensitive nanopipette (not to scale).

The previous simulation results have shown that the optimization of the SERS substrate can be achieved by controlling the AuNP coverage. We altered the AuNP deposition time to control the surface coverage of the AuNPs on the nanopipette tip while keeping the conditions of other steps the same. Figure 5-12C shows the SEM images of the nanopipette tip after immersing the APTES modified nanopipette in colloidal AuNP solution for different time intervals. Before the deposition of AuNPs, the outer and inner diameters of the nanopipette are around 100 nm and 30 nm, respectively. After 60 min of

deposition, the outer diameter of the nanopipette is increased to approximately 170 nm, revealing the adsorption of one sublayer of 40 nm AuNP. The inner channel remains open, as indicated by the red arrow in Figure 5-12C. After 120 min of deposition, the AuNP layer becomes much thicker with a multi-layer configuration. The inner diameter of the pore is also significantly reduced or even entirely blocked. Based on the SEM images, we can estimate the average number density of AuNPs on the nanopipette tip. As shown in Figure 5-12D, the surface number density of AuNP increases linearly at a rate of 3.2 min^{-1} μm^{-1} during the deposition of the first 60 min. At 60 min, the surface number density of AuNP is about 202 μm^{-2}.

Even though only flexible and apex size < 200 nm can apply for single cell analysis. We still fabricated different apex size AuNPs-loaded nanopipette by same procedure, as shown in Figure 5-13. Bigger size nanopipette gives more stable and better signal-to-noise ratio Raman spectra but may introduce more damage to small cells. Thus, it is important to choose wisely of different size nanopipette according to the size of the sample and for different applications. For our intracellular sensing, the small size (~ 200 nm) AuNPs-loaded nanopipette was calibrated and used.

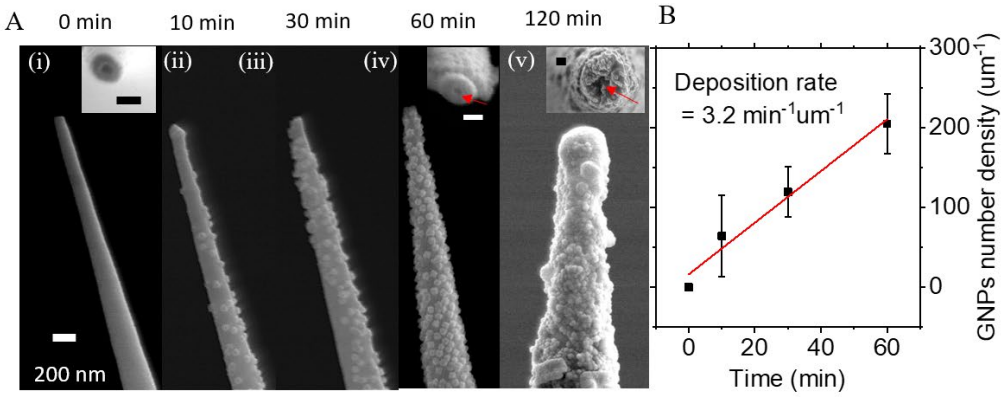

Figure 5-12 (A) SEM images of the nanopipette tip with different AuNP deposition time, ranging from 0 min to 120 min. The inset images are the top view of the nanopipette orifice. The scale bar is 100 nm in inset images. (B) The AuNP number density at the tip (2 μm from the apex) as a function of the AuNP deposition time.

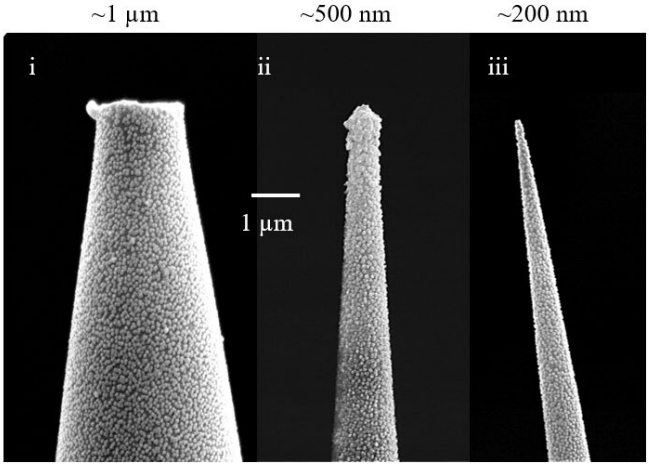

Figure 5-13 SEM images of AuNPs-loaded nanopipettes with different pulling parameters.

5.3.3 Decide Optimal AuNPs Density for pH Sensing

After modifying 4-MBA molecules to the AuNP surface, Raman spectra were taken at the tip of the AuNP-loaded nanopipette in 1xPBS. As shown in Figure 5-14A, the overall 4-MBA Raman intensity increases with the increase of the number density of AuNP at the tip. The nanopipette with a higher AuNP density possesses more plasmonic AuNPs and nanogaps, inducing a higher electromagnetic enhancement of SERS intensity. Figure 5-14B shows the same Raman spectra of 4-MBA in Figure 5-14A normalized to the peak at 1077 cm^{-1}. The band at 1400 cm^{-1} Raman spectra (indicated by the red arrow) is used for pH sensing. This band will be further discussed in the next section. When the AuNP number density is too high (the red color spectrum), the intensity of this band decreases obviously along with the appearance of two new bands[28, 29] near the 1077 cm^{-1} peak (indicated by the black arrows). Thus, there is an optimal thickness for the AuNP layer.

We have determined that the thickness of the AuNP layer after 60 min of AuNP deposition is the best for pH sensing.

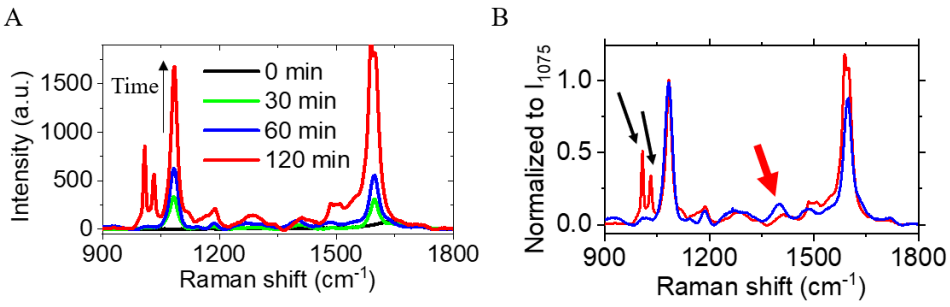

Figure 5-14 (A) Typical Raman spectra of 4-MBA from the AuNP-loaded nanopipette tip after different AuNP deposition time. (B) Normalized Raman spectra of 4-MBA after 60 min (blue line) and 120 min (red line) AuNP deposition time.

5.3.4 pH Calibration of pH-sensitive SERS-active AuNPs-loaded Nanopipette

Figure 5-15A illustrates the pH-sensing mechanism of 4-MBA molecule. The carboxyl group of 4-MBA is protonated at a lower pH and deprotonated at a higher pH, leading to changes in the Raman spectrum. Figure 5-15B shows the pH-dependent Raman spectra of 4-MBA, collected from a fabricated pH-sensitive nanopipette. To avoid sample-to-sample variations, we used the ratiometric method to characterize the pH-dependent response of the SERS signal. Here, the band at 1077 cm^{-1}, from the stretching mode of C-S coupled with the benzene ring, is used as the internal reference. All other bands in the SERS spectra were normalized to the internal reference (all SERS spectra shows after this point were normalized if not mentioned otherwise). The bath solution pH value varies from 4.3 to 10.1 results in the systematic changes in four major spectral regions, as marked with numbers (i) to (iv) in Figure 5-15B. Figure5-15C shows the zoom-in of the four pH-sensitive spectral regions. We assigned the Raman bands based on the literature [30-33] and our density

functional theory (DFT) calculation (Figure 5-16). Figure 5-15C(i) shows the bands at 688 and 847 cm^{-1}, which are attributed to the bending mode of δ(COOH) and δ(COO^-). The two peaks decreased and increased concurrently with pH due to the deprotonation of -COOH, respectively. However, these bands were often overlapped with the bands from the glass substrate (see details in Figure 5-17). Figure 5-15C(ii) shows the pH-dependent change of band at 1400 cm^{-1}, which is assigned to the symmetric COO^- stretching mode (ν(COO^-)). Its intensity increases with the increase of solution pH. Figure 5-15C(iii) shows the pH-dependent band at 1703 cm^{-1}, which is attributed to the stretching mode of the carbonyl group (ν(C=O)). Its intensity decreases with the increase of solution pH. However, if the overall SERS intensity is weak, like the case of intracellular measurement, the bending mode of water molecules at 1640 cm^{-1} may interfere with this mode (see Figure 5-17). Figure 5-15C(iv) shows the change of band at 1592 cm^{-1}. This band redshifts (to the lower wavenumber) 4 cm^{-1} as the solution pH increases from 4.3 to 10.1, which is due to the breaking of symmetry upon the deprotonation of the carboxyl group. However, this Raman shift is too small considering the 2 cm^{-1} spectral resolution of our setup. However, this band can be useful if we increase the spectral resolution of the spectrometer.

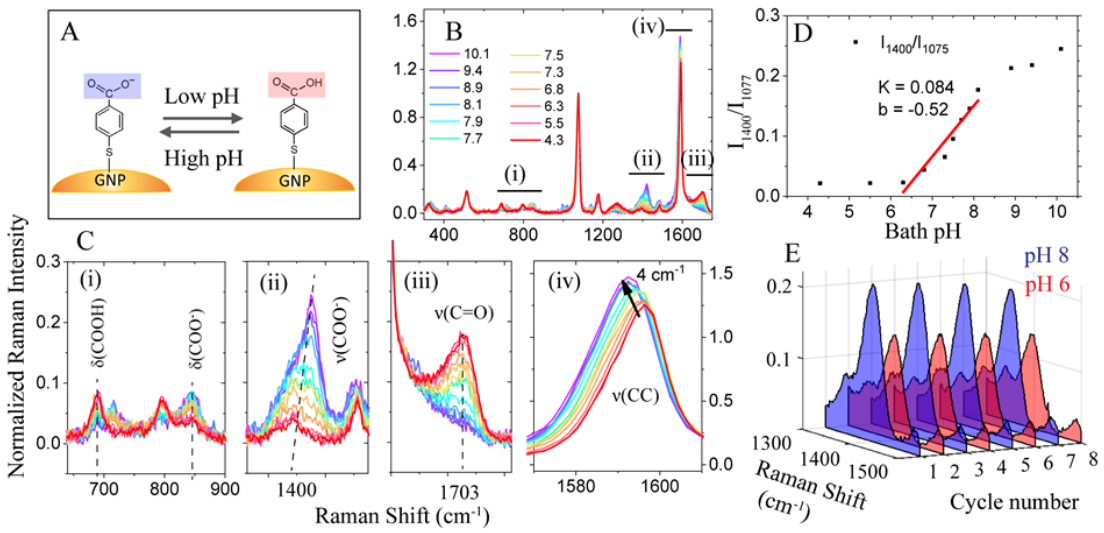

Figure 5-15 (A) Schematic of the reversible changes of the carboxyl group of 4-MBA as a result of pH changes. (B) The SERS spectra of the SERS-active nanopipette at different solution pH values. (i)-(iv) are four zoom-in bands. (C) Zoom in of four bands as indicated in Figure 5-15B. (D) pH calibration curve obtained by plotting the ratio of 1400 cm^{-1} against different pH values. The black dots are fitted by a linear regression equation and plot as a solid red line. (E) The 3D SERS spectra of the normalized intensity change of 1400 cm^{-1} when the solution pH was switched between 8 and 6 for 8 cycles.

All four regions can be used to detect local pH changes for different applications. Among them, we find the band at 1400 cm^{-1} in Figure 5-15C(ii) is the most robust and sensitive peak for the cellular application. Therefore, we use this band for the following experiments. Figure 5-15D shows the plot of intensity ratio I_{1400}/I_{1077} versus bath solution pH, in which the most sensitive pH range is from 6.0 to 8.0. A linear fit to the data in this dynamic range gives a slope of 0.084. The noise level of the normalized intensity is about 0.015, which gives the pH sensitivity of 0.2 units. The measured slope values vary from 0.029 to 0.084 for different nanopipettes. Therefore, it is important to obtain the calibration curve for each nanopipette. The reproducibility of the nanopipette for pH sensing was also tested. Figure 5-15E demonstrates the spectral changes of the normalized intensity of the $\nu(COO^-)$ mode between pH 6.0 (red color) and 8.0 (blue color) is reproducible. Let's

compare the performance of developed SERS probe for pH measurement with the commercialized fluorescent probe: pHrodo Red and pHrodo Green. They give comparable results in terms of sensitivity (<0.2 pH units) and stability (>12 min). However, there are potential advantages of SERS over fluorescence. 1) With proper SERS-active substrate (SERS), other biomarker detection can be realized simply by changing suitable reporter molecules. 2) SERS can be used for multiparameter simultaneous determination by combine several reporter molecules together on SERS-active substrate. Multiple biomolecular signatures will provide a more complete picture of the complex biological system while single biomarker detection only gives limited information.

We have used density functional theory (DFT) (Gaussian 09 package) to calculate the Raman spectra of 4-MBA molecule on gold. The geometry of the Au3-4-MBA molecular model with a neutral charge is shown in Figure 5-16A. The gold NP was represented by a Au3 cluster. The DFT calculation was conducted based on the energy minimized ground-state geometry using hybrid exchange–correlation functional (B3LYP). The 6-31G** basis set was used for molecule and LANL2DZ basis set was used for gold atoms. As shown in Figure 5-16B, the calculated and measured SERS spectra of 4-MBA (at pH 4.2) matched very well. The mode assignments to the SERS spectrum based on the DFT calculation are summarized in the table of Figure 5-16C.

A

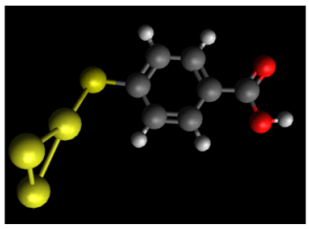

B

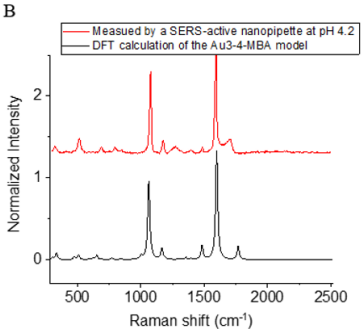

C

4-MBA	
Assignment	**Raman shift (cm^{-1})**
ν(CS) (b2)	320
γ(CCC) (ring, out-of-plane bending)	516
δ(COOH) (in-plane-bending)	688
δ(COO^-) (in-plane-bending)	847
Ring breathing (a1)	1012
ν(CC)+ν(CS) (a1)	1077
δ(CH) (in-plane-bending (a1))	1186
ν(COO^-)(stretching)	1400
ν(CCC) (Ring stretch (a1))	1592
νC=O (stretching)	1703

Symbols: *ν*, stretching; *δ*, deformation or in-plane bending; *γ*, π, out-of-plane bending; *ω*, wagging; *τ*, torsion; *ρ*, rocking; s, symmetric; as, antisymmetric.

Figure 5-16 (A) Molecular structure of the Au3-4-MBA model used for the DFT calculation. (B) The SERS spectrum measured from a SERS-active nanopipette tip at the acid condition (red color) and the DFT calculated Raman spectrum (black color). (C) The table of Raman bands assignment for 4-MBA.

Figure 5-17 shows the schematic of the experimental setup for the calibration (Left) and the actual (Right) live-cell experiments. The main difference is that the nanopipette tip position is different. The nanopipette tip needs to be very close to the cover glass surface to get into the cell for the intracellular sensing. Thus, the cover glass is close to the focus plane of the lens. Therefore, we observed the weak Raman signal from the cover glass in the intracellular measurement, as shown in the spectra of Figure 5-17C. In the calibration, no Raman signal was observed from the cover glass. In addition, the Raman signal of the live-cell experiment is generally weaker, likely due to the extra light scattering by the cell. We therefore used a longer exposure time of 2 s for the live-cell experiment. Although the signal-to-noise ratio is obviously increased, the tradeoff is that the water peak becomes noticeable with the longer exposure time. Fortunately, there is still a clean spectral window in the Raman spectra for the pH sensing, as highlighted with the green color in the spectra

of Figure 5-17C. This is the other reason I_{1400}/I_{1077} was used as the pH probe.

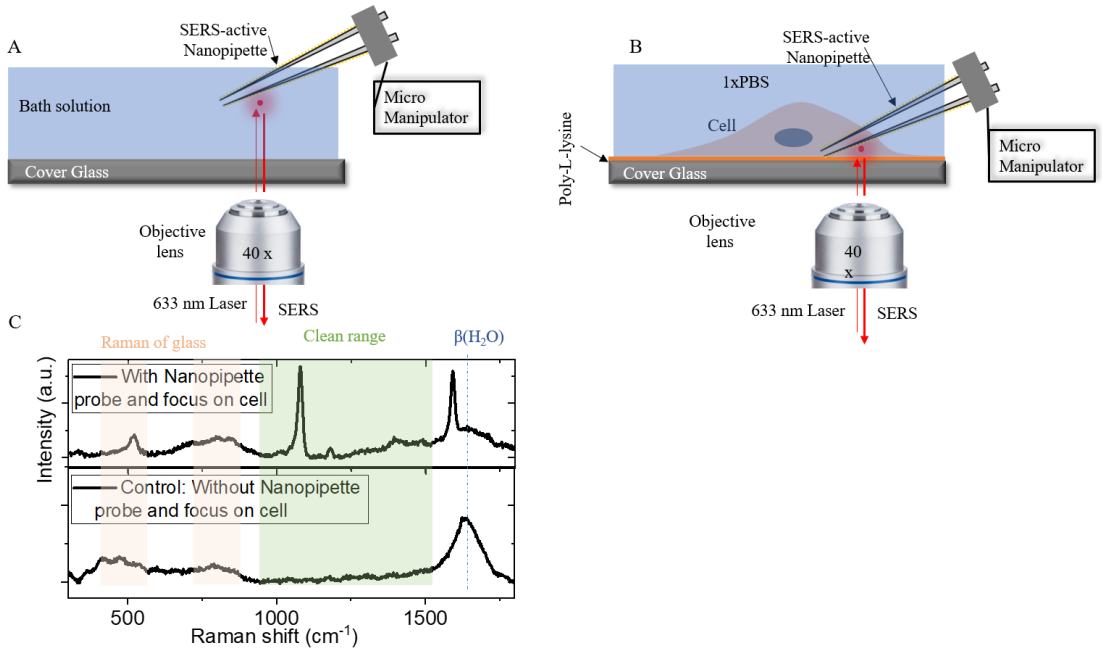

Figure 5-17 (A-B) Schematic of the experimental setup for the calibration (A) and actual intracellular sensing (B) experiments using the pH-sensitive nanopipette. (C) Top: Typical SERS spectrum acquired by a pH-sensitive nanopipette tip inside a cell. Bottom: Typical Raman spectrum of the cover glass with the absence of a SERS-active nanopipette, the exposure time is 2 s per frame.

5.3.5 Dynamic Response of the Nanopipette to pH Changes

Motivated by the temporal dynamics of living cells, it is essential to understand the response time of the nanoprobe for dynamic pH changes in the solution. Figure 5-18A shows the fluidic device made by Polydimethylsiloxane (PDMS). The nanopipette is embedded in the middle of the fluidic chamber. By switching two solutions with pH 4 and 8 at the inlet, controllable pH changes are introduced in the fluidic chamber. The measured real-time SERS changes are shown in the heat-map trajectory in Figure 5-18B. From the intensity (I_{1400}/I_{1077})-time trace at the bottom panel of Figure 5-18B, it takes about 5 s (indicated as t_0 in Figure 5-18B) to reach the maximum signal in responding to the solution

pH change. This response time is mainly limited by the fluid flow speed. It takes about 5 s for the solution to fully fill the 1000 μL fluidic chamber with a speed of 200 μL/s while the time resolution of the Raman signal is 1 s. Nevertheless, the results imply that the nanopipette-based pH nanoprobe has a pH response time at least a few seconds.

The open channel of the nanopipette can also be utilized for pH sensing. A proof-of-concept experiment is illustrated in Figure 5-18C. The pH of the solution inside the nanopipette barrel is 11, and the pH of the bath solution is 7.4. By applying a negative bias at the Ag/AgCl electrode inside the nanopipette barrel, the hydroxyl ions inside the nanopipette are driven out of the nanopipette barrel by the electric force. The effect of bias driven local pH change is demonstrated in the SERS trajectory shown in Figure 5-18D. At zero bias, the SERS trajectory was very stable and no spectral changes are detected (See Figure 5-19). After applying -0.5 V, the peak near 1400 cm^{-1} increased significantly, suggesting the increase of local pH. Therefore, the concentration gradient alone is not enough to drive hydroxyl ions out of the nanopipette tip. The applied bias is effective to deliver hydroxyl ions from the nanopipette tip to the bath solution. This experiment demonstrates the SERS active nanopipette loaded with molecules/ions inside the barrel could be used to electrically regulate the molecule/ion delivery while simultaneously monitoring the real-time and *in-situ* changes induced by the delivered molecules/ions through Raman spectral changes.

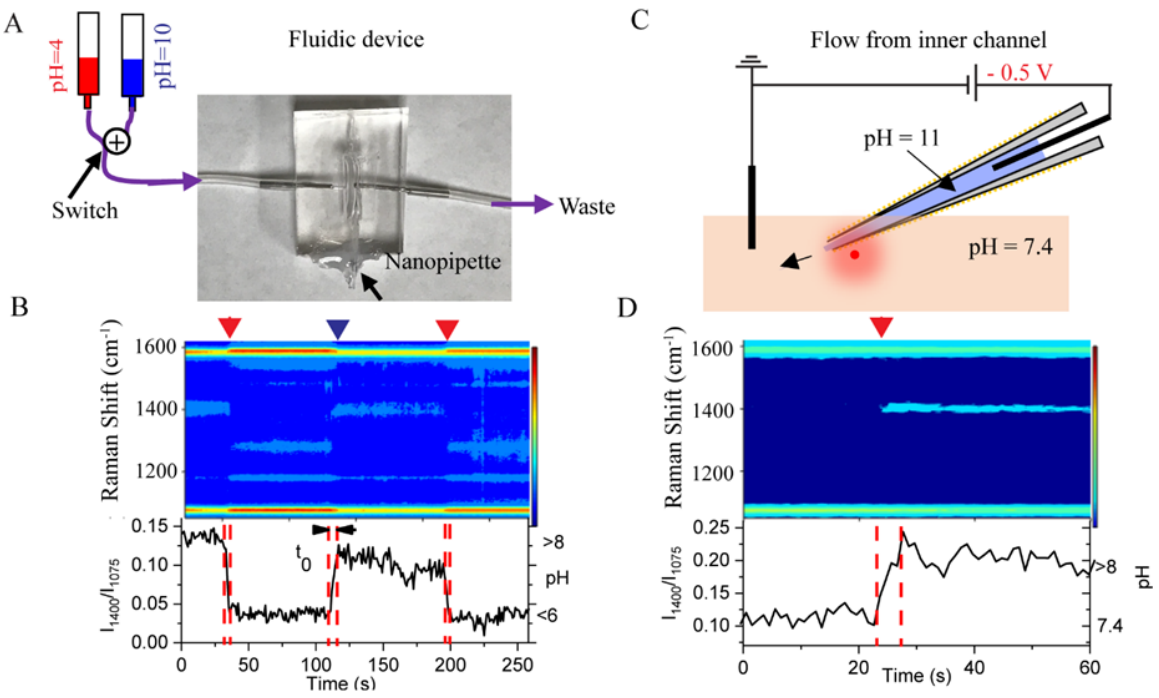

Figure 5-18 (A) Schematic (not to scale) of a fluidic device with the embedded pH-sensitive nanopipette. The bottom of the fluidic device is sealed by a cover glass. Solution with two different pH values passes through the nanopipette alternatively. (B) Top: Dynamic responding of SERS heatmap as two different pH bulk solutions passing through nanopipette. Red and blue arrows indicate pH 4 and pH 10 bulk solution passing to nanopipette. Bottom: intensity time trace of I_{1400}/I_{1077} and right y-axis indicate pH value. (C) Schematic drawing (not to scale) of pH 11 solution filled nanopipette exchange H^+ with pH 7.4 surrounding solution. (D) Top: Dynamic responding of SERS heatmap as H^+ exchange through nanopipette open channel. Red arrow indicates the moment of -500 mV potential applied. Bottom: intensity ratio (I_{1400}/I_{1077}) time trace and right axis indicate pH by using the calibration curve.

In the above paragraph, we have shown that the basic solution loaded in the nanopore barrel can be released electrically by an applied bias and locally change the pH near the apex of the nanopipette. This process is well-controlled by the applied bias in the nanopore barrel. At zero bias, no observable spectral changes were observed. One typical time-resolved SERS trajectory at zero bias is shown in Figure 5-19.

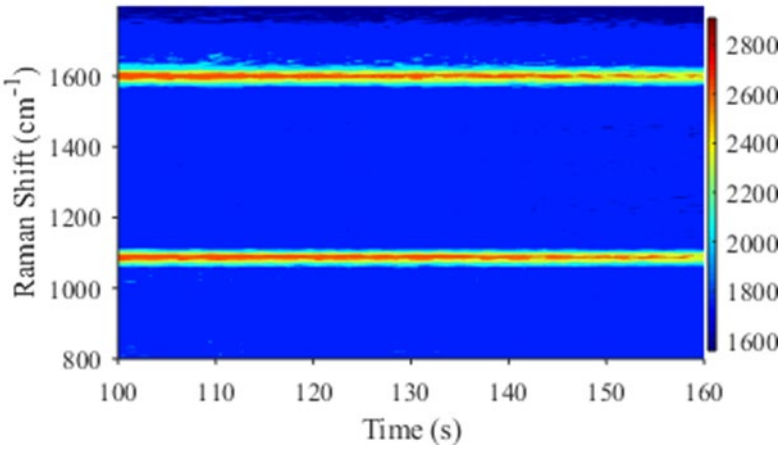

Figure 5-19 Heatmap of time-resolved SERS spectra (1 s per frame) at zero bias.

5.3.6 Single-cell Intracellular pH Sensing

We further use the pH-sensitive nanopipette to detect pH_i changes in individual cells. Controlled by a piezo micromanipulator, the pH-sensitive nanopipette tip is inserted into HeLa and Fibroblast cells at the center of the cells. Time-resolved SERS measurements are performed when the nanopipette tip reaches the designed location. Figure 5-20A shows the optical images of HeLa cells when the nanopipette tip was approached to, inside, and retreated out of the cell, respectively. The cell damage induced by the insertion of the nanopipette was tested by the Trypan blue assay. After the insertion by a long-taper nanopipette, the cells appear colorless within 60 min. In contrast, short-taper nanopipette inserted cells often shows a distinctive blue color within 2 min. Thus, we are able to perform the live-cell experiments in an hour using the long-taper nanopipette. By using the nanopipette nanoprobe, pH_i of HeLa and fibroblast cells in 1xPBS were measured based on the SERS spectra of 4-MBA molecule. Based on the calibration curve of each nanopipette, the measured pH_i values are always is in the range between 7.1 and 7.5, which are typical for the healthy cell in the culture environment.

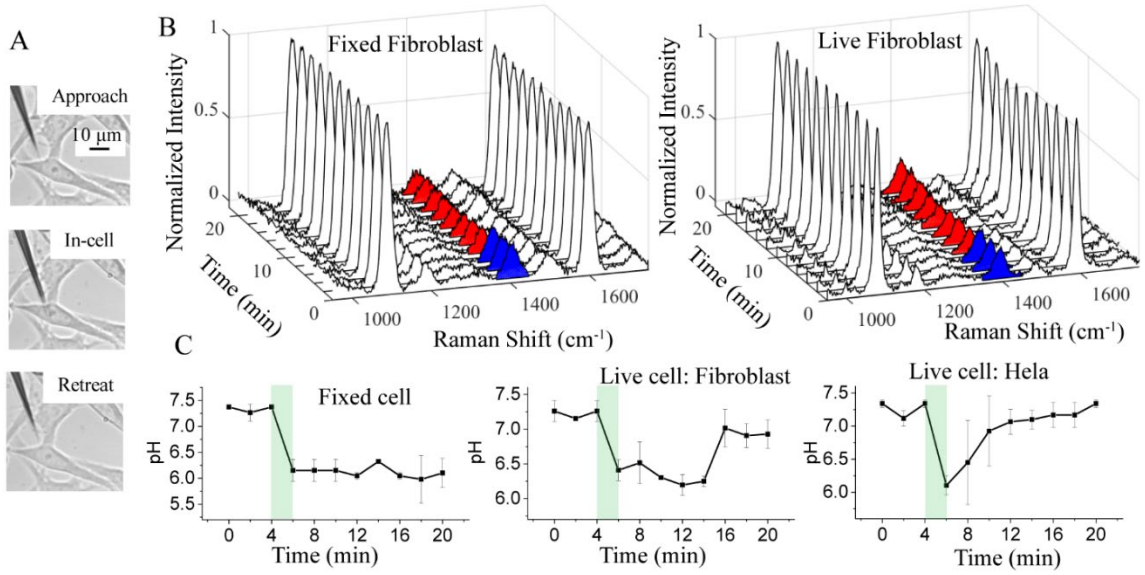

Figure 5-20 (A) Bright-field images of HeLa cell before, during, and after the nanopipette-based nanoprobe insertion. (B) Normalized SERS spectra of the nanopipette-based nanoprobe in a fixed and live Fibroblast cell under pH_e = 7.4 (blue color filled 1400 cm^{-1}) and pH_e = 6.0 (red color filled 1400 cm^{-1}) stimulation for different time periods. (C) Variation of the pH_i value in fixed Fibroblast cells, live Fibroblast and HeLa cells versus the time. The green shaded regions highlight the solution exchange time when the pH_e is changed from 7.4 to 6.0. The error bars are obtained from the standard deviation of three separate measurements. The pH calibration curves for nanopipettes nanoprobes are shown in Figure 5-21.

Then we measured the dynamic pH_i change induced by the change of pH_e. All the experiments have been repeated at least three times with good reproducibility. Figure 5-20B shows a series of SERS spectra collected by the nanopipette tip inside the fixed (left) and live (right) Fibroblast cells at different times. The pH_e of the medium was initially at 7.4 and replaced by pH_e 6.0 medium during 4-6 min. Raman spectrum acquisition was interrupted for 2 min due to the solution exchange. Correspondingly, the magnitude of the peak at 1400 cm^{-1} in the SERS spectra is higher (in blue color) in the first 4 min and then drops at 6 min (in red color) for both fixed and live fibroblast cells. However, at a later

time, the peak height at 1400 cm^{-1} increases gradually for live Fibroblast cells but not for the fixed Fibroblast.

Based on the calibration curve, we plotted the pH_i change as a function of time for both cells in Figure 5-20C. For the fixed Fibroblast cells, the pH_i quickly drops and stays near 6.1. This is attributed to the increased permeability of the cell membrane of the fixed cell. The pH_i of the live fibroblast cell also drops immediately with the change of pH_e. However, the pH_i of the live fibroblast cells gradually returns to ~7.3 after about 10 min while the cells remain in the weak acidic medium with pH_e 6. We did not observe visible changes in the morphology of the fibroblast cell. Therefore, the fibroblast cells likely adapt to environmental pH changes after 10 min. After that, the live fibroblast cells can maintain their cytoplasmic pH near neutral while they are still in a slightly acidic environment.

For comparison, we also studied the pH_i response of HeLa cells when they were exposed to the same weak acidic environment. The result is shown at the right panel in Figure 5-20C. Similar to the live fibroblast cell results, the pH_i of Hela cell decreases within 2 min with the exposure to the weak acidic environment. This change is much faster than the reported time of more than 10 min.[7, 34] We speculate that the seal between the cell membrane and nanopipette tip maybe affected by the sudden change of pH_e and allows more protons to enter the cytoplasm, leading to the relatively fast drop of pH_i.[35] However, the leakage must be very small and can be resealed quickly because the cells are still viable. Different from the live fibroblast cells, the pH_i of HeLa cells begins to increase right after the drop and returns to the initial neutral value in about 6 min. The quick response and faster recovery of pH_i of the HeLa cell indicate that the cancer cells may better regulate its

pH_i and adapt to the acidic environment. This is consistent with the fact that the tumor is often in an acidic microenvironment.

Figure 5-21A shows the SERS response of nanoprobe1 to different bath solution pH before (Pre-calibration) and after (Post-calibration) the live-cell intracellular pH sensing experiments. Figure 5-21B(i) shows the I_{1400}/I_{1077} at different pH. The SERS changes of pre-calibration and post-calibration are not exactly overlapped. Therefore, the average curve of pre- and post-calibration curves were used for the intracellular pH determination. By using the same method, the calibration curve of nanoprobe2 was obtained, as shown in Figure 5-21B(ii).

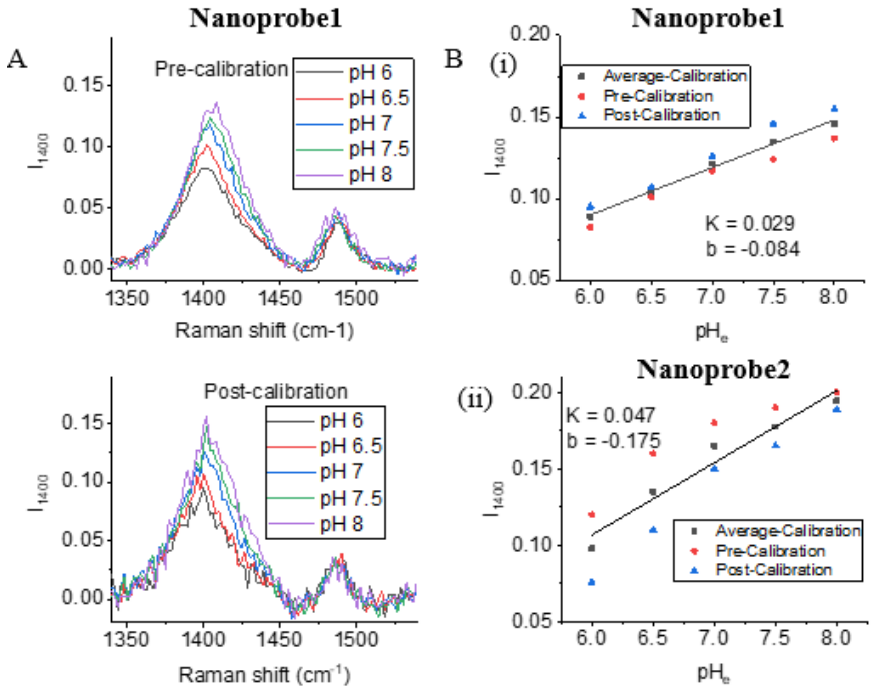

Figure 5-21 (A) SERS spectra of the nanoprobe1 in phosphate buffer solutions with different pH before (top) and after (bottom) the intracellular pH sensing experiments. (B)((i)-(ii)) The linear calibration curves of nanoprobe1 ((i), R^2 = 0.99) and nanoprobe2 ((ii), R^2 = 0.97) used for pH_i sensing.

5.4 Conclusion

In summary, we have successfully prepared SERS-active flexible nanopipettes for live-cell intracellular pH sensing. Because of the nanoscale size of the apex and the long taper geometry of the tip, the nanopipette is highly flexible and causes minimal cellular damage when it is inserted into the cell. The optimized AuNPs surface distribution and density on the outer surface of the glass nanopipette enable sensitive and fast responses in the SERS signal of pH-reporter molecule 4-MBA. The pH response of the SERS nanoprobe is linear in the dynamic range between pH 6.0 and 8.0. The ratiometric SERS signal acquired from the nanopipette tip inside the cell is stable over time, and the tip-to-tip variation is small. The non-specific adsorption of molecules and proteins on the AuNP surface only affects the overall Raman intensity but not the intensity ratio I_{1400}/I_{1077} of 4-MBA molecule. We found that the cancerous HeLa cell could effectively regulate its pH_i and better adapt to the weakly acidic extracellular environment than normal cells, such as fibroblast cells.

There are still a lot of rooms to improve this sensor. The shape and size of the AuNP can be further optimized to improve the sensitivity. By introducing antifouling reagents, e.g., Polyethylene glycol (PEG), during chemical modification, the stability and selectivity of the sensor can also be improved. This sensor can also be easily tailored to different applications or expand pH sensing range by using different Raman probe molecules. The demonstrated on-demand local delivery is another advantage of this sensor. Therefore, we expect that the plasmonic

nanopipette can be a promising sensor platform for various single-cell analysis applications, especially real-time intracellular sensing.

5.5 Reference

1. Scaffidi, J.P., et al., SERS-based plasmonic nanobiosensing in single living cells. Analytical and Bioanalytical Chemistry, 2009. **393**(4): p. 1135-1141.

2. Dittrich, P. and N. Jakubowski, Current trends in single cell analysis. Analytical and Bioanalytical Chemistry, 2014. **406**(27): p. 6957-6961.

3. Liu, J., et al., Voyage inside the cell: Microsystems and nanoengineering for intracellular measurement and manipulation. Microsystems &Amp; Nanoengineering, 2015. **1**: p. 15020.

4. Vitol, E.A., et al., Nanoprobes for intracellular and single cell surface‐enhanced Raman spectroscopy (SERS). Journal of Raman Spectroscopy, 2012. **43**(7): p. 817-827.

5. Niu, J.J., et al., Carbon Nanotube‐Tipped Endoscope for In Situ Intracellular Surface‐Enhanced Raman Spectroscopy. Small, 2011. **7**(4): p. 540-545.

6. Singhal, R., et al., Multifunctional carbon-nanotube cellular endoscopes. Nature Nanotechnology, 2010. **6**: p. 57.

7. Thomas, R.C., Intracellular pH of snail neurones measured with a new pH-sensitive glass mirco-electrode. The Journal of physiology, 1974. **238**(1): p. 159-180.

8. Özel, R.E., et al., Single-cell intracellular nano-pH probes. RSC Advances, 2015. **5**(65): p. 52436-52443.

9. Hailing, L., et al., A Multiparameter pH-Sensitive Nanodevice Based on Plasmonic Nanopores. Advanced Functional Materials, 2018. **28**(1): p. 1703847.

10. Jayant, K., et al., Flexible Nanopipettes for Minimally Invasive Intracellular Electrophysiology In Vivo. Cell Reports, 2019. **26**(1): p. 266-278.e5.

11. Wang, W., et al., A SERS Optophysiological Probe for the Real-Time Mapping and Simultaneous Determination of the Carbonate Concentration and pH Value in a Live Mouse Brain. Angewandte Chemie International Edition, 2019. **58**(16): p. 5256-5260.

12. Vitol, E.A., et al., In Situ Intracellular Spectroscopy with Surface Enhanced Raman Spectroscopy (SERS)-Enabled Nanopipettes. ACS Nano, 2009. **3**(11): p. 3529-3536.

13. Hanif, S., et al., Nanopipette-Based SERS Aptasensor for Subcellular Localization of Cancer Biomarker in Single Cells. Analytical Chemistry, 2017. **89**(18): p. 9911-9917.

14. Freedman, K.J., et al., On-Demand Surface- and Tip-Enhanced Raman Spectroscopy Using Dielectrophoretic Trapping and Nanopore Sensing. ACS Photonics, 2016. **3**(6): p. 1036-1044.

15. Hanif, S., et al., Organic Cyanide Decorated SERS Active Nanopipettes for Quantitative Detection of Hemeproteins and Fe3+ in Single Cells. Analytical Chemistry, 2017. **89**(4): p. 2522-2530.

16. Masson, J.-F., et al., Plasmonic Nanopipette Biosensor. Analytical Chemistry, 2014. **86**(18): p. 8998-9005.

17. Liu, H.-L., et al., Size-Controllable Gold Nanopores with High SERS Activity. Analytical Chemistry, 2017. **89**(19): p. 10407-10413.

18. Casey, J.R., S. Grinstein, and J. Orlowski, Sensors and regulators of intracellular pH. Nature Reviews Molecular Cell Biology, 2010. **11**(1): p. 50-61.

19. Boron, W.F., Regulation of intracellular pH. Advances in Physiology Education, 2004. **28**(4): p. 160-179.

20. Murphy, Michael P., et al., Unraveling the Biological Roles of Reactive Oxygen Species. Cell Metabolism, 2011. **13**(4): p. 361-366.

21. Rhee, S.G., H₂O₂, a Necessary Evil for Cell Signaling. Science, 2006. **312**(5782): p. 1882-1883.

22. Winterbourn, C.C., Reconciling the chemistry and biology of reactive oxygen species. Nature Chemical Biology, 2008. **4**(5): p. 278-286.

23. Sun, F., et al., Sensitive and Fast Detection of Fructose in Complex Media via Symmetry Breaking and Signal Amplification Using Surface-Enhanced Raman Spectroscopy. Analytical Chemistry, 2014. **86**(5): p. 2387-2394.

24. Sun, F., et al., Hierarchical zwitterionic modification of a SERS substrate enables real-time drug monitoring in blood plasma. Nature Communications, 2016. **7**(1): p. 13437.

25. Han, J. and K. Burgess, Fluorescent Indicators for Intracellular pH. Chemical Reviews, 2010. **110**(5): p. 2709-2728.

26. Laffafian, I. and M.B. Hallett, Lipid-Assisted Microinjection: Introducing Material into the Cytosol and Membranes of Small Cells. Biophysical Journal, 1998. **75**(5): p. 2558-2563.

27. Schrlau, M.G. and H.H. Bau. Tools for Nanosurgery: Applying Carbon Nanopipettes to Cell Physiology. in ASME 2008 3rd Frontiers in Biomedical Devices Conference. 2008.

28. Ma, T., et al., Modulating and probing the dynamic intermolecular interactions in plasmonic molecule-pair junctions. Physical Chemistry Chemical Physics, 2019. **21**(29): p. 15940-15948.

29. Zong, Y., et al., Plasmon-induced decarboxylation of mercaptobenzoic acid on nanoparticle film monitored by surface-enhanced Raman spectroscopy. RSC Advances, 2014. **4**(60): p. 31810-31816.

30. Handa, S., Y. Yu, and M. Futamata, Adsorbed state of p-mercaptobenzoic acid on silver nanoparticles. Vibrational Spectroscopy, 2014. **72**: p. 128-133.

31. Phan, H.T. and A.J. Haes, Impacts of pH and Intermolecular Interactions on Surface-Enhanced Raman Scattering Chemical Enhancements. The Journal of Physical Chemistry C, 2018. **122**(26): p. 14846-14856.

32. Lu, G., B. Shrestha, and A.J. Haes, Importance of Tilt Angles of Adsorbed Aromatic Molecules on Nanoparticle Rattle SERS Substrates. The Journal of Physical Chemistry C, 2016. **120**(37): p. 20759-20767.

33. Lee, S.B., K. Kim, and M.S. Kim, Surface-enhanced Raman scattering of o-mercaptobenzoic acid in silver sol. Journal of Raman Spectroscopy, 1991. **22**(12): p. 811-817.

34. Fellenz, M.P. and L.E. Gerweck, Influence of Extracellular pH on Intracellular pH and Cell Energy Status: Relationship to Hyperthermic Sensitivity. Radiation Research, 1988. **116**(2): p. 305-312.

35. Angelova, M.I., et al., pH sensing by lipids in membranes: The fundamentals of pH-driven migration, polarization and deformations of lipid bilayer assemblies. Biochimica et Biophysica Acta (BBA) - Biomembranes, 2018. **1860**(10): p. 2042-2063.

CHAPTER 6 SUMMARY AND FUTURE RESEARCH

6.1 Summary of Results

In summary, my dissertation demonstrates that the AuNP collisions at a SAM modified AuNE enable the construction of plasmonic molecular junctions of NPoNE. Compared with flat microelectrodes, the large curvature of AuNE renders the AuNP thermodynamically unstable, limiting the number of adsorbed AuNPs at the AuNE apex to a few, thus limiting the number of hot spots. We have successfully monitored the dynamic formation of new junctions, which are initiated by a AuNP collision event at the AuNE. The new NPoNE geometry and the simultaneous SERS/electrochemical measurements also have a great potential to be utilized in the study of single molecule chemical reactions confined in a nanocavity or nanoreactor[1] and the interplay between molecular electronics and plasmonics.[2, 3]

The effective and reversible electrochemical tuning of SERS intensity can be achieved with the assistant of the chemical transformation of the Ag shell of shell-core plasmonic NPs. The Au@Ag NP can be formed *in situ* on the SAM covered AuNE surface, and the formation of Ag shell can be interrogated in real-time through monitoring both the EC current and SERS changes. When the electrode potential was swept on the formed Au@Ag NPoNE structures, the simultaneously acquired EC current and SERS revealed the strong correlation between the redox reaction of silver shell and the SERS intensity modulation. The degree and reversibility of SERS tuning were controlled by the Ag deposition time on AuNPs. 3D-FDTD simulation confirmed the EME modulation is mainly due to the large refractive index change of the shell when the metallic Ag is converted to

insulating AgCl. In addition to the modulation of EME, the CE can also be modulated during the chlorination of the Ag shell. The specific molecular-metal interaction can be switch on and off during the chemical conversion of the shell between Ag and AgCl. The combination of EME and CE modulation can further enhance the tuning effect. With the tuning of EME and CE, this work can help to understand better the EME and CE mechanisms and metal-molecule interactions in plasmonic molecular junctions. Furthermore, the *in situ* fabricating and controlling of NPs electrochemistry and SERS monitoring can easily integrate with plasmonic sensing. Direct chemical and optical electrochemistry measurements can help us fully understanding the role of plasmons and eventually utilizing for catalyzing and sensing. The electrode potential also provides a facile and fast means to tune SERS intensity and can trigger new applications in electroanalysis, heterogeneous catalysis, photocatalysis, plasmonics, molecular electronics, and biosensing.

With the fundamental understanding of the SERS technique and SM investigation, we further investigate the capability of SERS for single-cell analysis. We have successfully prepared SERS-active flexible nanopipettes for live-cell intracellular pH sensing. Because of the nanoscale size of the apex and the long taper geometry of the tip, the nanopipette is highly flexible and causes minimal cellular damage when it is inserted into the cell. The optimized AuNPs surface distribution and density on the outer surface of a glass nanopipette enable sensitive and fast responses in the SERS spectra of pH-reporter molecule 4-MBA. The pH response of the SERS nanoprobe is linear in the dynamic range between pH 6 and 8. The ratiometric SERS signal acquired from the nanopipette tip inside the cell is stable over time, and the tip-to-tip variation is small. The non-specific adsorption

of molecules and proteins on the AuNP surface only affects the overall Raman intensity but not the intensity ratio I_{1400}/I_{1077} of 4-MBA molecule. We found that the cancerous HeLa cell could better adapt to the extracellular solution pH change than normal cells, such as fibroblast cells. This is consistent with the fact that the tumor is often in an acidic microenvironment.

Other than pH sensor, glucose, and H_2O_2 sensors based on SERS were also tested. Even though those sensors still not working for intracellular sensing yet, they have shown good performance in the prepared solution. By redesigning the SERS-active substrate and introducing antifouling reagents, e.g., Polyethylene glycol (PEG), during chemical modification, the glucose and H_2O_2 sensors may also apply for single-cell analysis. The demonstrated on-demand local delivery is another advantage of this sensor. Therefore, we expect that the plasmonic nanopipette can be a promising sensor platform for various single-cell analysis applications, especially real-time intracellular sensing.

6.2 Future Research

6.2.1 Scattering Spectrum of Plasmonic Nanostructure

Plasmonic nanoparticles present unique and changeable optical properties due to the phenomenon of LSPR have been used as nanosensors toward single-cell sensing. The optical properties can be monitored by scattering spectra with darkfield microscopy. Figure 6-1A shows the setup of home-made darkfield microscopy in our lab. Figure 6-1B shows the preliminary results of the scattering spectra for AuNPs on cover slides with different sizes. In the future, we will develop ultrasensitive sensors based on scattering spectra of plasmonic nanostructures.

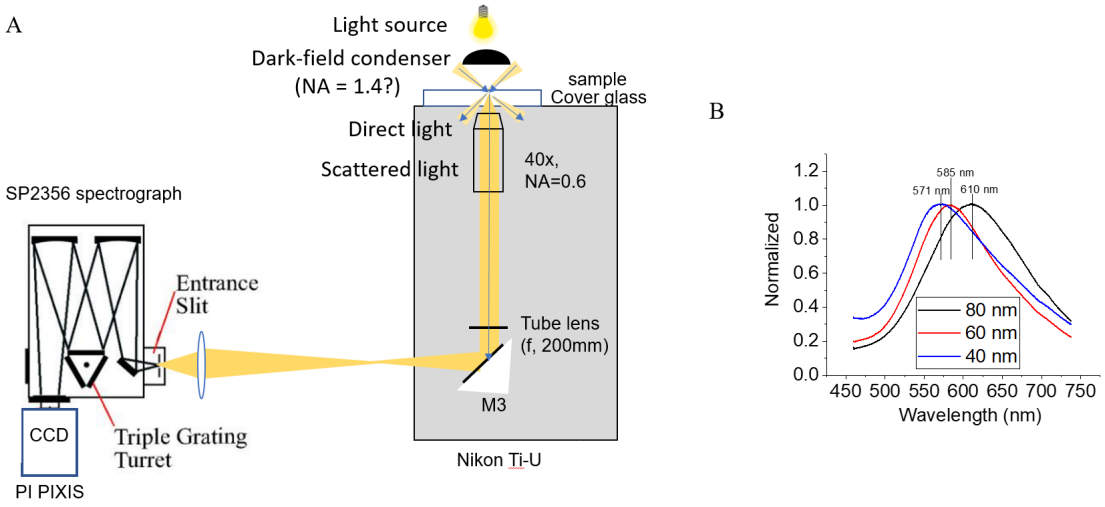

Figure 6-1 (A) The setup of home-made darkfield spectroscopy. (B) Scattering spectra of AuNPs on a cover slide with a diameter of 40, 60, and 80 nm.

6.2.2 Nanorod Array for Biological Sensing

The majority of substrate preparation techniques focus on how to maximize Raman enhancement. The reproducibility and production of SERS substrate are rarely discussed. There are following fabrication techniques meet all the above-mentioned requirements: electron beam lithography (EBL), nanosphere lithography (NSL), template method, hybrid method, and oblique angle vapor deposition (OAD) method. Among those techniques, the OAD method has advantages such as i) low cost; ii) use the conventional physical vapor deposition instrument; iii) large substrate deposition. The mechanism of the OAD method is the geometric shadow effect.[4, 5]

Figures 6-2 and 6-3A show the preliminary results of the AuNR array by the OAD fabrication method. There are still many parameters need to be tuned to reach considerable SERS enhancement. Figure 6-3B shows the plan of single cell-extracellular SERS detection. The flat SERS substrate may use to get the extracellular chemical distribution image. The glass pipette SERS substrate will apply for point of care measurement.

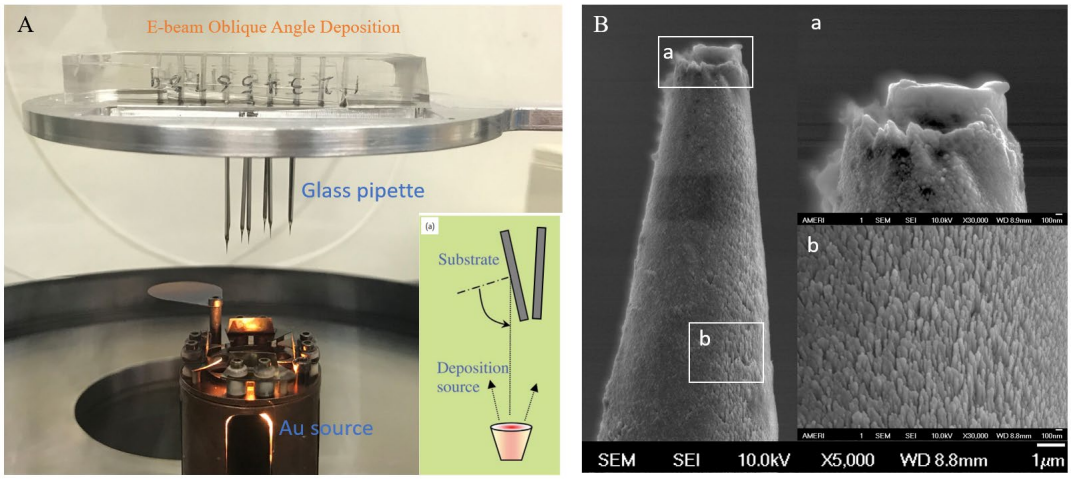

Figure 6-2 (A) Optical image of E-beam deposition based OAD method fabricated AuNR array on glass pipette. Insert is the schematic of OAD deposition. (B) SEM images of glass pipette with OAD method AuNR fabrication.

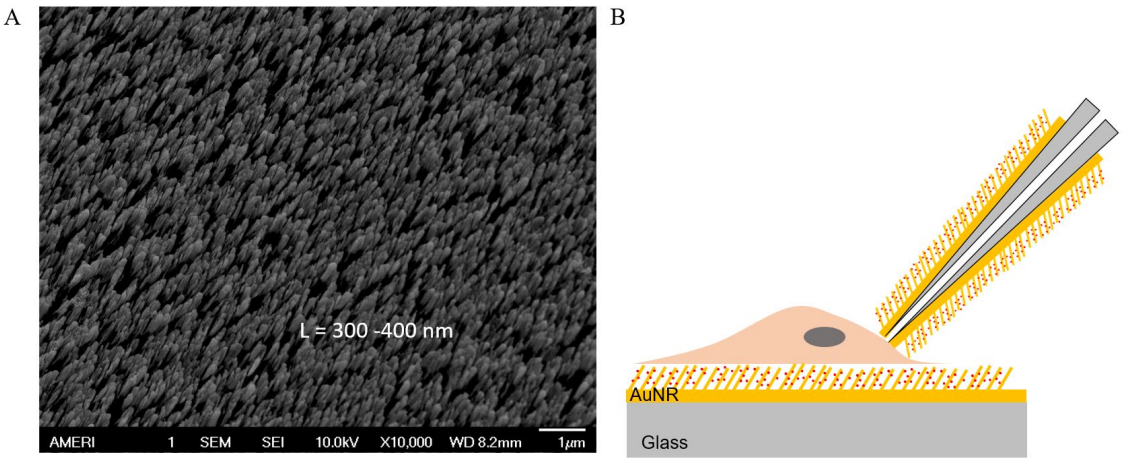

Figure 6-3 (A) OAD method fabricated AuNR array on flat cover glass. (B) Schematic of the plan for single cell extracellular SERS measurement.

6.2.3 Plasmonic Nanostructures for Local Heating Effect

LSPR effect of plasmonic nanostructures allows them absorption of incident light significantly increased at a specific resonance frequency. The absorbed light energy of plasmonic nanostructures will be released as heat to the environment. Thus the plasmonic nanostructures can be used as light-to-heat converters. And this heating effect of plasmonic

nanostructures can be started and controlled by an external laser. Plasmonic nanostructures have great potential to treat cancer or tumor. Since the spectral window in the near-infrared (NIR) region (700−1300 nm) is biological transparency, it allows light to penetrate biological tissue with centimeter depth.[6] Due to extremely high adsorption of AuNR and gold nanostars (AuNSt) at the NIR region, and I used to synthesize those nanostructures, I plan to investigate their photothermal efficiency.

6.3 Reference

1. Choi, H.-K., et al., Metal-Catalyzed Chemical Reaction of Single Molecules Directly Probed by Vibrational Spectroscopy. Journal of the American Chemical Society, 2016. **138**(13): p. 4673-4684.

2. Wilson, A.J. and K.A. Willets, Molecular Plasmonics. Annual Review of Analytical Chemistry, 2016. **9**(1): p. 27-43.

3. Zhu, W., et al., Quantum mechanical effects in plasmonic structures with subnanometre gaps. Nature Communications, 2016. **7**(1): p. 11495.

4. He, Y., J. Fu, and Y. Zhao, Oblique angle deposition and its applications in plasmonics. Frontiers of Physics, 2014. **9**(1): p. 47-59.

5. Barranco, A., et al., Perspectives on oblique angle deposition of thin films: From fundamentals to devices. Progress in Materials Science, 2016. **76**: p. 59-153.

6. Jauffred, L., et al., Plasmonic Heating of Nanostructures. Chemical Reviews, 2019. **119**(13): p. 8087-8130.

CURRICULUM VITAE

JING GUO

EDUCATION

Ph.D	2016-2020	Biophysics, Florida International University (FIU), United State
Visiting Scholar	2014-2016	Biophysics, FIU United State
Ph.D (Not Completed)	2011-2014	Department of Electronic Physics, University of Electronic Science and Technology of China (UESTC), China
B.S.	2007-2011	Department of Electronic Physics, UESTC, China

PUBLICATION and CONFERENCE

1. *J. Guo*, A. Rubfiaro, Y. Lai, J. Moscoso, F. Chen, Y. Liu, X. Wang, J. He (2020) "The Dynamic Single-Cell Intracellular pH Sensing by a SERS-Active Nanopipette" Analyst 145: 4852-4859.
2. Thapa, *J. Guo*, K. Jungjohann, X. Wang, W. Li (2020). "Density control of vertically aligned carbon nanotubes and its effect on field emission properties." Materials Today Communications 22: 100761.
3. L. Yu, Z. Wang, H. Chen, *J. Guo*, M. Zhang, Y. Liu, J. He, S. Chang (2020). "Long-Lived Gold Single-Atom Junctions Formed by a Flexible Probe for Scanning Tunneling Microscopy Applications." ACS Applied Nano Materials 3(4): 3410-3416.
4. D. Yang, G. Liu, H. Li, A. Liu, *J. Guo*, Y. Shang, Z. Wang, J. He (2020). "The fabrication of a gold nanoelectrode–nanopore nanopipette for dopamine enrichment and multimode detection." Analyst 145(3): 1047-1055.
5. T. Ma, *J. Guo*, S. Chang, X. Wang, J. Zhou, F. Liang, J. He (2019) "Modulating and probing the dynamic intermolecular interactions in plasmonic molecule-pair junctions." Physical Chemistry Chemical Physics 21(29): 15940-15948.
6. P. Pandey, J. Garcia, *J. Guo*, X. Wang, D. Yang, J. He (2019). "Differentiation of metallic and dielectric nanoparticles in solution by single-nanoparticle collision events at the nanoelectrode." Nanotechnology 31(1): 015503.
7. M. Aljaghtham, Z. Liu, *J. Guo*, J. He, E. Celik (2019) "Numerical Simulations of Cell Flow and Trapping within Microfluidic Channels for Stiffness Based Cell Isolation Journal of Biomechanics." Journal of Biomechanics 85: 43–49.

8. *J. Guo*, J. Pan, S. Chang, X. Wang, J. He (2018) "Monitoring the Dynamic Process of Formation of Plasmonic Molecular Junctions during Single Nanoparticle Collisions." Small 14(15): 1704164.
9. *J. Guo*, J. He and B. Zeng (2016) "Carbon Nanotube-Based Nanopore and Nanofluidic Devices Towards Sensing Applications." Current Nanoscience 12(4): 421-428.
10. J. Liu, B. Zeng, W. Wang, N. Li, *J. Guo*, Y. Fang (2014) "High-Current-Density Edge Electron Emission and Electron Beam Shaping for Vacuum Electronics Using Flexible Graphene Paper." IEEE Transactions on Electron Devices 61(6): 1776-1780.
11. J. Liu, B. Zeng, W. Wang, N. Li, *J. Guo*, Y. Fang (2013) "Graphene electron cannon: High-current edge emission from aligned graphene sheets." Applied Physics Letters 104 (2), 023101.
12. W. Cai, B. Zeng, J. Liu, *J. Guo*, N. Li, L. Cheng (2013). "Improved field emission property of graphene by laser irradiation." Applied Surface Science 284: 113-117.
13. *Presentation:* "Electrochemical tuning Localized Surface Plasmon Resonance of Au-Ag core-shell nanoparticle for Surface-Enhanced Raman Scattering" American Physical Society Annual Meeting, Denver, Colorado, March 2-6, 2020 Canceled due to COVID19
14. *Poster:* "Modulating and probing the dynamic intermolecular interactions in plasmonic molecule-pair junctions" Biophysical Society 64rd Annual Meeting, San Diego, California, February 16-20, 2020
15. *Poster:* "SERS-active Nanopipette For Single Cell Intracellular pH Sensing" Biophysical Society 63rd Annual Meeting, Baltimore, Maryland, March 2-6, 2019
16. *Presentation:* "Nanopipette for Single Cell Intra- and Extra-Cellular pH Sensing by Surface Enhanced Raman Spectroscopy (SERS)" NanoFlorida2018, Melbourne, FL, October 2018
17. *Presentation:* "Dynamic plasmonic molecular junctions formed by single nanoparticle collision" NanoFlorida2017, Miami, FL, September 2017
18. *Poster:* "Study recognition tunneling current in single nanoparticle collision events", NanoFlorida2016, Orlando, FL, September 2016
19. NanoFlorida2015, Miami, FL, September 2015
20. NanoFlorida2014, Orlando, FL, September 2014